CODED APERTURE DESIGN IN A THREE-DIMENSIONAL SUPER-RESOLUTION SYSTEM OF COMPRESSIVE COMPUTED TOMOGRAPHY

EDSON FABIÁN MOJICA RODRIGUEZ

UNIVERSIDAD INDUSTRIAL DE SANTANDER
FACULTAD DE INGENIERÍAS FISICOMECÁNICAS
ESCUELA DE INGENIERÍA DE SISTEMAS E INFORMÁTICA
BUCARAMANGA

2022

CODED APERTURE DESIGN IN A THREE-DIMENSIONAL SUPER-RESOLUTION SYSTEM OF COMPRESSIVE COMPUTED TOMOGRAPHY

EDSON FABIÁN MOJICA RODRIGUEZ

Trabajo de Grado para optar al título de
Doctor en Ciencias de la Computación

Director
Ph.D. HENRY ARGUELLO FUENTES

UNIVERSIDAD INDUSTRIAL DE SANTANDER
FACULTAD DE INGENIERÍAS FISICOMECÁNICAS
ESCUELA DE INGENIERÍA DE SISTEMAS E INFORMÁTICA
BUCARAMANGA
2022

DEDICATORIA

Este trabajo viene dedicado para todas aquellas personas que apoyaron el desarrollo y ejecución de este trabajo de grado.
A mi padre Enor Mojica, y a todos aquellos familiares quienes hoy no están conmigo.
En especial reconozco la permanente presencia de Dios en mi camino de vida.

AGRADECIMIENTOS

Agradezco a mi familia por todo el apoyo que me brinda en cada aventura emprendida durante mi vida académica. A mis amigos y compañeros, por ser el soporte de mi estabilidad mental durante estos inolvidables años de universidad. A Kareth M. León por apoyarme incondicionalmente en cada momento de duda. Quiero agradecer especialmente a mi madre Carmen Sofía Rodríguez, quien con humildad me ha inculcado la tenacidad y los valores para llegar a la culminación de este proyecto.
Un reconocimiento y agradecimiento importante a mi director, por dedicar de su tiempo los momentos suficientes para transmitir su experiencia y conocimiento para guiarme como profesional y persona durante la ejecución de mi estudio de maestría y doctorado.

RESUMEN

TÍTULO: DISEÑO DE APERTURAS CODIFICADAS EN UN SISTEMA TRIDIMENSIONAL DE SUPER-RESOLUCION DE TOMOGRAFÍA COMPUTARIZADA COMPRESIVA *

AUTOR: Edson Fabián Mojica Rodríguez **

PALABRAS CLAVE: Diseño de codigo de apertura, tomografía computarizada de rayos-X, Super-resolución, Decimación, muestreo compresivo & imagen.

DESCRIPCIÓN:

La tomografía computarizada (TC) de rayos-X de muestreo compresión (MC) se ha convertido en una herramienta esencial para conocer la estructura interna de un objeto a través de un procedimiento no invasivo. Estos enfoques utilizan aperturas codificadas (AC) a lo largo de múltiples ángulos de captura para bloquear una parte de la energía de rayos X que viaja hacia los detectores. Sin embargo, la mayoría de los diseños de AC se centran en sistemas de haz en abanico (FB) de múltiples disparos, que manejan una proporción de 1:1 entre las características de AC y los elementos detectores. En consecuencia, la resolución de la imagen está sujeta al tamaño de píxel del detector. Como alternativa, en lugar de utilizar un arreglo de detectores más denso, este trabajo presenta un método para diseñar los patrones de AC en un sistema de haz cónico (CBTC) compresivo bajo una configuración de súper resolución (SR), donde el AC de alta resolución está diseñado para obtener imágenes de alta resolución de proyecciones de menor resolución. El diseño de AC explota el teorema de Gershgorin al minimizar sus radios, mejorando la condición de la matriz del sistema. Las simulaciones muestran que el diseño obtenido logra imágenes de alta resolución a partir de detectores de menor resolución en un escenario SR-CBTC de disparo único, donde se mejora el PSNR de las imágenes reconstruidas en comparación con patrones AC no diseñados. Además, esta tesis amplía su alcance principal para incluir un diseño de AC en un sistema imagenes espectrales conocido como (CASSI), que permite aplicar de manera eficiente el concepto de MC para adquirir información espacio-espectral de una escena. El diseño de AC está formulado en diferentes arreglos de

---

* Tesis doctoral

** Escuela de ingeniería de sistemas e informática. Director: Ph.D. Henry Arguello Fuentes.

matriz para inducir una baja correlación entre filas y columnas en la matriz de Gram. La optimización incluye una máscara litográfica de colores en movimiento como restricción, alcanzando una calidad de reconstrucción similar en comparación con un diseño de AC de última generación.

ABSTRACT

TITLE: CODED APERTURE DESIGN IN A THREE-DIMENSIONAL SUPER-RESOLUTION SYSTEM OF COMPRESSIVE COMPUTED TOMOGRAPHY *

AUTHOR: Edson Fabián Mojica Rodríguez **

KEYWORDS: Coded aperture design, X-ray computed tomography, Super-resolution, Decimation, Compressive sensing & Imaging.

DESCRIPTION:

Compressive sensing (CS) X-ray computed tomography (CT) has become an essential tool to know the inner structure of the object under observation through a non-destructive scanning procedure. These approaches rely on coded apertures (CA) along multiple view angles to block a portion of the x-ray energy traveling towards the detectors. Most of CA designs, however, are focused on multi-shot fan-beam (FB) systems, handling a 1:1 ratio between CA features and detector elements. In consequence, image resolution is subject to the detector pixel size. As an alternative, instead of using a denser detector array, this work presents a method for designing the CA patterns in a compressive CBCT system under a super-resolution configuration, i.e., high-resolution CA patterns are designed to obtain high-resolution images from lower-resolution projections. The proposed CA design, exploits the Gershgorin theorem by minimizing its radii to improves the condition of the system matrix. Simulations show that the optimal design obtained from the proposed approach achieves high-resolution images from lower-resolution detectors in a single-shot SR-CBCT scenario, where the PSNR of the reconstructed images is improved compared to non-designed CA patterns under different super-resolution factors. Additionally, this dissertation extends its main scope to include a CA design in a system named coded aperture snapshot spectral imaging (CASSI), which allows efficiently apply the CS concept to acquiring spatial-spectral information of a scene. The CA design is formulated in different matrix arrangements to induce a low correlation between rows and columns in the Gram matrix. The optimization includes a novel strategy, which can be implemented as a moving-colored lithographic mask using a micro-piezo electric device. The CA design for a multiple snapshot

---

* Doctoral Thesis

** Department of Systems Engineering and Informatics. Director: Ph.D. Henry Arguello Fuentes.

imagery system offers a similar reconstruction quality compared to a CA design of state-of-the-art, considering implementable filters as a solution due to the physical limitations in the CA manufacturing.

Contents

List of Figures

pág.

Acronyms

2D two-dimensional 106, 107, 119, 123

ADMM alternating direction method of multipliers 68

ART algebraic reconstruction technique 55, 56, 57

BP basis pursuit 63, 71

BPDN basis pursuit de-noising 65

C-SALSA constrained split enhanced Lagrangian shrinkage algorithm 68, 71, 87

CA coded aperture 9, 10, 13, 14, 30, 31, 32, 33, 34, 35, 59, 60, 61, 69, 70, 71, 72, 73, 74, 75, 77, 78, 80, 81, 82, 83, 86, 89, 90, 91, 92, 94, 95, 96, 97, 98, 99, 100, 101, 102, 103, 104, 105, 117, 119, 120, 121, 124, 125, 126, 128, 130, 133

CASSI coded aperture snapshot spectral imaging 15, 30, 31, 33, 119, 121, 122, 130, 131

CB cone-beam 24, 42

CBCT cone-beam computed tomography 9, 10, 12, 13, 25, 32, 34, 36, 42, 59, 60, 61, 69, 70, 71, 72, 74, 77, 82, 83, 85, 86, 100, 104

CCA colored coded aperture 15, 117, 121, 122, 123, 124, 125, 127, 128, 130

CS compressive sensing 12, 25, 26, 27, 28, 29, 30, 34, 59, 60, 62, 63, 64, 65, 66, 67, 69, 119

CSI compressive spectral imaging 30, 117, 119, 121

CT computed tomography 9, 12, 23, 24, 25, 29, 30, 31, 32, 33, 34, 36, 39, 40, 41, 42, 44, 45, 51, 55, 59, 62, 63, 65, 66, 67, 69, 72, 73, 74, 106, 107, 109, 110, 113, 121, 133

SIRT simultaneous iterative reconstruction technique 56, 57, 58

SNR signal-to-noise ratio 14, 15, 99, 105, 115, 116

SpaRSA sparse reconstruction through separable approximation 68

SPCA sparse principal component analysis 73

SR super-resolution 14, 32, 34, 69, 70, 71, 72, 74, 95, 96, 97, 102, 103 [type=acronym

SVD singular value decomposition 13, 75, 82, 86, 91, 92, 93, 105

TV total variation 63, 65, 66, 67, 71

TwIST two-step iterative shrinkage-thresholding 68

X-ray computed tomography (CT) has become an essential tool for applications such as medical diagnosis, image-guided radiotherapy, and material characterization, where the inner structure of the object under observation can be analyzed through a non-destructive scanning observation. Cone-beam CT (CBCT) is a particular CT system that employs a single X-ray source and a flat detection area, such that multiple object slices are captured at each acquisition angle. One of the main challenges in the CBCT-based acquisition process is to obtain accurate reconstructions of the object while maintaining a relatively low radiation dose. Furthermore, compressive sensing (CS) based approaches such as compressive X-ray CBCT rely on coded apertures (CA) along multiple view angles to block a portion of the X-ray energy traveling towards the detectors, leading to less correlated projections which in turn yields to better conditioning of the system. Then, recovery algorithms are employed to obtain the three-dimensional (3D) data cube from the acquired coded projections. Previous works in CS-based acquisition systems have shown that the spatial distribution of the CA patterns and the recovery method determine the resulting image quality, where the optimization of these CA patterns is an active area of current research. State-of-the-art on CA designs exploits the concept of coherence of the sensing matrix via the Gram matrix since it describes the correlation among the columns or rows of the matrix, producing less-correlated propagation functions that increase the variability of the captured data.

In compressive CT acquisition systems, most CA designs, are focused on multi-shot fan-beam (FB) architectures, getting information of the same angle multiple times, handling a 1:1 ratio between CA features and detector elements. In consequence, image resolution is subject to the detector pixel size. Moreover, CA optimization for CT involves strong binarization assumptions, impractical data rearrangements, or computationally expensive tasks such as singular value decomposition. A high-resolution CA pattern can be placed before a low-resolution detector, producing high-resolution coding; then, high-resolution images are recovered from the acquired low-resolution measurements. State-of-art in CT-CA includes CA design strategies for the fan-beam system, which corresponds to a variation of the CBCT architecture where the detector is composed of a straight-set of elements. Due to their physical differences, CA designs for fan-beam X-ray setups cannot be directly applied to cone-beam X-ray systems. Therefore, instead of using CA distributions into a CBCT system with a more dense detector array, this dissertation presents a method for designing a higher resolution CA patterns in compressive CBCT system, performing a super-resolution configuration (SR-CBCT) in order to obtain higher-resolution 3D image reconstruction by using a single low-resolution set of projections at each angle. Hence, the CA design is formulated as a coherence minimization problem, where the CA is the optimization parameter for ensuring implementable solutions. The proposed approach exploits the Gershgorin theorem since its algebraic interpretation relates the circle radii with the eigenvalue bounds, whose minimization improves the condition of the system matrix. Simulations with medical data sets and synthetic Monte-Carlo projections show that the optimal design obtained from the proposed approach achieves high-resolution images from lower-resolution detectors in a single-shot SR-CBCT scenario, where the PSNR of the reconstructed images is improved compared to non-designed CA patterns under different super-resolution factors. Additionally, the computational cost of the proposed approach is up to three orders of magnitude lower than SVD-based methods.

Additionally, this dissertation extends its main scope to include a CA design in a remarkable compresive sensing based acquisition system named coded aperture snapshot spectral imaging (CASSI), which allows efficiently acquiring spatial-spectral information of a scene. In the optimization problem of the CASSI system design, the CA is formulated in different matrix arrangements to induce a low correlation between rows and columns in the Gram matrix. The proposed optimization includes variability and uniformity constraints, including hardware restrictions and a novel strategy, which can be implemented as a moving colored lithographic mask using a micro-piezo electric device. The CA design for a multiple snapshot imagery system offers a similar reconstruction quality compared to a CA design of state-of-the-art at a fraction of the cost of a non-moving CA, considering implementable filters as a solution due to the physical limitations in the CA manufacturing.

1. Introduction

The invention of X-ray devices dates to 1895 as the precursor of diagnostics based on imaging systems [1]. This technique enables procedures to obtain a non-destructive observation of the inner human body or the inner structure under analysis. The main issue of this technique is the acquisition process, due to the elements under analysis are exposed to ionizing radiation, increasing the possibility of damaging the object structure or even producing death for human beings. The viability of the process is subject to obtain more detailed information without increasing the radiation dose in order to prevent an over-exposure. An advancement in X-ray technology is the computed tomography (CT) scanning system, which can be described by a source that emits X-ray energy at multiple angles in the direction of a sensor line array on the opposite side [1]. The interaction between the emitted energy and the objects placed between the source and the detector array reduces the emitted energy, thus, creating a projection. Therefore, the CT system processes the multiple X-ray projections generated on the sensor to produce a high-quality volumetric reconstruction of the object's internal structure.

Assuming that the setup rotates around an axis orthogonal to the propagation plane, the object measurements used for reconstruction process can be acquired by either rotating the object or jointly rotating the source and the detector. For this reason, in medical applications, the X-ray source and the linear detector set jointly rotate around the patient [2], the scheme of this setup is shown in Fig.1(a). On the other

[1] Thorsten M Buzug. *Computed Tomography*. Springer-Verlag Berlin Heidelberg, 2008.

[2] Daniel Thomas Ginat and Rajiv Gupta. "Advances in computed tomography imaging technology". In: *Annual review of biomedical engineering* 16.1 (2014), pp. 431–453.

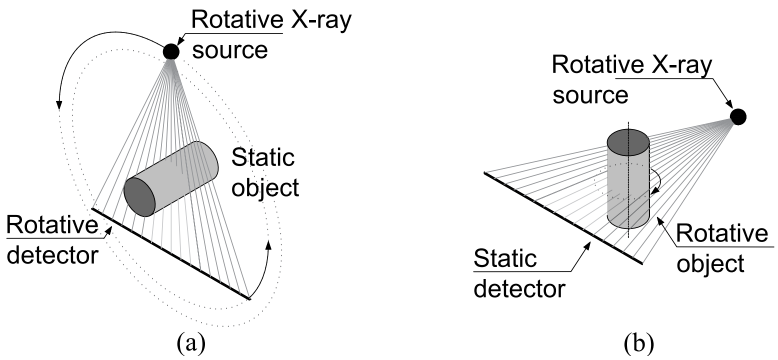

Figure 1. CT schematic with source, object, and linear detector set, for a fan-beam propagation shape of X-rays. Rotation strategies applied to (a) clinical applications and (b) industrial applications.

hand, applications in industrial quality control [3] and security [456], employ a moving base to rotate the object [7], where its setup is shown in Fig.1(b). Fig.1 illustrates the propagation of the registered X-ray beam from the source, describing a fan-beam (FB) shape between the source and the linear detector set. Varying the detector to a two-dimensional element array, the emitted X-ray energy that achieves the detector describes a cone propagation of the beam (CB). Most of the commercial X-ray CT systems are designed based on fan-beam and cone-beam geometries.

---

3 G-R Tillack, Christina Nockemann, and Carsten Bellon. "X-ray modeling for industrial applications". In: *NDT & E International* 33.7 (2000), pp. 481–488.

4 H Strecker. "Automatic detection of explosives in airline baggage using elastic X-ray scatter". In: *Medicamundi* 42 (1998), pp. 30–33.

5 C Cozzini, S Olesinski, and G Harding. "Modeling scattering for security applications: a multiple beam x-ray diffraction imaging system". In: *2012 IEEE Nuclear Science Symposium and Medical Imaging Conference Record (NSS/MIC)*. IEEE. 2012, pp. 74–77.

6 Silvia Pani et al. "Modelling an energy-dispersive x-ray diffraction system for drug detection". In: *IEEE Transactions on Nuclear Science* 56.3 (2009), pp. 1238–1241.

7 Leonardo De Chiffre et al. "Industrial applications of computed tomography". In: *CIRP annals* 63.2 (2014), pp. 655–677.

Each reconstruction of the FB system provides a slice of the object, due to each interaction occurs in the two-dimensional (2D) cross-section of the object before being recorded on the detector, which is composed of a one-dimensional array of sensors. In this case, covering the three-dimensional (3D) object means that the source and detector move in the normal direction of the slice plane. In contrast, cone-beam geometry introduces a 3D reconstruction based on volumetric interactions at the expense of increased computational resources by using a 2D detector array. The measurement acquisition using the cone-beam system dramatically reduces the time consumption compared to a fan beam system since, from an equivalent radiation dose, the cone-beam acquires multiple slices whereas the fan beam obtains a single slice.

Consequently, there is growing interest in using X-ray cone-beam computed tomography (CBCT) due to its advantages. Indeed, it is still subject to active research to obtain an image with enough high quality from a minimal exposure and/or cost.

The digitally generated image representation of an object from a **CT** system is composed of voxels (volume elements) with the attenuated information of the object under observation [1]. The propagation of energy through a voxel group establishes the behavior of attenuations, where each interaction is modeled with a linear equation. As a result, similar interactions between X-rays propagation across the object result in correlated functions that must over-sample the object in order to get accurate reconstructions. To reduce such correlated equations, compressive sensing (CS) has been introduced into X-ray CT systems (so-called compressive X-ray CT systems) via coded aperture-based encoding with the aim at partially blocking the propagation of the energy through the object [8,9]. In this way, a certain amount of X-ray energy

---

[8] Yan Kaganovsky et al. “Compressed sampling strategies for tomography”. In: *JOSA A* 31.7 (2014), pp. 1369–1394.

[9] Keijo Hamalainen et al. “Sparse tomography”. In: *SIAM Journal on Scientific Computing* 35.3 (2013), B644–B665.

that impacts the object is supposed to decrease, as well as the incident radiation [9,10], where the reduction of equations is compensated by assuming sparsity in the object [10,11]. The CS asserts the possibility of recovering signals and images from far fewer measurements than those established in the Shannon-Nyquist theorem [12,13]. The recovery is possible based on the sparsity and incoherence principles, where sparsity exploits that many real-world signals are sparse or compressible in a given basis, and incoherence is related to certain randomness in the acquisition of the signal [14]. Formally, the measured data denoted as $\mathbf{p} \in \mathbb{R}^M$ are the projections of the signal $\mathbf{f} \in \mathbb{R}^N$ through the matrix $\mathbf{W} \in R^{M \times N}$, i.e.,

$$\mathbf{p} = \mathbf{W}\mathbf{f}, \tag{1}$$

where $\mathbf{W}$ models the linear measurement process. Thus, the aim is to recover the vector $\mathbf{f}$ by solving the inverse problem. Traditional sampling criteria suggest that the amount of measured data must be at least as large as the signal length N, i.e., $N = M$. This principle has been widely used in optical imaging equipment such

---

10 Ingrid Reiser and Stephen Glick. *Tomosynthesis imaging*. Taylor & Francis, 2014.

11 David J Brady et al. "Compressive tomography". In: *Advances in Optics and Photonics* 7.4 (2015), pp. 756–813.

12 David L Donoho. "Compressed sensing". In: *IEEE Transactions on information theory* 52.4 (2006), pp. 1289–1306.

13 Emmanuel J Candes, Justin K Romberg, and Terence Tao. "Stable signal recovery from incomplete and inaccurate measurements". In: *Communications on Pure and Applied Mathematics: A Journal Issued by the Courant Institute of Mathematical Sciences* 59.8 (2006), pp. 1207–1223.

14 Gonzalo R Arce et al. "Compressive coded aperture spectral imaging: An introduction". In: *IEEE Signal Processing Magazine* 31.1 (2013), pp. 105–115.

as digital cameras [15,16], microscopy [17], and current medical imaging technologies [18]. Now, if $M < N$, the system in (1) becomes under-determined, producing infinite solutions due to its ill-conditionality [19]. As a consequence, the recovery of $\mathbf{f}$ from $\mathbf{p}$ is infeasible without any additional information of the signal. Thus, CS supposes that the signal $\mathbf{f}$ in (1) has coefficients that are sparse in some basis $\boldsymbol{\Psi}$ such that $\mathbf{f} = \boldsymbol{\Psi}\mathbf{u}$ can be approximated by a linear combination of S vectors from $\boldsymbol{\Psi}$, i.e., $\|\mathbf{u}\|_0 = S$, where $\mathbf{u}$ denotes the sparse coefficients vector [12,13]. Hence, (1) can be rewritten as

$$\mathbf{p} = \mathbf{W}\boldsymbol{\Psi}\mathbf{u}. \tag{2}$$

Traditional CS inverse problem formulations exploit the sparsity principle to find a solution of the sparse representation $\mathbf{u}$ by solving a $\ell_2 - \ell_1$-norm convex optimization problem [20] given by

$$\underset{\mathbf{u}}{\operatorname{argmin}} \|\mathbf{p} - \mathbf{W}\boldsymbol{\Psi}\mathbf{u}\|_2^2 + \tau \|\mathbf{u}\|_1, \tag{3}$$

where the ℓ_2 norm is defined as $\|\mathbf{e}\|_2^2 = \sum_j e_j^2$ and the ℓ_1 norm as $\|\mathbf{e}\|_1 = \sum_j |e_j|$.

---

[15] Henry Arguello, Hoover F Rueda, and Gonzalo R Arce. "Spatial super-resolution in code aperture spectral imaging". In: *Compressive Sensing*. Vol. 8365. International Society for Optics and Photonics. SPIE, 2012, pp. 43 –48.

[16] Henry Arguello, Claudia V Correa, and Gonzalo R Arce. "Fast lapped block reconstructions in compressive spectral imaging". In: *Applied Optics* 52.10 (2013), pp. D32–D45.

[17] Christy Fernandez Cull et al. "Identification of fluorescent beads using a coded aperture snapshot spectral imager". In: *Applied optics* 49.10 (2010), B59–B70.

[18] Edson Mojica, Said Pertuz, and Henry Arguello. "High-resolution coded-aperture design for compressive X-ray tomography using low resolution detectors". In: *Optics Communications* 404 (2017). Super-resolution Techniques, pp. 103 –109. DOI: `https://doi.org/10.1016/j.optcom.2017.06.053`.

[19] Emmanuel J Candès and Michael B Wakin. "An introduction to compressive sampling". In: *IEEE signal processing magazine* 25.2 (2008), pp. 21–30.

[20] Simon Foucart and Holger Rauhut. "An invitation to compressive sensing". In: *A mathematical introduction to compressive sensing*. Springer, 2013, pp. 1–39.

In the literature, there exist several specific algorithms that iteratively solve the optimization problem in (3) seeking for high image quality through the iterations [21][22][23][24]. These CS-based reconstruction methods focus on obtaining an approximate value of the features of the scene from the set of coded projections $\mathbf{p}$, where the resolution of the reconstruction is as high as the range allowed by the physical constraints of the acquisition system, e.g., the detector resolution. Additionally, the computational load of the iterative approaches is directly related to the number of measurements and elements to be reconstructed. In contrast, multi-resolution (MR) reconstruction approaches have emerged from image processing as an alternative to alleviate the computational load of restoring the underlying signal [25][26]. More specifically, a MR-based reconstruction method establishes a procedure capable of obtaining a low-resolution reconstruction from the projection of a set of high-resolution objects by introducing a pair of decimation/upscaling matrices in the problem from (3). In this way, it uses an equivalent low-resolution sensing matrix to solve the MR problem. Generally, decimating the matrix involves creating super-pixels (which are elements that contain pixels sharing common properties) in the target low-resolution (LR) sig-

---

[21] Mário AT Figueiredo, Robert D Nowak, and Stephen J Wright. "Gradient projection for sparse reconstruction: Application to compressed sensing and other inverse problems". In: *IEEE Journal of selected topics in signal processing* 1.4 (2007), pp. 586–597.

[22] Joel A Tropp and Anna C Gilbert. "Signal recovery from random measurements via orthogonal matching pursuit". In: *IEEE Transactions on information theory* 53.12 (2007), pp. 4655–4666.

[23] Sathish Ramani and Jeffrey A Fessler. "A splitting-based iterative algorithm for accelerated statistical X-ray CT reconstruction". In: *IEEE transactions on medical imaging* 31.3 (2011), pp. 677–688.

[24] Stephen J Wright, Robert D Nowak, and Mário AT Figueiredo. "Sparse reconstruction by separable approximation". In: *IEEE Transactions on signal processing* 57.7 (2009), pp. 2479–2493.

[25] Xing Wang and Jie Liang. "Multi-resolution compressed sensing reconstruction via approximate message passing". In: *IEEE Transactions on Computational Imaging* 2.3 (2016), pp. 218–234.

[26] Hans Garcia, Claudia V Correa, and Henry Arguello. "Multi-resolution compressive spectral imaging reconstruction from single pixel measurements". In: *IEEE Transactions on Image Processing* 27.12 (2018), pp. 6174–6184.

nal. Super-pixels-based methods are employed to group similar pixels in the image concerning a specific criterion, such that the resulting dimension of the signal is reduced as dictated by the decimation matrix, also applied to facilitate tasks such as classification and detection [27][28][29][30]. Traditional state-of-the-art super-pixel segmentation techniques include the simple linear iterative clustering [31] and the entropy rate segmentation [32]. The MR-based reconstruction has been studied in CS-based recovery for spectral imaging [26] considering the super-pixel segmentation from a LR version of the image. However, up to date, this approach has not been exploited in compressive CT reconstruction, where the use of super-pixels can be directly introduced in the iterative reconstruction procedure instead of computing a LR solution as in [26], for reducing the number of unknowns in the inverse problem.

Besides, the image recovery depends on other factors such as the distribution of the

---

[27] David R Thompson et al. "Superpixel endmember detection". In: *IEEE Transactions on Geoscience and Remote Sensing* 48.11 (2010), pp. 4023–4033.

[28] Yi Chen, Nasser M Nasrabadi, and Trac D Tran. "Simultaneous joint sparsity model for target detection in hyperspectral imagery". In: *IEEE Geoscience and Remote Sensing Letters* 8.4 (2011), pp. 676–680.

[29] Shuzhen Zhang and Shutao Li. "Spectral-spatial classification of hyperspectral images via multiscale superpixels based sparse representation". In: *2016 IEEE International Geoscience and Remote Sensing Symposium (IGARSS)*. IEEE. 2016, pp. 2423–2426.

[30] Pegah Massoudifar, Anand Rangarajan, and Paul Gader. "Superpixel estimation for hyperspectral imagery". In: *Proceedings of the IEEE Conference on Computer Vision and Pattern Recognition Workshops*. 2014, pp. 287–292.

[31] Xuewen Zhang et al. "SLIC superpixels for efficient graph-based dimensionality reduction of hyperspectral imagery". In: *Algorithms and Technologies for Multispectral, Hyperspectral, and Ultraspectral Imagery XXI*. vol. 9472. International Society for Optics and Photonics. 2015, pp. 92–105.

[32] Ming-Yu Liu et al. "Entropy rate superpixel segmentation". In: *CVPR 2011*. IEEE. 2011, pp. 2097–2104.

low-resolution (CA) elements [33][34][18][35][36]. Typically, CS-based acquisition systems rely on CAs for encoding the input signal coming to the acquisition system, where the CA effect in the system in (2) is modeled through the $\mathbf{W}$ matrix structure. These CA are usually composed of randomly distributed block-unblock elements that block or let the information of the object, or its projection, to pass as measurement towards the detector [37]. The design of the CA spatial pattern distribution and its structure has been studied on fields such as compressive spectral imaging (CSI) [34][33][38] and compressive X-ray CT [8][39][35][40][18], since the CA-pattern design has shown higher reconstruction quality images than the random patterns. For instance, authors in [40] introduced a uniform-sensing-based CA design for both the coded aperture snapshot spectral imaging (CASSI) system (in the CSI field) and a compressive CT fan-beam

---

[33] Henry Arguello and Gonzalo Arce. “Colored coded aperture design by concentration of measure in compressive spectral imaging”. In: *IEEE Transactions on Image Processing* 23.4 (2014), pp. 1896–1908.

[34] Claudia V Correa, Henry Arguello, and Gonzalo R Arce. “Spatiotemporal blue noise coded aperture design for multi-shot compressive spectral imaging”. In: *JOSA A* 33.12 (2016), pp. 2312–2322.

[35] Miguel Marquez and Henry Arguello. “Coded aperture optimization for single pixel compressive computed tomography”. In: *Journal of Computational and Applied Mathematics* 348 (2019), pp. 58–69.

[36] Andrés Jerez, Miguel Márquez, and Henry Arguello. “Adaptive coded aperture design for compressive computed tomography”. In: *Journal of Computational and Applied Mathematics* 384 (2021), p. 113174.

[37] Hoover Rueda, Henry Arguello, and Gonzalo R Arce. “DMD-based implementation of patterned optical filter arrays for compressive spectral imaging”. In: *JOSA A* 32.1 (2015), pp. 80–89.

[38] Henry Arguello and Gonzalo R Arce. “Rank minimization code aperture design for spectrally selective compressive imaging”. In: *IEEE transactions on image processing* 22.3 (2012), pp. 941–954.

[39] Angela Cuadros et al. “Coded aperture design for compressive X-ray tomosynthesis”. In: *Computational Optical Sensing and Imaging*. Optical Society of America. 2015, CW2F–2.

[40] Yuri Mejia and Henry Arguello. “Binary codification design for compressive imaging by uniform sensing”. In: *IEEE Transactions on Image Processing* 27.12 (2018), pp. 5775–5786.

system (in the compressive X-ray CT field), where the designed CA showed superior quality image reconstructions respect to non-designed CAs. As a matter of fact, the CASSI-based designs have motivated several research directions in areas such as compressive spectral classification [41][42], compressive fluorescence microscopy [17], spatio-spectral compressive super-resolution [43][15], and X-ray compressive imaging [44][45].

State-of-the-art CA design approaches exploit the concept of coherence of the sensing matrix [46][47][48], since it describes the correlation between the columns of the measurement matrix, and it enables the selection of less-correlated propagation func-

---

[41] Qiang Zhang et al. "Joint segmentation and reconstruction of hyperspectral data with compressed measurements". In: *Applied optics* 50.22 (2011), pp. 4417–4435.

[42] Ana Ramirez et al. "Spectral image classification from optimal coded-aperture compressive measurements". In: *IEEE Transactions on Geoscience and Remote Sensing* 52.6 (2013), pp. 3299–3309.

[43] Hoover F Rueda, Henry Arguello, and Gonzalo R Arce. "On super-resolved coded aperture spectral imaging". In: *Algorithms and Technologies for Multispectral, Hyperspectral, and Ultraspectral Imagery XIX*. vol. 8743. International Society for Optics and Photonics. SPIE, 2013, pp. 421–426.

[44] Kerkil Choi and David J. Brady. "Coded aperture computed tomography". In: *Adaptive Coded Aperture Imaging, Non-Imaging, and Unconventional Imaging Sensor Systems*. Ed. by David P. Casasent et al. Vol. 7468. International Society for Optics and Photonics. SPIE, 2009, pp. 99–108.

[45] Kenneth MacCabe et al. "Pencil beam coded aperture x-ray scatter imaging". In: *Optics Express* 20.15 (2012), pp. 16310–16320.

[46] Angela P Cuadros and Gonzalo R Arce. "Coded aperture optimization in compressive X-ray tomography: a gradient descent approach". In: *Optics Express* 25.20 (2017), pp. 23833–23849.

[47] Bo Li et al. "Projection matrix design using prior information in compressive sensing". In: *Signal Processing* 135 (2017), pp. 36–47.

[48] Vahid Abolghasemi, Saideh Ferdowsi, and Saeid Sanei. "Fast and incoherent dictionary learning algorithms with application to fMRI". in: *Signal, Image and Video Processing* 9.1 (2015), pp. 147–158.

tions to increase the variability of the captured data [49]. However, these strategies entail designing the entire system matrix, which involves both the hardware configuration and the CA effect. Therefore, strong binarization assumptions are required to obtain implementable systems. For instance, in [40] the condition of the system is enhanced with a binarized and rearranged version of the sensing matrix by employing the boundaries of the Gershgorin theorem [50]. Further, most CA designs in compressive X-ray CT have focused on the case in which there is a 1:1 correspondence between the CA and detector elements, such that the physical dimensions of each pixel of the detector array limits the CT image resolution [39408].

The recent advances in CA design for compressive X-ray CT have mainly focused on the multi-shot fan-beam CT system [184036], having in each angular shot of the X-ray source multiple measurements by varying the CA pattern and disregarding the cone-beam CT system (which has advantages such as lower effective radiation doses and faster scan for getting 3D volumes [1]). However, the CA designs for fan-beam X-ray setups cannot be directly applied on cone-beam X-ray systems due to their physical differences.

This dissertation extends the capabilities of the compressive X-ray CBCT architecture by designing the CA patterns under a super-resolution (SR) strategy, so-called super-resolution-CBCT (SR-CBCT), such that higher resolution image reconstructions can be obtained from LR projections captured in a single shot at a given set of angles. Specifically, the proposed CA design in the SR-CBCT system takes advantage of the Gershgorin theorem since its algebraic interpretation relates the circle radii with the eigenvalue bounds, whose minimization improves the condition of the system matrix.

Beyond the main scope of this thesis, two related problems were tackled during the

---

[49] Michael Elad. “Optimized projections for compressed sensing”. In: *IEEE Transactions on Signal Processing* 55.12 (2007), pp. 5695–5702.

[50] S. Gershgorin. “Uber die Abgrenzung der Eigenwerte einer Matrix”. In: *Izvestija Akademii Nauk SSSR, Serija Matematika* 7.6 (1931), pp. 749–754.

state-of-the-art revision; thus, two additional contributions are presented. Firstly, for the CT measurement reconstruction obtained from a fan-beam CT architecture, a multi-resolution reconstruction algorithm was introduced to boost the recovery speed and improve image quality. Secondly, for the CASSI system in spectral image acquisition, a CA optimization design is introduced, considering the physical restrictions of the system. Finally, a moving colored-coded aperture is designed, which improves the reconstruction quality of the spectral data cube and is physically implementable. These characteristics reduce the cost of manufacturing offering high-quality images.

1.1. Research Objectives

The general objective of this dissertation embraces: To introduce, design, and simulate high-resolution coded apertures in an X-ray compressive cone-beam computed tomography system, which allows obtaining high-resolution images from a tridimensional object using low-resolution detectors. The specific objectives include:

- To mathematically model the compressive measurement acquisition of tridimensional objects in an X-ray cone-beam computed tomography system including high-resolution coded apertures and low-resolution detectors.

- To design an algorithm that simulates the mathematical model that describes the compressive cone-beam computed tomography system.

- To develop a mathematical method to determine the structure of the coded apertures used in the reconstruction of super-resolution images in the X-ray cone-beam computed tomography system.

- To evaluate the performance of the super-resolution compressive computed tomography system using the designed coded apertures compared with a non-designed structure and a non-coded system.

1.2. Dissertation Organization

The organization of the dissertation is as follows: Chapter 2 describes the principal theoretical concepts of CT, including the attenuation physical phenomenon, the projection formation from measurements, and the image reconstruction by using the Fourier slice theorem as well as its disadvantages with discrete measurements. Finally, the iterative algebraic reconstruction techniques to recover the underlying signal are also introduced.

Chapter 3 presents the formulation of a CBCT system and extends the concept of sparsity defined in the compressive sensing paradigm, its application to most of the images through a sparsifying basis, and it identifies which basis provides high acceptance in CT applications. Additionally, it provides a brief exploration of the reconstruction optimization problem, identifying an affordable option among the algorithms used to solve a constrained formulation in CS.

Chapter 4 introduces the so-called SR-CBCT system, to design high-resolution CAs with a low-resolution detector array, where the super-resolved images can be recovered without significantly changing the traditional architecture. Therefore, the chapter develops a framework around the concept of the Gershgorin theorem to estimate an approximation of the system matrix condition. Specifically, the CA design is formulated as a coherence minimization problem in which the CA is the design variable. Then, the proposed method reduces the Gershgorin radii of the SR-CBCT system matrix, which describe the eigenvalue distribution bounds for improving the condition of the inverse problem.

Chapter 5 presents the image improvement capabilities of the SR-CBCT system, comparing reconstructions of random blocking-unblocking distributions of the CAs against a set of designed CAs which promotes a radii reduction of the Gershgorin theorem as suggested in the formulation of chapter 4.

Chapter 6 presents the adaptation of the MR concept as a framework applicable to iterative algebraic reconstruction techniques in CT. Evaluating the image reconstruction at each iteration allows the generation of a custom decimation matrix that can be

introduced into a linear problem to perform an analogous optimization function limited in its resolution by the corresponding upsampling transformation. Consequently, each iteration solves the decimated coefficients, reducing the unknowns in the next iteration. The MR-based reconstruction is applied for recovering compressed fan-beam projections.
Chapter 7 presents an alternative CA design in a compressive spectral imaging system, extending the main scope of this dissertation. These CA patterns are subject to select a set of color filters while each snapshot shares a portion of the pattern to reduce the cost of building, achieving a comparable performance against the state-of-the-art CAs.

1.3. List of Contributions

Most of the material presented in this thesis appears in the following publications by the author:

1.3.1. Journal papers

- **Mojica, E.**, Correa, C. V., and Arguello, H. (2021). High-resolution coded aperture optimization for super-resolved compressive x-ray cone-beam computed tomography. Applied Optics, 60(4), 959-970.

- Galvis, L., **Mojica, E.**, Arguello, H., and Arce, G. R. (2019). Shifting colored coded aperture design for spectral imaging. Applied optics, 58(7), B28-B38.

1.3.2. Conference Papers:

- **Mojica, E.**, Garcia, H., and Arguello, H. (2019, April). Impact of Multi-resolution reconstruction on Computed Tomography. In 2019 XXII Symposium on Image, Signal Processing and Artificial Vision (STSIVA) (pp. 1-5). IEEE.

- Galvis, L., **Mojica, E.**, Arguello, H., and Arce, G. R. (2019, May). Optimization of a Moving Colored Coded Aperture in Compressive Spectral Imaging. In

ICASSP 2019-2019 IEEE International Conference on Acoustics, Speech and Signal Processing (ICASSP) (pp. 7685-7689). IEEE.

1.4. Research Contributions

This dissertation proposes a coded aperture design with a higher ratio between coding and detection elements for the X-ray CBCT system. The coding strategy allows getting high-resolution reconstruction images from low-resolution projections with a single shot. The proposed design method uses an optimization problem to reduce the radii of the Gershgorin theorem, exhibiting a gain in quality of the recovered images over the random structures. The results of this contribution were published in the journal in [51].

Additionally, this dissertation shows a multi-shot fan-beam CT system reconstruction framework that transforms the signal to be reconstructed into a lower dimension set. The adaptive process uses the iterative steps of the reconstruction fitting decimation matrix to group similar pixels in a sub-pixel description. Results of the reconstruction process are comparable to state-of-the-art, highly reducing the time consumption of the total number of iterations. This contribution was published in the conference [52].

Extending the coded aperture application to spectral imagery systems embraces flat blocking patterns for each spectral band color. Therefore, this dissertation offered a color-coded aperture design by selecting a pattern distribution from a set of filters. It is worth to remark that the proposed design has been based on a set of filters that follows physical limitations, and has not been previously studied in the literature. The proposed design achieves a performance comparable to the previous state of

---

[51] Edson Mojica, Claudia V Correa, and Henry Arguello. "High-resolution coded aperture optimization for super-resolved compressive x-ray cone-beam computed tomography". In: *Applied Optics* 60.4 (2021), pp. 959–970.

[52] Edson Mojica, Hans Garcia, and Henry Arguello. "Impact of Multi-resolution reconstruction on Computed Tomography". In: *2019 XXII Symposium on Image, Signal Processing and Artificial Vision (STSIVA)*. IEEE. 2019, pp. 1–5.

art distributions, where the filter distribution is not restricted. The results of this contribution were published in the journal in [53] and the conference paper in [54].

[53] Laura Galvis et al. "Optimization of a Moving Colored Coded Aperture in Compressive Spectral Imaging". In: *ICASSP 2019-2019 IEEE International Conference on Acoustics, Speech and Signal Processing (ICASSP)*. IEEE. 2019, pp. 7685–7689.

[54] Laura Galvis et al. "Shifting colored coded aperture design for spectral imaging". In: *Applied optics* 58.7 (2019), B28–B38.

2. Computed Tomography (CT)

X-rays are electromagnetic waves characterized by having a higher frequency than ultraviolet rays but a lower frequency than gamma rays. X-rays are emitted by high-speed electrons colliding with a target element called the anode. The radiation is emitted in terms of photons, each of which has defined energy. X-rays with energy exceeding 100 eV can ionize atoms and penetrate through matter. X-ray photons interact with matter in the form of absorption or scattering. If neither happens, it is transmitted through the object. In the phenomenon of absorption interaction, the energy of X-ray photons is absorbed by the object and transferred to electrons in one of the atomic shells. This phenomenon is known as photoelectric absorption. The process of removing photons from the beam is called attenuation. In general, the attenuation behavior of a particular material at a given energy is measured by the linear attenuation coefficient or mass attenuation coefficient. On the other side, two types of interactions take place in the form of scattering: Compton scattering, and coherent scattering. Both cases are the result of the collision between photons and electrons. As a result, the incident photons are deflected at a certain angle after a collision. In Compton scattering, this occurs due to the interaction of photons with electrons in the outer shell of the atom. The photons transfer part of their energy to the colliding electrons, and both energy and momentum are conserved in the colliding electrons. The incident photon is deflected by a certain angle due to the collision and is scattered from the collision site with energy less than the energy of the incident photon. The impacted electron gains some kinetic energy from the incident photon and recoils. Coherent scattering occurs when low-energy photons collide, which causes the colliding electrons to vibrate at the photon frequency. Thus, energy in the form of X-rays is released due to the vibration of the same frequency and energy as the incident photons. As result, the incident photons that are deviated during the process causing coherent scattering. The process of removing photons from the beam is called attenuation. Generally, the attenuation behavior of a specific material at a given energy is measured by a linear attenuation coefficient or a mass attenuation coefficient, and the Lambert's-Beer law describes his behavior. This chapter guides a brief introduction to the basics of X-ray CT, from the energy projection to its recovery.

2.1. Lambert's-Beer Law on Image Acquisition

The attenuation of X-rays depends on the type of material and the energy of the incident particles. In this phenomenon, the radiation intensity is given by a number of photon particles from the source, having the total emission of energy as the proportion I_0 that relates a group of emitted particles and the thickness of the object dy. The interaction processes characterized with a linear attenuation coefficient of X-rays can be described as the differential equation

$$dI = -fI_0 dy. \tag{4}$$

In this model f is a constant that is known as the linear attenuation coefficient for X-rays. The solution to the formulation introduced on eq.(4) is well-known as the Beer-Lambert formula,

$$I = I_0 e^{-fw}. \tag{5}$$

This equation shows the relationship between the final intensity I and the initial intensity of the incident radiation I_0, which has an exponential decay relationship with the two characteristics of the attenuation medium (linear attenuation coefficient f and object thickness w). The attenuation coefficient f_y along a single thickness section w_y is illustrated in Fig.2(a), where the input intensity I_{y-1} is given by a set of arrows and the output I_y shows the reduction of the set of arrows.
Generally, X-rays are polychromatic in nature [55], and the linear attenuation coefficient

[55] Angela Cuadros, Xu Ma, and Gonzalo R Arce. "Compressive spectral x-ray tomography based

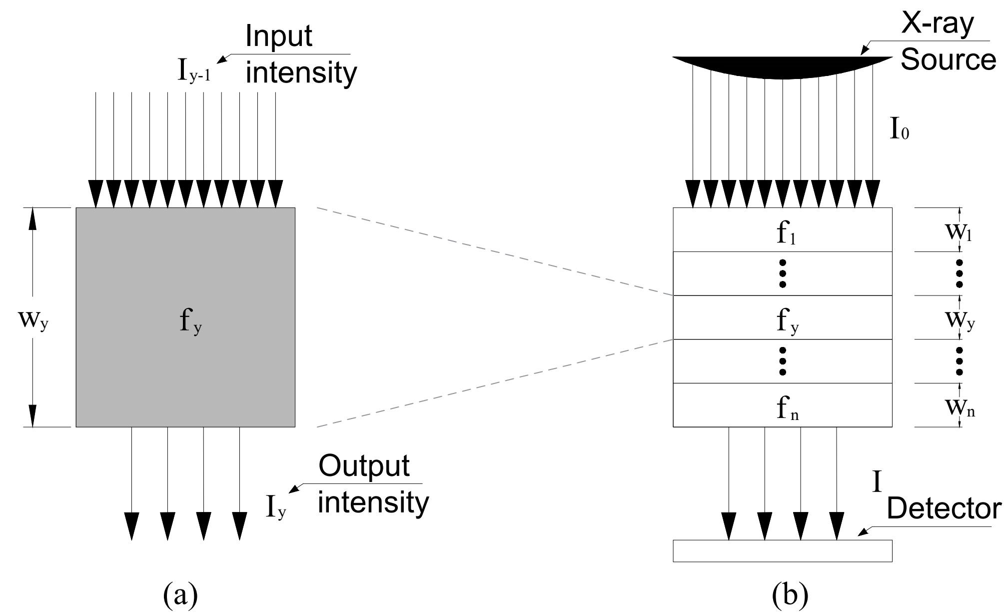

Figure 2. Schematic representation of attenuation for a single X-ray beam through: (a) a single section W_y with attenuation coefficient f_y and (b) the initial energy I_0 crossing multiple sections to produce the output I.

depends on the energy of the particles. For non-homogeneous objects revealing different attenuation materials eq.(5) becomes

$$I = I_0 e^{-f_1 w_1} e^{-f_2 w_2} \cdots e^{-f_n w_n} = I_0 e^{-\sum_{y=1}^{n} f_y w_y}, \tag{6}$$

having n for the total sections that interact with the particles which will travel through the object, each small volume section w_y of the object is associated to an attenuation coefficient f_y as illustrated the Fig.2(b). This formulation indicates the number of considered object portions as voxels that contain the attenuation coefficients to solve in the propagation direction.

The reconstruction process starts from the data acquisition with the aim of obtaining the cross-sectional coefficients f_y of the CT image. Assuming attenuation by Beer-Lambert's law, an ideal model of the photoelectric effect can be processed from the

---

on spatial and spectral coded illumination". In: *Optics express* 27.8 (2019), pp. 10745–10764.

CT acquisition, which allows modeling the system CT from intensity measurements.

2.1.1. Acquisition Process The Eq.(6) from the Beer-Lambert's formulation can be applied to the X-ray CT scanning systems for the image acquisition by tracing photons through a defined space. This space contains the voxels that subdivide the object and relates each weight w_y with the attenuation effect as a parallel, fan, or cone propagation shape of the beams. Initial CT systems were based on the pencil beam configuration to generate a X-ray shape approximation of parallel beams. This kind of configuration requires the emission of energy from the source to the detector and introduces a displacement of the source and the detector to cover the width of the object; then, rotates and repeats the displacement at a different angle as illustrated in the Fig.3.

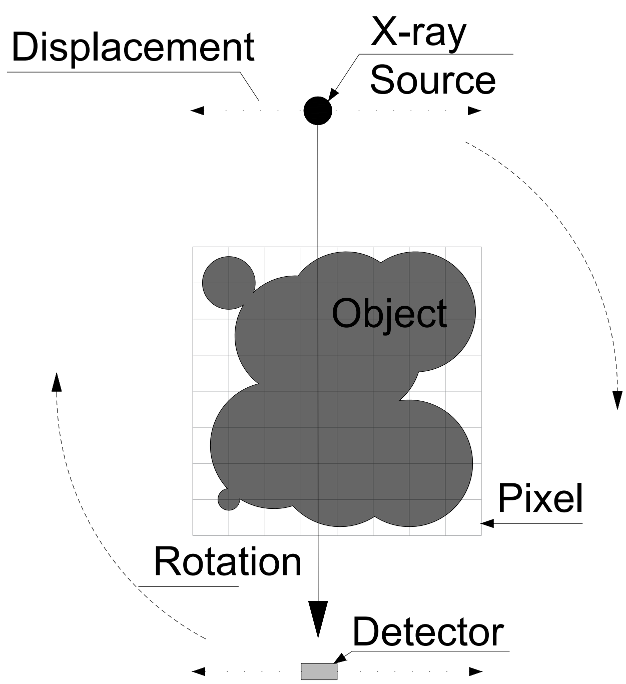

Figure 3. Diagram of a pencil-beam system, jointly displaces and rotates the X-ray source and detector unit to acquire measurements of the intensity of the attenuated beam.

As consequence, pencil beam system is often discarded to be used in medical imaging or industrial imaging applications, due to the high radiation dose dangerous for patients, and extensive on time-consuming related to the long exposure time. Hence, some of the most profitable commercial X-ray CT systems are based on FB and cone-beam computed tomography [56]. FB and CB architectures are the result of variations based on the pencil beam approach. Thus, FB describes a system with a punctual source of X-rays and a linear detector array, generating a fan of energy shape between source and detectors, while a CB system with a matrix detector distribution develops a cone of energy shape between source and detectors. In consequence, these CT systems reduce scanning speed and the radiation dose, because the multiple shots of the source and his displacement at each angle are removed. Systems based on parallel beams or FB provide 2D images of the object from the cross-section of a slice. With the advent of 2D detectors and faster computers, a 3D image reconstruction can be achieved using a CB propagation scheme [56].
In this model, the captured projection p relates the emitted energy I_0 and the output energy I, as in (6) where the logarithm of the ratio between these intensities are expressed as

$$p = -ln\left(\frac{I}{I_0}\right) = \sum_{y=1}^{n} f_y w_y. \quad (7)$$

Moreover, the source emits uniform divergent X-rays with intensity I_0 through the direction of the detection area forming a cone, as shown in Fig. 4. Instead of a single beam there is a set of R trajectories that collides each detector element indexed by $(\hat{\gamma}, \hat{\omega})$ of the 2-dimensional detector array with a total of γ rows and ω columns. Thus, considering a $n \times n$ object $\mathbf{F}$ with v slices whose attenuation coefficients are indexed by f_{xyz}, the interaction of the incoming X-ray energy with object volume sections

---

[56] Jiang Hsieh. *Computed tomography: principles, design, artifacts, and recent advances*. Vol. 114. SPIE press, 2003.

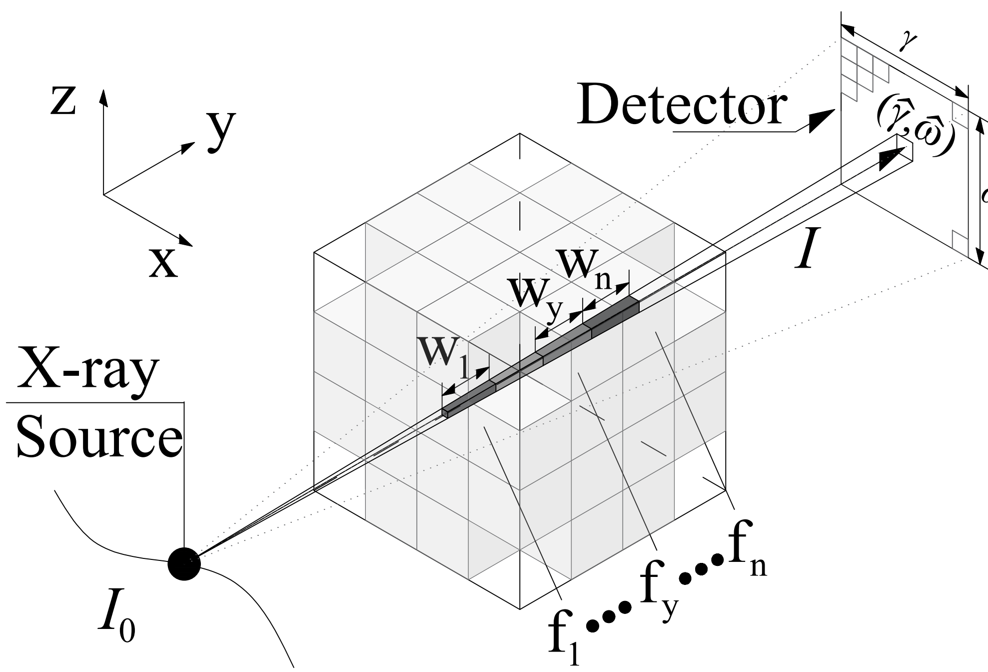

Figure 4. Energy propagation of a single X-ray beam. Energy intensity I_0 follows a linear trajectory towards the detector. Interaction with object sections, produces the attenuated output energy I.

(voxels) w_{xyz} can be written as

$$p_{\hat{\gamma},\hat{\omega},\hat{\theta}} = -\ln\left(\frac{I_{\hat{\gamma},\hat{\omega},\hat{\theta}}}{I_0}\right) \approx \sum_{x=1}^{n}\sum_{y=1}^{n}\sum_{z=1}^{v} w_{xyz} f_{xyz}. \tag{8}$$

Since the system elements (the X-ray source and the detector array) rotate θ angles in a single turn during the acquisition process, $\hat{\theta}$ in Eq.(8) indexes the captured projections at each particular angle. Then, the acquisition process can be stated as the linear problem

$$\tilde{\mathbf{p}} = \mathbf{W}\mathbf{f}, \tag{9}$$

where $\mathbf{f} \in \mathbb{R}^N$ with $N = n^2 v$ represents the object elements rearranged as a vector; the output vector $\tilde{\mathbf{p}} \in \mathbb{R}^{\tilde{M}}$ represents the attenuated intensities captured at the detector for $\tilde{M} = \gamma\omega\theta$ propagation functions; the matrix $\mathbf{W} \in \mathbb{R}^{\tilde{M}\times N}$, whose rows are the weight coefficients w_{xyz} that model the interactions of the X-ray beams with the N object voxels, represented as columns of $\mathbf{W}$.

The mathematical procedures of CT reconstruction can be divided into two major categories: analytical and iterative. Analytical approaches can either use a frequency approach or linear algebra approach. Specifically, frequency approaches as an analytical reconstruction mainly apply the Fourier central slice theorem or filtered back projection (FBP) [1]. Assuming a return of the measured energy to the propagation path of voxels, it is important to notice that the matrix $\mathbf{W}$ performs as many horizontal, vertical, and diagonal paths as measurement angles were used for each detector element.

Thereby, a high-quality image can be obtained by using the proposed linear system (9) when enough independent measurements are taken for each voxel, then, a unique solution can be obtained from the system of equations that describe the coefficient distribution of the object. Even assuming a path of two orthogonal projections, the horizontal path, and vertical path could share a single voxel coefficient; this effect is worse between adjacent or opposite angles, showing that the equations of the system are not linearly independent having highly correlated equations and turning $\mathbf{W}$ into an ill-conditioned system. Since the measurements may not cover the entire object by linearly interacting with an independent voxel, to ensure that enough independent equations can be performed, the number of measurements $\tilde{M}$, must exceed the number of solved elements N. In case of having infinite number of projections, it is possible to assume a continuous behavior of information around the object, which means that $\tilde{M} \approx \infty$. As result, it brings the possibility of taking advantage of analytical reconstructions with high accuracy. However, in the context of real applications, to acquire infinite projections is a highly unlikely task, limiting to have a finite number of registers. Considering that the tomographic sampling elements refer to the number of rays per projection, and the total number of projections refers to the number of registers of the attenuated energy in the detector, projections are limited by a discrete number of detectors and angles, even having infinite photons as sampling elements. Therefore, the reduction of the number of projections impacts the reconstruction quality, increasing artifacts consequence of either data undersampling or the presence of random noise in the measurements.

Current CT scanner use FBP methods for reconstruction but its quality is highly dependent on the sufficient number of projections [1]. In addition, the irregular geometry of the scanner or the loss of data causes serious difficulties for the analytical reconstruction methods. However, using a matrix formalism into a linear problem can accurately represent the acquisition process and treat further behaviors like lack of data, asymmetric elements, or non-uniform motion. Even it is possible to simulate a finite set of detectors, with different heights, widths, and sensitivity. On the other hand, the matrix can take into consideration beams running through objects in directions that produce inconsistencies for analytical models leading a more realistic physical acquisition process. As consequence, this matrix system does not have a simple structure, describing it as a sparse matrix where only $N^{\frac{1}{2}}$ voxels contribute to an entry, doing it almost singular, which means that it contains very small singular values such that the reconstruction is an ill-conditioned problem. This establishes that measurements must be higher than the number of unknowns ($\tilde{M} > N$) to get high-quality reconstructions, followed by an extreme requirement of time and memory in the case of calculating a direct inverse of a matrix.

2.1.2. The Fourier Slice Theorem The most representative theory that establishes most of the reconstruction generalities is known as the Fourier slice theorem. This, is a mathematical procedure that decomposes a function or signal into frequencies. Applying the formulation for 2D slices of the object with a function $f(x, y)$, the Fourier transform $F(\dot{u}, \dot{v})$ is defined as,

$$F(\dot{u}, \dot{v}) = \int_{-\infty}^{\infty} \int_{-\infty}^{\infty} f(x, y) e^{-i2\pi(x\dot{u}+y\dot{v})} dx dy. \tag{10}$$

Assuming the detector and source have been rotated around the origin at an orientation angle $\hat{\theta}$, it is convenient to describe a coordinate system with a rotation such that one axis t is parallel to the x-ray path for the projection with angle $\hat{\theta}$, and an orthogonal axis s to describe the width of a path, as shown in Fig. 5.
Thus, the spatial and rotated coordinate system (s,t) can be given as,

$$\begin{bmatrix} s \\ t \end{bmatrix} = \begin{bmatrix} \cos(\hat{\theta}) & \sin(\hat{\theta}) \\ -\sin(\hat{\theta}) & \cos(\hat{\theta}) \end{bmatrix} \begin{bmatrix} x \\ y \end{bmatrix}. \tag{11}$$

Figure 5 shows how a projection $p(s, \theta)$ is generated by drawing a line across (x, y) plane orthogonal to the detector and arrives at the detector location s at a particular angle $\hat{\theta}$. If the projection is defined using a delta function, it could be referred to as a Radon transformation formulated as,

$$p(s, \hat{\theta}) = \int_{-\infty}^{\infty} \int_{-\infty}^{\infty} f(x, y) \delta(x \cos(\hat{\theta}) + y \sin(\hat{\theta}) - s) dx dy, \tag{12}$$

where $s = x \cos(\hat{\theta}) + y \sin(\hat{\theta})$. Then, the projection $p(s, \hat{\theta})$ can be expressed in terms of the coordinate (s, t) obtaining:

$$p(s, \hat{\theta}) = \int_{-\infty}^{\infty} f(s, t) dt, \tag{13}$$

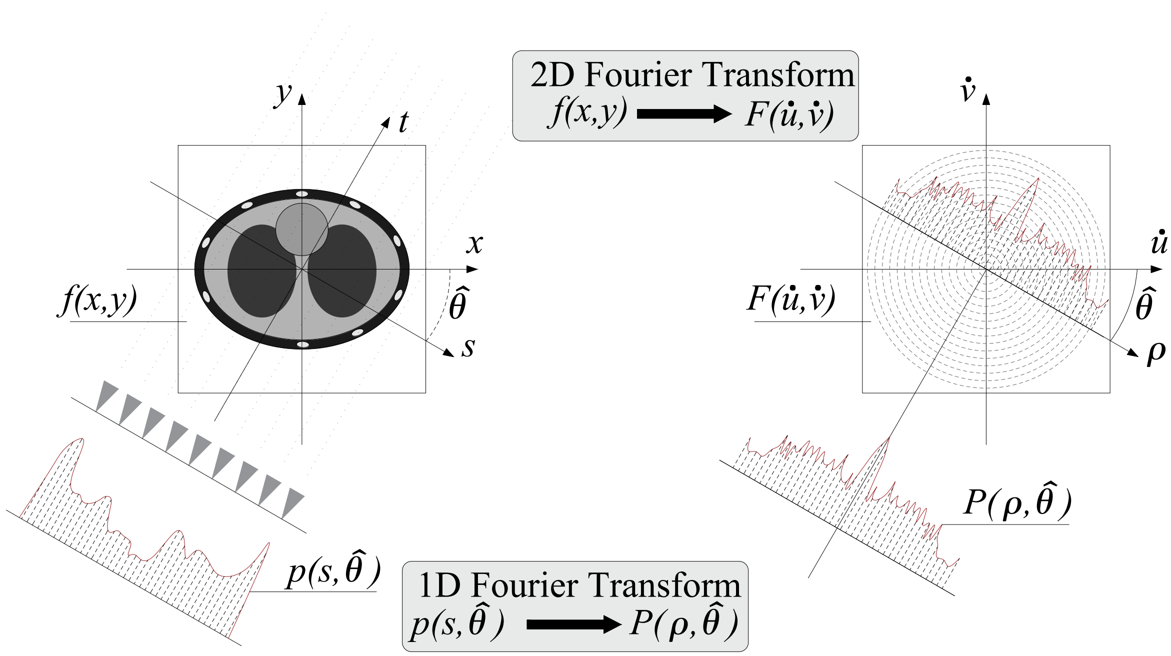

Figure 5. Illustration of the Fourier slice theorem. The 2D image at left is projected at angle $\hat{\theta}$ produce a 1D projection function $p(s, \hat{\theta})$. The 1D Fourier transform $P(\rho, \hat{\theta})$ of this projection is equal to the 2D image Fourier transform, $F(\dot{u}, \dot{v})$ along the radial line ρ at angle $\hat{\theta} + \pi/2$.

where the 1D Fourier transform of the projection $p(s,\hat{\theta})$ gives:

$$P(\rho,\hat{\theta}) = \int_{-\infty}^{\infty} p(s,\hat{\theta}) e^{-i2\pi(\rho s)} ds. \tag{14}$$

Replacing (13) into (14) produce

$$P(\rho,\hat{\theta}) = \int_{-\infty}^{\infty}\int_{-\infty}^{\infty} f(s,t) e^{-i2\pi(\rho s)} dsdt. \tag{15}$$

Substituting (11) into (15), the coordinate system can be transformed to the (x, y) system as,

$$P(\rho,\hat{\theta}) = \int_{-\infty}^{\infty}\int_{-\infty}^{\infty} f(x,y) e^{-i2\pi\rho(x\cos(\hat{\theta})+y\sin(\hat{\theta}))} dxdy. \tag{16}$$

This replacement let notice an equivalence between (10) and (16), been equal in the Fourier transform along one radial line, therefore,

$$P(\rho,\hat{\theta}) = F(\rho\cos(\hat{\theta}), \rho\sin(\hat{\theta})). \tag{17}$$

where $\dot{u} = \rho\cos(\hat{\theta})$,$\dot{v} = \rho\sin(\hat{\theta})$ define a straight line through the origin that forms an angle $\hat{\theta}$ with respect to the $\dot{u}$ axis. This is known as the Fourier slice theorem and states that the Fourier transform of a parallel projection at an angle $\hat{\theta}$ represents the 2D Fourier transform of the object function along a radial line (see Fig.6) at angle $\hat{\theta}$ in Fourier space. Notice that each obtained projection performs a line of the 2D Fourier. Therefore, collecting a sufficient number of projections over the range from 0 to π, it is possible fill the entire Fourier space of the object being reconstructed. This kind of reconstruction exhibits some aliasing artifacts that appear due to the undersampling of projections or by an undersampled grid for displaying.

To avoid this issue, Shannon's sampling theorem defines the number of projections required for accurate reconstruction. The theorem stipulates that if the sampling frequency of an object must be at least twice the highest frequency of the object variation, to obtain a reconstruction without losing information quality. Thus, each sampling point of the projected data is given from a detector element that is identified

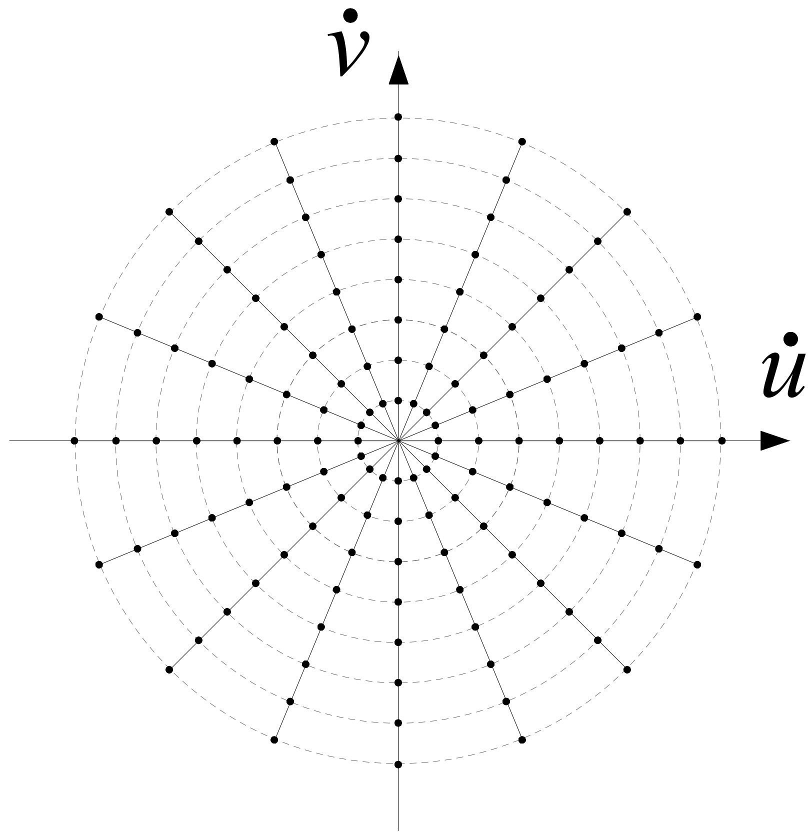

Figure 6. Ilustrative points of the sampling in the Fourier space.

from a set of X-rays. Having that each radial line (e.g. $P_1 - P_1'$ in Fig. 7) represent a projection in Fourier space [57].

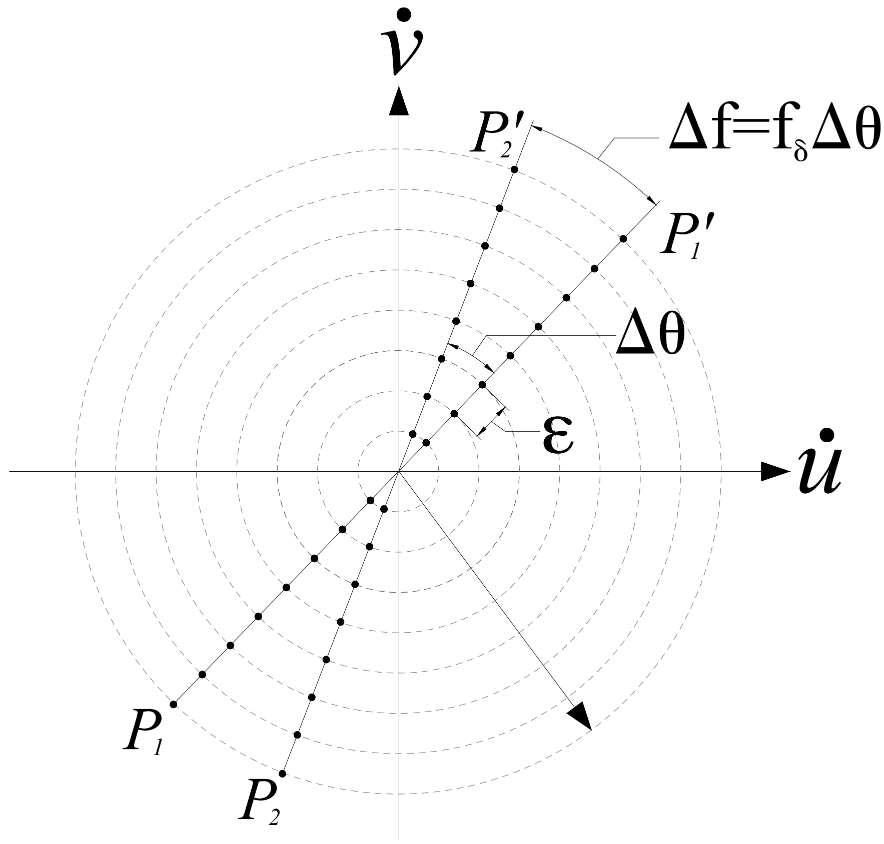

Figure 7. Ilustrative parameters from the frequency domain to the parallel projection data.

Therefore, assuming a set of multiple detectors γ, and that each lecture corresponds to a single ray, there exist a distribution of rays equal to the number of detectors in a projection. In order to complete the Shannon theorem in parallel beam tomography, consider a number of uniform projections distributed on $180°$, the angle transition

---

[57] Avinash C Kak, Malcolm Slaney, and Ge Wang. *Principles of computerized tomographic imaging*. 2002.

between two continuous radial lines in the Fourier domain $\Delta\theta$ is,

$$\Delta\theta = \frac{\pi}{\theta}. \tag{18}$$

For a distance $\Delta\gamma$ between two adjacent rows (detector pixel spacing), the highest spatial frequency (f_δ), named, the sampling points of the outer periphery of the disc, in a projection line that the system can handle is given according to the Nyquist-Shannon theorem,

$$f_{max} = \frac{1}{2\Delta\gamma}. \tag{19}$$

The distance between any two consecutive rays measured on a radial line $P_1 - P_1'$ will be

$$\varepsilon = \frac{2f_\delta}{\gamma} = \frac{1}{\gamma(\Delta\gamma)}. \tag{20}$$

The distance (Δf) between two consecutive sampling points ($P_1'P_2'$) on the periphery of the disc is the azimuth resolution, which is given by

$$\Delta f = f_\delta \Delta\theta = \frac{\pi}{2(\Delta\gamma)\theta}. \tag{21}$$

A sufficient condition to obtain a good reconstruction is to ensure that, the worst azimuth resolution (Δf) in the frequency domain should be approximately the same as the radial resolution (ε) [1]. Therefore, we must have $\Delta f \approx \varepsilon$. Thus

$$\frac{\pi}{2(\Delta\gamma)\theta} \approx \frac{1}{\gamma(\Delta\gamma)} \tag{22}$$

can be reduced to

$$\theta \approx \frac{\pi}{2}\gamma, \tag{23}$$

where (23) implies that the number of projections needed for a good reconstruction is roughly equal to the number of rays in a projection, in other words, the number of elements in a detector. This statement is independent of the reconstruction algorithm. As a general rule, a CT image system should have about as many pixels in each dimension as there are detectors providing data for a view.

Based on the Fourier slice theorem, a complete sampling can be achieved for a 180° rotation because of the symmetry of the projection (see Fig.6) of the line with any arbitrary angular interval. The sampling theorem establishes that the detector spacing has to be small enough to record maximum object frequency, i.e., to detect the smallest possible feature.

2.2. Image Reconstructions Methods

To reconstruct an image based on analytical methods is a computationally high-demanding task because it needs a number of measurements tending to infinity in order to achieve an accurate solution. Thereby, continuous model can be solved as a discrete representation of the system, offering an approximation of the inverse continuous analytical model. This consideration covers two types of analytical reconstruction algorithms often employed on reconstructions: the Fourier slice theorem and the filtered back-projection. For the Fourier slice theorem, consider that the projection data $p(s, \hat{\theta})$ is measured with equal spacing for $\hat{M} = \gamma\theta$ number of projections, thus, the reconstruction strategy can be summarized as follows:

- To calculate the one-dimensional Fourier transform of the measured projection,

$$P(\rho, \hat{\theta}) = \mathcal{F}\{p(s, \hat{\theta})\}. \tag{24}$$

- To arrange the Fourier transformed projection in 2D radial lines using,

$$F(\rho\cos(\hat{\theta}), \rho\sin(\hat{\theta})) = P(\rho, \hat{\theta}). \tag{25}$$

- To resample the data points to a rectangular grid $(\dot{u}, \dot{v})$ using interpolation, as illustrated in Fig. 8.

- To perform the 2D inverse Fourier transform of $F(\dot{u}, \dot{v})$ to restore the objective image as

$$f(x,y) = \mathcal{F}^{-1}F(\dot{u},\dot{v}). \tag{26}$$

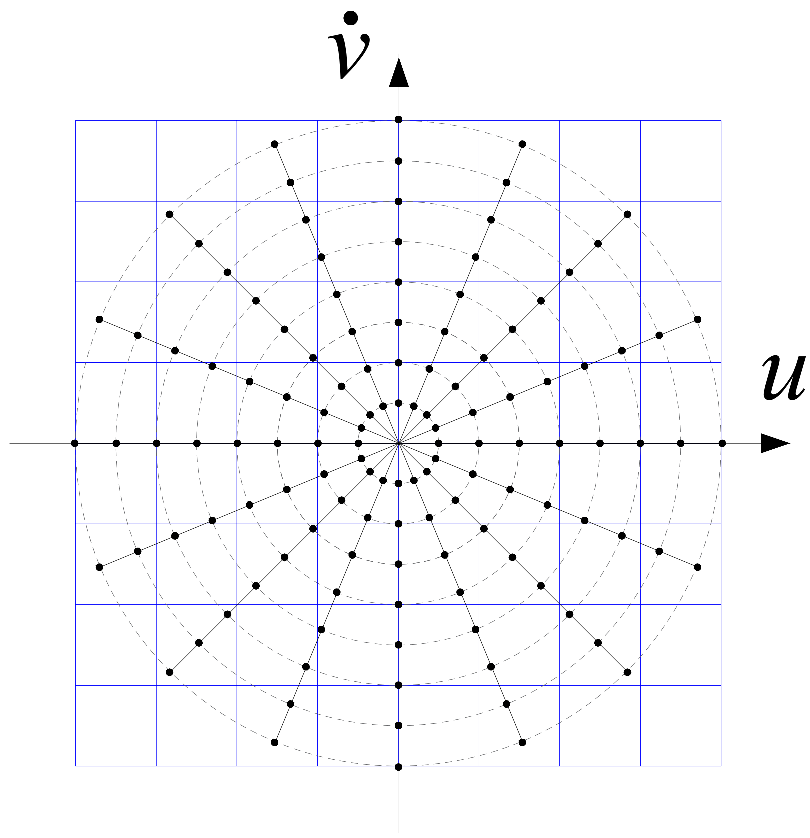

Figure 8. Interpolation grid of the Fourier samples.

The main disadvantage of the Fourier slice theorem is the use of a poor high-frequency data approximation from a polar coordinate grid to a rectangular grid, which will introduce grid errors and produce high-frequency artifacts. This comes from the interpolation in the frequency domain that is not as straightforward as the interpolation of Cartesian space. In a Cartesian space, interpolation error is located around the small region where the value is located. This property does not hold, for interpolation in the Fourier domain, since each sample in a 2D Fourier space, represents certain spatial frequencies. Therefore, an error produced on a single sample of the fourier space affects the entire image.

FBP is a reformulation of the Fourier slice theorem, a method that consists of project data filtered in the frequency domain and back-projecting it onto the image domain. For a 2D object function $f(x,y)$, the inverse Fourier transform $F(\dot{u},\dot{v})$ is defined as,

$$f(x,y)=\int_{-\infty}^{\infty}\int_{-\infty}^{\infty}F(\dot{u},\dot{v})e^{-i2\pi(x\dot{u}+y\dot{v})}d\dot{u}d\dot{v}, \tag{27}$$

where $\dot{u}=\rho\cos(\hat{\theta})$, $\dot{v}=\rho\sin(\hat{\theta})$ and $d\dot{u}d\dot{v}=\rho d\dot{\rho}d\dot{\hat{\theta}}$. This yields

$$f(x,y)=\int_{0}^{2\pi}\int_{0}^{\infty}P(\rho,\hat{\theta})e^{-i2\pi\rho s}\rho d\dot{\rho}d\dot{\hat{\theta}}, \tag{28}$$

where $s=x\cos(\hat{\theta})+y\sin(\hat{\theta})$, and the integral can be split into $\hat{\theta}\in[0,\pi]$ and $\hat{\theta}\in[\pi,2\pi]$, using symmetry properties $F(\rho,\hat{\theta})=F(-\rho,\hat{\theta}+\pi)$, we have to

$$f(x,y)=\int_{0}^{\pi}\int_{-\infty}^{\infty}P(\rho,\hat{\theta})|\rho|e^{-i2\pi\rho s}d\dot{\rho}d\dot{\hat{\theta}}. \tag{29}$$

According to Fourier slice theorem, the 2D Fourier transform of $F(\rho\cos(\hat{\theta}),\rho\sin(\hat{\theta}))=F(\rho,\hat{\theta})=P(\rho,\hat{\theta})$ along the radial line is defined by the Fourier transform of the projection $F(\rho,\hat{\theta})$ as

$$f(x,y)=\int_{0}^{\pi}\int_{-\infty}^{\infty}F(\rho,\hat{\theta})|\rho|e^{-i2\pi\rho s}d\dot{\rho}d\dot{\hat{\theta}}. \tag{30}$$

In (30), the inner integral is the Fourier transform of the projection data with a projection filtering operation with a filtering kernel $|\rho|$. This is a high pass filter which compensates inhomogeneous sampling. To avoid the over enhancement of high-frequency noise and aliasing artifacts, often a smoothing window function is used, such as Hamming window. Then, to apply the FBP process are perform the following steps:

- Calculate the one-dimentional Fourier transform of the projection data.
- Multiply Fourier transform $P(\rho,\hat{\theta})$ with a filter kernel $|\rho|$.
- Backproject the filtered projections onto image domain.

The main disadvantage of analytical algorithms is derived from the assumption that the rays are infinite and continuous. However, in real applications projection data is limited. A drawback handled by the iterative reconstruction (IR) method describing the system as a linear problem with a limited number of measured rays.

2.2.1. Iterative Image Reconstruction The use of IR algorithms is justify since it overcomes the issues of FBP, such as reducing image artifacts and noise elements of the reconstruction process which appears by getting a set of limited projections. In contrast with the analytical method where the filtered projection is back-projected, the IR method provides an iterative solution by refining and modifying the result until satisfying certain criteria [58]. To apply an IR method, it is necessary to formulate the reconstructions carried out using an algebraic reconstruction technique (ART). Even with the widespread use of FBP for CT image reconstructions, ART is more instructive since it represents the reconstruction problem as a linear system of equations.
This requires the discretization of the tomographic images to be reconstructed, and determine the number of voxels N in the field of view where reconstruction takes place. However, the discrete array of unknown variables, f_j, with $j = \{1 \dots N\}$ can be modeled with a linear system of equations. It describes the behavior of the system as a set of projections where the intensity of the X-ray beam through the object is weakened according to the attenuation coefficients f_j of the tissue.
For each X-ray beam through the object, a path of already known image pixels defines a projection as explained in Section 2.1.1. Each propagation equation characterizes its corresponding projection as a linear interaction (7). In contrast to analytical methods, in which the object assumes a sampling with a line of the X-ray beam, the use of algebraic methods proceeds to describe the interactions with the correct assumption that X-ray beams have an area in the wave-front. When passing through tissue, the characterization of equations must regard how much of the voxel to be

---

[58] Jiang Hsieh et al. "Recent advances in CT image reconstruction". In: *Current Radiology Reports* 1.1 (2013), pp. 39–51.

reconstructed is interacting with the beam.
In this case, a weight w_{ij} of a single projection i is determined by the relation

$$w_{ij} = \frac{\text{iluminated area of voxel } j \text{ by the ray } i}{\text{total volume of the voxel } j} \tag{31}$$

and lies in the interval $0 \leq w_{ij} \leq 1$. Considering an X-ray beam traveling between a known position of the source and the detector, a projection geometry can be established to get the weights w_{ij} of a matrix $\mathbf{W}$ by employing the ASTRA Toolbox [59]. The relationship (31) can be extended to a pixel area by assuming a width instead of an area of the wave-front. Stating the problem as (9), the general solution can be described as

$$h(\mathbf{f}) = \underset{\mathbf{f}}{\operatorname{argmin}} \parallel \mathbf{W}\mathbf{f} - \tilde{\mathbf{p}} \parallel_2^2, \tag{32}$$

and its solution is called the least squares minimum norm. ART methods promote iterative strategies to determine a solution of (32) assuming the idea that $\mathbf{f}$ presents a unique solution in a N-dimensional space. Starting with an initial image $\mathbf{f}_0$, it calculates the following results of a sequence of images $\{\mathbf{f}_1, \mathbf{f}_2, \dots\}$ until converge to a desired tomographic reconstruction of the column vector $\mathbf{f}$. In the first step, a forward projection,

$$\tilde{\mathbf{p}}_{(0)} = \mathbf{W}\mathbf{f}_{(0)}, \tag{33}$$

of the z^{th} image approximation $\mathbf{f}_{(z)}$ is determined. The projection, $\hat{\mathbf{p}}_{(z)}$ resolved in the z_{th} forward projection can then be compared with the measured projection, of the column vector $\hat{\mathbf{p}}$. The comparison between the determined and the measured projection yields correction terms that are applied to the z_{th} image approximation, $\mathbf{f}_z$, resulting in the $(z+1)_{th}$ image approximation. This process is repeated to get a projection vector $\hat{\mathbf{p}}_{(z+1)}$. Usually, IR methods are structured into three categories [1] ART, simultaneous algebraic reconstruction technique (SART), and simultaneous

[59] Wim van Aarle et al. “Fast and flexible X-ray tomography using the ASTRA toolbox”. In: *Optics express* 24.22 (2016), pp. 25129–25147.

iterative reconstruction technique (SIRT). Having that a single projection is given by a row vector $\mathbf{w}_i = [\mathbf{W}]_i$, a math formalism of ART is given by:

$$\mathbf{f}_{(z)} = \mathbf{f}_{(z-1)} - \frac{\left(\mathbf{w}_i \mathbf{f}_{(z-1)} - \tilde{p}_i\right)}{\mathbf{w}_i \left(\mathbf{w}_i\right)^{\intercal}} \left(\mathbf{w}_i\right)^{\intercal} . \tag{34}$$

Thereby, (34) implies ART updates the attenuation coefficient value on a ray-by-ray basis and estimates the voxel value based on the difference between a detected pixel value and the calculated pixel value. The difference is back-projected along the ray path length and contributes by correcting each voxel with a proportional value to the path length of the ray inside the voxel. Since the simple ART is computationally expensive and it takes a single ray at a time, the convergence speed is slower compared to FBP. Therefore, the SART method considers one projection at a time introducing as the ART method, by including a relaxation parameter β to the update term. Including the relaxing variation, deals with the over-correction of noise and artifacts and speeds up the convergence time. Turning (34) into :

$$\mathbf{f}_{(z)} = \mathbf{f}_{(z-1)} - \beta \frac{\left(\mathbf{w}_i \mathbf{f}_{(z-1)} - \tilde{p}_i\right)}{\mathbf{w}_i \left(\mathbf{w}_i\right)^{\intercal}} \left(\mathbf{w}_i\right)^{\intercal} . \tag{35}$$

The optimal value, β, depends on the number of iterations of z, the sampling parameters of the system, and the projections. However, a small shift away from the value $\beta = 1$ can increase the convergence speed.

For the case of SIRT methods, all the projections must be processed before the update of the image solution. Convergence speed is further increased by using subsets (OS) [60][61] dividing the projections as groups or subsets and update an estimate for each group instead of updating for the complete dataset. The convergence in-

[60] Ming Jiang and Ge Wang. “Convergence studies on iterative algorithms for image reconstruction”. In: *IEEE Transactions on Medical Imaging* 22.5 (2003), pp. 569–579.

[61] H Malcolm Hudson and Richard S Larkin. “Accelerated image reconstruction using ordered subsets of projection data”. In: *IEEE transactions on medical imaging* 13.4 (1994), pp. 601–609.

creases with a smaller number subset. However, the over-correction leads to higher noise and artifacts due to the increasing number of subsets. For the case where each subset contains a single projection, the scheme is expressed as a SART solution. Otherwise, establishing a subset with all the projections, the scheme becomes a SIRT.

Assuming that each measurement is accurate and not influenced by statistical fluctuations, the scanned object vector $\mathbf{f}$ linked to the matrix system description $\mathbf{W}$, establishes a relationship that maps from $\mathbf{f}$ to its projections $\tilde{\mathbf{p}}$.

In SIRT methods, with a current image estimation, $\mathbf{f}_{(z)}$, finds $\mathbf{f}_{(z+1)}$, identifying a gradient descent approach of the problem (32), having a solution, with the Jacobi derivation of $h(\mathbf{f})$. It allows introduce solutions as stochastic gradient descend as:

$$\mathbf{f}_{(z)} = \mathbf{f}_{(z-1)} - \gamma \nabla h(\mathbf{f}_{(z-1)}) = \mathbf{f}_{(z-1)} - \gamma \mathbf{W}^{\intercal} \left(\mathbf{W} \mathbf{f}_{(z-1)} - \tilde{\mathbf{p}} \right). \tag{36}$$

Thus, introducing variants to reconstruction methods is an attractive field of research, always requiring improving the computational resources or the speed of offering an accurate response. Alternatives for algorithms combine regularization design, i.e., since the linear attenuation coefficient is always positive, it is possible to include a positivity constraint for the pixel solution.

3. Compressive Sensing for CT Image Reconstruction

Traditionally, analytical and iterative CT reconstruction algorithms are used for image recovery from projected data to achieve the limits of the Shannon Nyquist theorem. This theorem establishes the necessity to oversample certain measurements based on the properties of detectors and characteristics of the object discretization to achieve high quality images. In contrast, authors in [1312] showed that if the signal or image itself is sparse without noise, the CS based solution can accurately recover the signal or image from a few linear measurements through optimization. This CS theory integrates the acquisition and compression steps into a single process, hence the name compressed sensing.

In particular, compressive X-ray CBCT approaches rely on CA along multiple view angles to block a portion of the X-ray energy traveling towards the detectors. The inclusion of the CA into the X-ray setups promotes a reduction of the oversampled projections, approaching the sampling scheme to the CS theory. In this chapter, the main concepts of the CS theory applied on CT and CBCT approaches are introduced.

3.1. CBCT Acquisition for CS

A general CBCT scanner, introduced in chapter 2.1.1, incorporates an emitted energy I_0 to a continuous linear trajectory towards the detection area, traversing the object of interest and registering the output energy I, as illustrated the Fig. 4. In addition, since it is assumed that the source uniformly emits divergent X-rays with an intensity of I_0 in direction to the detection area forming a cone of projections over a total of γ rows and ω columns. Thus, considering an object $\mathbf{F}$ depicted with $n \times n$ spatial elements and υ slices, whose attenuation coefficients are indexed by f_{xyz}, and each element interacts with the volume sections w_{xyz} which characterize a propagation path of the emitted energy; the equation (8) describes the attenuation procedure in a three-dimensional object, as illustrated in Fig. 9.

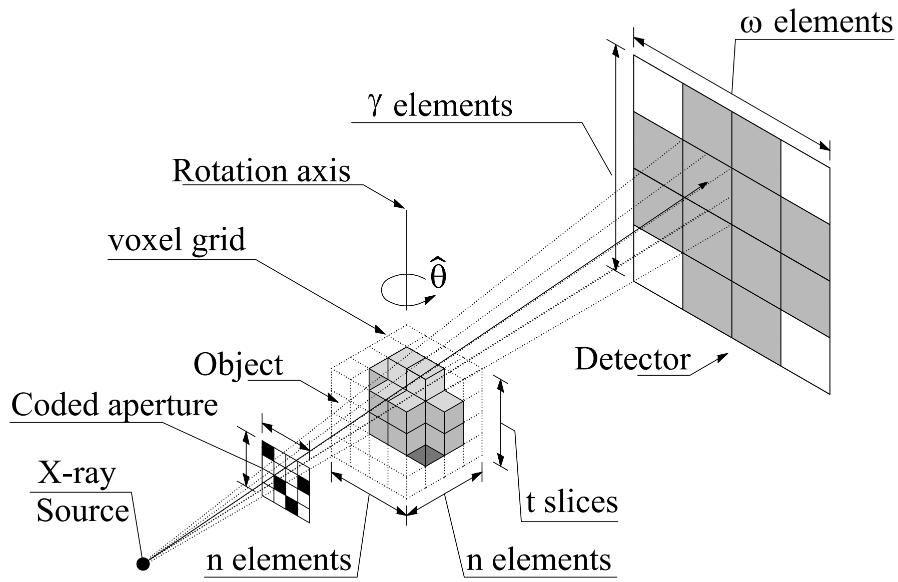

Figure 9. CBCT scheme based on CS theory by including a coding element.

Since the system (the X-ray source, the coded aperture and the detector array) can rotate θ angles in a single turn during the acquisition process, $\hat{\theta}$ in (8) indexes the captured projections at each particular angle indexing the detector by $(\hat{\gamma}, \hat{\omega})$. On the other hand, including a CA between the source and the object, it is possible to describe the system from a reduced set of projections set of projections, turning (8) in a compressive X-ray CBCT architecture. The CA blocks or allows specific X-rays pass through the object, such that the energy intensity reaching the target object can be expressed as $I_c = I_0 e^{-f_c w_c}$, where f_c represents the attenuation caused by the material of the CA features. More specifically, $f_c = 0$ corresponds to the traditional CBCT system, where a CA is not used, i.e., $I_c = I_0$. Similarly, large f_c values represent the blocking operation resulting in a negligible or null projection. In the intermediate cases, a CA works as a coding element in the system. Note that the general compressive CBCT system fixes the CA pitch such that there is a one-to-one correspondence with the elements on the detector array. Thus, introducing the CA effect in (8), the projections in a compressive CBCT system are given by

$$p_{\hat{\gamma},\hat{\omega},\hat{\theta}} = -\ln\left(\frac{I_{\hat{\gamma},\hat{\omega},\hat{\theta}}}{I_c}\right) \approx \sum_{x=1}^{n}\sum_{y=1}^{n}\sum_{z=1}^{v} w_{xyz} f_{xyz}, \tag{37}$$

and can be rewritten as the following linear system

$$\hat{\mathbf{p}} = \mathbf{TWf}, \tag{38}$$

where $\mathbf{f} \in \mathbb{R}^N$, with $N = n^2 v$, represents the object elements rearranged as a vector; the output vector $\hat{\mathbf{p}} \in \mathbb{R}^{\tilde{M}}$ represents the attenuated intensities captured at the detector for $\tilde{M} = \gamma\omega\theta$ propagation functions; the matrix $\mathbf{W} \in \mathbb{R}^{\tilde{M}\times N}$, whose rows are the weight coefficients w_{xyz} that model the interactions of the X-ray beams with the N object voxels, represented as columns of $\mathbf{W}$; and $\mathbf{T} \in \{1, 0\}^{\tilde{M}\times\tilde{M}}$ is a diagonal matrix whose diagonal contains the CA pattern, where the zero values represent the blocking features and the one values represent the X-ray beam pass through the object. The ratio between the total number passing features of the CA, and the total amount of detection pixels defines the transmittance of the system which is given by

$$k = \frac{\sum_{i=1}^{\tilde{M}} \mathbf{T}_{ii}}{\tilde{M}}. \tag{39}$$

Whereas the classical model of CBCT requires $\tilde{M} > N$ projections to reconstruct N object voxels, compressive CBCT enables the reconstruction of the same number of voxels from a fewer amount of projections ($k\tilde{M} < N$), determined by k. In this case, the transmittance promotes a reduction from $\tilde{M}$ to $k\tilde{M}$ propagation functions, which is referred to as the compression of the system. As well as multiple attenuations describe a linear system in the form of (9), it needs to accomplish that the sampling rate is equal to or greater than the Nyquist rate stated in (19), in order to restore the signal

or the image without presence of aliasing artifacts. On the contrary, as declared in [62], this statement is misleading because CS and Nyquist sampling rates perform two different assumptions. The aforementioned Nyquist sampling theorem establishes that a continuous signal limited by a frequency band can be reconstructed accurately. On the other side, CS must find an exact solution with a finite or reduced set of data as in (38), under the premise that CS reconstruction can be given only when the signal composition show to be sparse. Although the images in CT are not sparse, the use of mathematical transforms allows to handle sparse signals, where any target solution can be regarded as processable and reconstructed from CS theory.
These mathematical operations are better known as sparse transformations and can be used to obtain sparse signals describing the image. Generally, the use of a discrete gradient transform or a wavelet transforms [63][12] look increase the image sparsity. With a more sparse signal, the number of unknowns to solve in the sparsified version of the target image solution from the undersampled data needed is lower compared with the spatial image domain of a non-sparse signal. Thereby, solving the sparse elements and applying an inverse sparsifying transform it is possible to return the target image. Even applying the sparsifying transform, an inverse transform is not necessary, needing it only on the reconstruction step. An iterative non-linear optimization procedure can be performed instead of inverse sparsifying transform during the reconstruction process [64]. Therefore, the image reconstruction process in CS is the combination of sparsifying transform and the iterative reconstruction algorithm. The purpose of CS reconstruction is to recover the values of $\mathbf{f} \in \mathbb{R}^N$, from its

---

[62] Xiaochuan Pan, Emil Y Sidky, and Michael Vannier. "Why do commercial CT scanners still employ traditional, filtered back-projection for image reconstruction?" In: *Inverse problems* 25.12 (2009), p. 123009.

[63] Emmanuel J Candès, Justin Romberg, and Terence Tao. "Robust uncertainty principles: Exact signal reconstruction from highly incomplete frequency information". In: *IEEE Transactions on information theory* 52.2 (2006), pp. 489–509.

[64] Yuri Mejia and Henry Arguello Sr. "Filtered gradient reconstruction algorithm for compressive spectral imaging". In: *Optical Engineering* 56.4 (2016), pp. 1 –11.

measurement vector $\hat{\mathbf{p}} = \mathbf{TWf} \in \mathbb{R}^{\tilde{M}}$, where ideally $k\tilde{M} < N$. The CS reconstruction problem for solving $\mathbf{f}$ based on the constrained l_0 minimization problem can be described as:

$$\underset{\mathbf{f}}{\operatorname{argmin}} \parallel \mathbf{\Psi f} \parallel_0 \ \textbf{s.t}\ \hat{\mathbf{p}} = \mathbf{TWf}, \tag{40}$$

where $\mathbf{\Psi}$ is the sparse transformation operator, $\parallel . \parallel_0$ is the l_0-norm of the non-zero component of the vector. Considering that the minimization of l_0-norm is an NP-hard problem [65], and there is instability in the presence of noise [66]. The solution to the l_0-optimization problem is divided into two categories. The first, relax the l_0-optimization through l_1-optimization, which is also called basic pursuit. The second category is defined by iterative greedy algorithms, such as (orthogonal) matching pursuit [22] and iterative hard thresholding (IHT) [67].
In addition, basis pursuit (BP) algorithms rely on linear programming, using a tractable quantity of computational resources and providing stable solutions. In contrast, greedy algorithms are faster, because exploit prior knowledge of the image solution, as consequence, cannot provide the same guarantees BP solution when do not exist any prior information. In the context of CT reconstruction, total variation minimization instead of l_1-optimization provides a sharper image by preserving jumps in the reconstruction as well as the geometry of the boundaries. However, total variation (TV) minimization can only restore an image if the gradient of the underlying target solution is sparse and follows the l_1-optimization.

---

[65] Shanmugavelayutham Muthukrishnan. *Data streams: Algorithms and applications*. Now Publishers Inc, 2005.

[66] Irina Rish and Genady Grabarnik. “Sparse signal recovery with exponential-family noise”. In: *Compressed Sensing & Sparse Filtering*. Springer, 2014, pp. 77–93.

[67] Thomas Blumensath and Mike E Davies. “Iterative hard thresholding for compressed sensing”. In: *Applied and computational harmonic analysis* 27.3 (2009), pp. 265–274.

3.2. Solving a CT Problem with CS

The projections $\hat{\mathbf{p}}$ acquired from $\mathbf{f}$ through the system $\mathbf{TW}$ use CS image reconstruction concept based on the l_0-optimization problem can be treated as a relaxation with the l_1-optimization problem:

$$\underset{\mathbf{f}}{\operatorname{argmin}} \parallel \mathbf{\Psi f} \parallel_1 \ \textbf{s.t}\ \hat{\mathbf{p}} = \mathbf{TWf}, \tag{41}$$

where the l_1-norm $\parallel . \parallel_1$ is defined as the sum of the absolute value of the coefficients that compose the vector. The drawback of (41) is the unrealistic situation of measuring a signal $\mathbf{f} \in \mathbb{R}^N$ with infinite precision. It means that a measurement vector $\hat{\mathbf{p}} \in \mathbb{R}^{\tilde{M}}$ is only an approximation of the vector $\mathbf{TWf} \in \mathbb{R}^{\tilde{M}}$. The corresponding perturbation can be expressed with the l_2-norm of error vector as

$$\parallel \hat{\mathbf{p}} - \mathbf{TWf} \parallel_2 \leq \eta, \tag{42}$$

for some $\eta \geq 0$ parameter which controls data fidelity and a l_2-norm $\parallel . \parallel_2$ denotes the Euclidean norm of a vector. Therefore, the optimization problem is modified to include perturbation as follows

$$\underset{\mathbf{f}}{\operatorname{argmin}} \parallel \mathbf{\Psi f} \parallel_1 \ \textbf{s.t}\ \parallel \hat{\mathbf{p}} - \mathbf{TWf} \parallel_2^2 \leq \eta. \tag{43}$$

The constrained minimization problem can be converted into an unconstrained minimization problem using the Lagrangian approach as

$$\underset{\mathbf{f}}{\operatorname{argmin}}\, \lambda \parallel \mathbf{\Psi f} \parallel_1 + \parallel \hat{\mathbf{p}} - \mathbf{TWf} \parallel_2^2, \tag{44}$$

where λ is a Lagrange multiplier which is also called as regularization parameter. In the literature, the parameter $\parallel \hat{\mathbf{p}} - \mathbf{TWf} \parallel_2^2$ can also be called data fidelity term, and $\parallel \mathbf{\Psi f} \parallel_1$ regularizer term. Data fidelity measures the deviation between measured data and forward-projected expected data. Although the solution of (43) comes from solving (44), this reduces the fidelity bound η. Because of it, is possible to link the output to the basis pursuit de-noising (BPDN) method, which consists of solving (44), for a parameter $\lambda \geq 0$. In addition, the solution of (44) is also related to the output of the LASSO, which consists of solving

$$\underset{\mathbf{f}}{\operatorname{argmin}} \parallel \hat{\mathbf{p}} - \mathbf{TWf} \parallel_2^2 \ \textbf{s.t} \ \parallel \mathbf{\Psi f} \parallel_1 \leq \tau \tag{45}$$

for some parameter $\tau \geq 0$. These alternative noise reduction methods assume CS data affected by additive white Gaussian noise, while a more realistic CT noise model assumes a logarithm-transformed Poisson distribution for projection data obtained from each detector. The differences in the assumption of the noise model promote alternatives of the regularizer term, introducing a custom definition of the l_q-norm dealing with $\parallel \mathbf{f} \parallel_q^q$ which approaches $\parallel \mathbf{f} \parallel_0$ as $q > 0$ tending to zero. It is noticeable the use of the TV-norm as an option particularly accepted on CT reconstructions as an alternative of the l_q-norm, transforming the unconstrained optimization problem in (44) using the TV-norm as,

$$\underset{\mathbf{f}}{\operatorname{argmin}} \, \lambda \parallel \mathbf{f} \parallel_{TV} + \parallel \hat{\mathbf{p}} - \mathbf{TWf} \parallel_2^2 . \tag{46}$$

TV minimization used in image processing as denoising, deblurring, and an inpainting technique [68][69][70] have the goal of recover the original noise-free signal from an additive Gaussian noise signal. TV-norm regularization suppresses noise from segments of the signal that suppose to be constant and reveal steep jumps. The l_1-norm

---

[68] Leonid I Rudin, Stanley Osher, and Emad Fatemi. “Nonlinear total variation based noise removal algorithms”. In: *Physica D: nonlinear phenomena* 60.1-4 (1992), pp. 259–268.

[69] Antonin Chambolle. “An algorithm for total variation minimization and applications”. In: *Journal of Mathematical imaging and vision* 20.1 (2004), pp. 89–97.

[70] Triet Le, Rick Chartrand, and Thomas J Asaki. “A variational approach to reconstructing images corrupted by Poisson noise”. In: *Journal of mathematical imaging and vision* 27.3 (2007), pp. 257–263.

of the TV term in the discrete version can be expressed as the TV-norm as

$$\| \mathbf{f} \|_{TV} = \sum_{x}\sum_{y}\sum_{z} \left|\nabla f(x,y,z)\right|, \tag{47}$$

where $\nabla f(x,y,z)$ corresponds to the spatial distribution of the gradient coefficients on his respective direction (x,y,z). The discrete TV term is expressed as

$$|\nabla f(x,y,z)| = \begin{bmatrix} \nabla_x f(x,y,z) \\ \nabla_y f(x,y,z) \\ \nabla_z f(x,y,z) \end{bmatrix}. \tag{48}$$

Minimizing the value of the TV-norm in the regularization term will cause smoothness in each gradient direction of a reconstruction process of the image processing. However, in CT applications, the free-noise image is not a piecewise constant signal, and pop-up or block artifacts can be introduced during the reconstruction process. Therefore, the reconstructed image will have a lost contrast due to over-smoothing [71]. This problem faced on the state of the art of CS framework by using variants proposed for the aforementioned optimization methods.

3.3. Alternative Optimization Algorithms

The CS concept in CT reconstruction can be implemented in two forms, either with a constrained minimization problem achieving a solution for an objective function within a small data fidelity norm, or an unconstrained minimization problem reducing the data fidelity error to reach a certain tolerance in the regularizer term of the minimization process. The numerical solution of the constrained or the unconstrained minimization is an optimization problem. There are a large number of algorithms

[71] Maurice Debatin et al. "CT reconstruction from few-views by anisotropic total variation minimization". In: *2012 IEEE Nuclear Science Symposium and Medical Imaging Conference Record (NSS/MIC)*. IEEE. 2012, pp. 2295–2296.

available in the literature, but not a unique optimization algorithm available for CT reconstruction. It depends on the accuracy needed in a particular application where the reconstruction is subject to get a solution of an optimization algorithm. Optimization algorithms include first-order methods and their variants, such as steepest-descent or gradient method [21] and accelerated first order method proposed by Nesterov [72]. These optimization algorithms can be adjusted to take into account the regularization term to induce smoothness.

Following the CS theory, when a sparsity prior is assumed, it is possible to recover a high-resolution 3D object from the set of projections (38) such that $\mathbf{f}$ has a representation $\mathbf{u} = \mathbf{\Psi}\mathbf{f}$, and $\mathbf{\Psi}$ describes the sparse representation basis which is incoherent concerning to the sensing matrix $\mathbf{TW}$ [13], and $\mathbf{u}$ is a vector that contains the sparse coefficients of the object. Thus, the reconstruction problem of the sparse elements expressed by a convex optimization form is

$$\mathbf{f}^{*} = \mathbf{\Psi}^{\intercal} \left\{ \underset{\mathbf{u}}{\operatorname{argmin}} \frac{1}{2} \parallel \mathbf{TW}\mathbf{\Psi}^{\intercal}\mathbf{u} - \hat{\mathbf{p}} \parallel_2^2 + \tau \mathbf{\Phi}(\mathbf{u}) \right\}, \tag{49}$$

where τ is a regularization parameter, and the operator $\mathbf{\Phi}$ involves a regularization function over the coefficients, such as the ℓ_1 norm with a given basis $\mathbf{\Psi}$ induces a sparsity solution term. Alternatively, the convex problem can be expressed as

$$\mathbf{f}^{*} = \underset{\mathbf{f}}{\operatorname{argmin}} \frac{1}{2} \parallel \mathbf{TWf} - \hat{\mathbf{p}} \parallel_2^2 + \tau \mathbf{\Phi}(\mathbf{f}), \tag{50}$$

for the TV function. In general, the convex optimization problem (49) can be solved through solutions as primal-dual methods [73], dual formulation [69], second-order cone

[72] Ilya Sutskever et al. "On the importance of initialization and momentum in deep learning". In: *International conference on machine learning*. PMLR. 2013, pp. 1139–1147.

[73] Antonin Chambolle and Thomas Pock. "A first-order primal-dual algorithm for convex problems with applications to imaging". In: *Journal of mathematical imaging and vision* 40.1 (2011), pp. 120–145.

programming [74], Bregman distance method [23] and alternating direction method of multipliers (ADMM) [75]. Identifying fast and accurate alternatives to solve (46) include: gradient projection for sparse reconstruction (GPSR)[21]; fast iterative shrinkage-thresholding algorithm (FISTA)[76]; two-step iterative shrinkage-thresholding (TwIST)[77]; sparse reconstruction through separable approximation (SpaRSA) [24]. In contrast, the split enhanced Lagrangian shrinkage algorithm (SALSA) overcomes the image reconstruction process of GPSR, TwIST, FISTA, and SpaRSA algorithms [78]. Thereby, a constrained split enhanced Lagrangian shrinkage algorithm (C-SALSA) version of the unconstrained SALSA algorithm can be given by applying a variable splitting operation; as a variant of the ADMM algorithm an alternative that stand out in time excecution as in performance of the solution [79][80].

---

[74] Donald Goldfarb and Wotao Yin. "Second-order cone programming methods for total variation-based image restoration". In: *SIAM Journal on Scientific Computing* 27.2 (2005), pp. 622–645.

[75] Se Young Chun, Yuni K Dewaraja, and Jeffrey A Fessler. "Alternating direction method of multiplier for tomography with nonlocal regularizers". In: *IEEE transactions on medical imaging* 33.10 (2014), pp. 1960–1968.

[76] Amir Beck and Marc Teboulle. "A fast iterative shrinkage-thresholding algorithm for linear inverse problems". In: *SIAM journal on imaging sciences* 2.1 (2009), pp. 183–202.

[77] José M Bioucas-Dias and Mário AT Figueiredo. "A new TwIST: Two-step iterative shrinkage/thresholding algorithms for image restoration". In: *IEEE Transactions on Image processing* 16.12 (2007), pp. 2992–3004.

[78] Mario AT Figueiredo, Jose M Bioucas-Dias, and Manya V Afonso. "Fast frame-based image deconvolution using variable splitting and constrained optimization". In: *2009 IEEE/SP 15th Workshop on Statistical Signal Processing*. IEEE. 2009, pp. 109–112.

[79] Jonathan Eckstein and Dimitri P Bertsekas. "On the Douglas—Rachford splitting method and the proximal point algorithm for maximal monotone operators". In: *Mathematical Programming* 55.1 (1992), pp. 293–318.

[80] Manya V Afonso, José M Bioucas-Dias, and Mário AT Figueiredo. "Fast image recovery using variable splitting and constrained optimization". In: *IEEE transactions on image processing* 19.9 (2010), pp. 2345–2356.

4. CBCT Super-resolution Coded Aperture Design

Previous works have shown that designing CA patterns provides improved images. Most designs, are focused on multi-shot FB systems, handling a 1:1 ratio between CA features and detector elements. In consequence, image resolution is subject to the detector pixel size. Moreover, CA optimization for CT involves strong binarization assumptions, impractical data rearrangements, or computationally expensive tasks such as singular value decomposition. Instead of using higher resolution CA distributions into a multi-slice system with a more dense detector array, this chapter presents an arrangement for the CBCT system using a high-resolution CA, defining the SR-CBCT system. To this end, the Gershgorin theorem is exploited in the CA optimization given that its algebraic interpretation relates the circles radii with the eigenvalue bounds, whose minimization improves the condition of the SR-CBCT system matrix. The proposed mathematical framework for designing super-resolution CA for compressive CBCT based on the Gershgorin theorem is described, as well as the cost function to obtain the CA structure and reduce the Gershgorin bounds.

4.1. Super-Resolution Cone-Beam Computed Tomography System

X-ray CT scanners are mainly composed of a source of X-ray energy and an array of detectors that capture information about the inner configuration of an object at several angle views, which allows estimating its structural composition [1]. To this end, industrial applications like quality control [3] and security inspection [456], can employ a moving base to rotate the object [7]. On the other hand, in medical applications, the X-ray source and the detector array jointly rotate around the patient [2]. Describing a CS-CBCT system, in which there is one-to-one correspondence between the detector and CA elements, the attainable image quality depends on the resolution of the detector. Thus, low-resolution detectors cause several propagation lines to interact with large object volume sections, resulting in a loss of detail in the captured

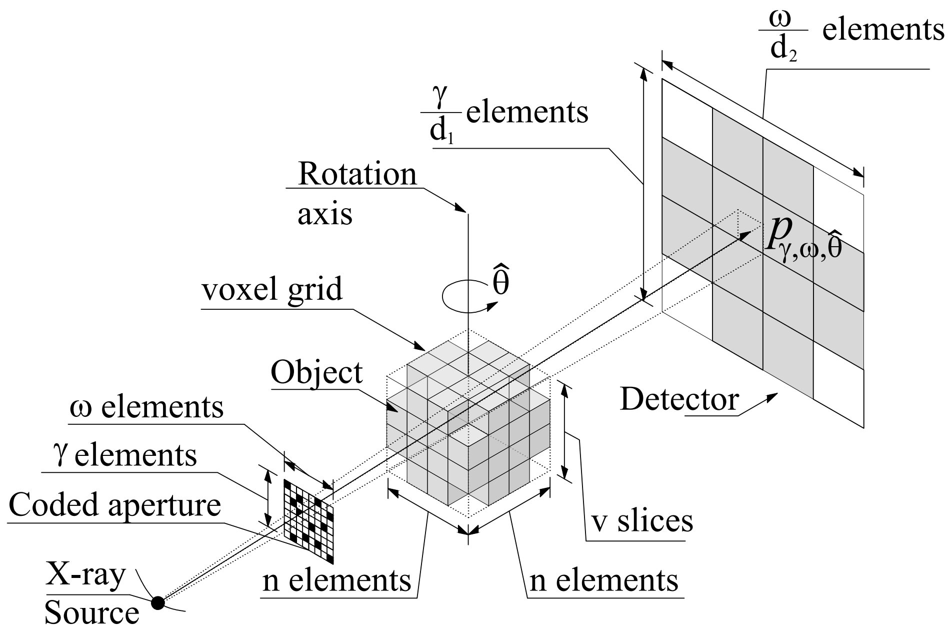

Figure 10. Compressive super-resolution CBCT system that includes a high-resolution CA and a low-resolution detector array.

projections. Better-resolved projections imply increasing the number of detector elements per unit area, that in turn, raises the cost of the system and depends on the manufacturing size limits of sensor components. Conversely, the SR-CBCT model proposed in this work employs CA of higher-resolution with lower-resolution detectors, such that the correspondence between the detector and CA features is greater than one, i.e. a single detector element captures projections from more than one propagation line, describing smaller object voxels. The ratio between the CA and detector features is denoted as $d = d_1 d_2$, where d_1 corresponds to the rows ratio and d_2 to the columns as shown in Fig. 10. Note that this approach allows the discrimination among multiple (d) propagation lines captured at each detector element. Mathematically, this effect can be modeled as

$$\mathbf{p} = \mathbf{D}\hat{\mathbf{p}} = \mathbf{DTWf}, \tag{51}$$

where $\mathbf{D} \in \mathbb{R}^{M \times \tilde{M}}$ is a decimation operator, whose rows integrate d high resolution projections at each detector pixel. More precisely, the $\left(\hat{\imath}, \hat{\jmath}\right)$ $-$th entry of $\mathbf{D}$ is given by

$$(\mathbf{D})_{\hat{\imath},\hat{\jmath}} = \begin{cases} 1, & \text{if } \hat{\imath} = a\{\hat{\jmath}\} + \left\lceil \frac{\gamma}{d_1} \right\rceil \left(b\{\hat{\jmath}\} + \left\lceil \frac{\omega}{d_2} \right\rceil \left(\left\lceil \frac{\hat{\jmath}}{\gamma\omega} \right\rceil - 1 \right) \right) \\ 0, & \text{otherwise} \end{cases}, \tag{52}$$

for $\hat{\jmath} = 1, \cdots, \gamma\omega\theta$ columns and, $\hat{\imath}\{\hat{\jmath}\}$ rows, with $a\{\hat{\jmath}\} = \frac{\hat{\jmath} - \gamma \left\lceil \frac{\hat{\jmath}}{\gamma} \right\rceil + \gamma}{d_1}$ and $b\{\hat{\jmath}\} = \frac{\left\lceil \frac{\hat{\jmath}}{\gamma} - \omega \left\lceil \frac{\hat{\jmath}}{\gamma\omega} \right\rceil + \omega \right\rceil}{d_2} - 1$. At this point, it is noticeable that the total amount of energy from X-rays that are decimated and arrived at the detector is equivalent to the total amount of energy from X-rays that pass through the CA. Independently if there exists decimated information that arrives at the detector which comes from a total, partial, or from applying a null blockage on the CA. For this reason, the definition of the transmittance given as (52) is used in order to quantify the number of equations characterized in the propagation (assumed proportional to the total energy) which passes through the CA and arrives at the detector array.
The SR-CBCT system modeled in (51), allows redefining the solution in (50) as

$$\mathbf{f}^* = \underset{\mathbf{f}}{\operatorname{argmin}} \frac{1}{2} \parallel \mathbf{DTWf} - \mathbf{p} \parallel_2^2 + \tau \mathbf{\Phi}\left(\mathbf{f}\right), \tag{53}$$

with a TV function constraint $\mathbf{\Phi}\left(\mathbf{f}\right)$, where the convex optimization problem (53) can be solved through basis pursuit [81], basis pursuit de-noising [81], least absolute shrinkage and selection operator [82] and least angle regression [83]. Recently, the C-SALSA

[81] Scott Shaobing Chen, David L Donoho, and Michael A Saunders. “Atomic decomposition by basis pursuit”. In: *SIAM review* 43.1 (2001), pp. 129–159.

[82] Robert Tibshirani. “Regression shrinkage and selection via the lasso”. In: *Journal of the Royal Statistical Society: Series B (Methodological)* 58.1 (1996), pp. 267–288.

[83] Bradley Efron et al. “Least angle regression”. In: *The Annals of statistics* 32.2 (2004), pp. 407–499.

[84] has been introduced as an alternative method to solve (53) at lower computational complexity. Disregarding the effect of different algorithms, the reconstruction quality in SR-CBCT is also associated with the amount of captured projections, which depends on the number of multiplexed elements that pass through the CA.

4.2. State-of-the-Art of CT-CA designs

CBCT is a particular CT system configuration that employs a single X-ray source and a flat detection area, such that multiple object slices are captured at each acquisition angle [7]. CBCT acquisition has been modeled as a linear problem, in which each row of the acquisition matrix describes the interactions between the object and the X-ray beams to generate the projections [1]. In general, radiation damage, temperature, misalignment, and changes in x-ray beam intensity are sources of error that entail either an under-estimation or over-estimation of the pixels in the underlying image [85]. To reduce the effects of these errors, several redundant projections are commonly acquired. Thus, the linear system becomes over-determined because of the multiple angle views and projections [1]. Despite the over-determined system enables improved CT image reconstructions, the complexity of the problem increases due to the large amount of involved data. To overcome these limitations, compressive CT introduces a CA to reduce the highest row correlations by blocking similar propagation functions [11]. In particular, the interaction of the CA with the X-rays allows capturing undersampled data with sparse views [89] or missing data at every single view [8]. Consequently, the amount of X-ray energy that impacts the object is supposed to decrease as well as the incident radiation [9][10].

Multiple strategies have been developed to design the CA projection patterns in CT

---

[84] Manya V Afonso, José M Bioucas-Dias, and Mário AT Figueiredo. “An augmented Lagrangian approach to the constrained optimization formulation of imaging inverse problems”. In: *IEEE Transactions on Image Processing* 20.3 (2011), pp. 681–695.

[85] Xiaoquan Yang et al. “Abnormal pixel detection using sum-of-projections symmetry in cone beam computed tomography”. In: *Optics express* 20.10 (2012), pp. 11014–11030.

systems [10][11]. Initial studies showed that in an architecture where the CA pattern is not designed, the use of random CA for equidistant rotation angles provides correct CT reconstructions [4][88]. To date, research on CA design has introduced better distributions than pure random sampling to obtain improved reconstructions [8]. In general, the concept of coherence of the sensing matrix is used, since it describes the correlation between the columns of the measurement matrix [49], and it enables the selection of less-correlated propagation functions to increase the variability of the captured data. For instance, the work in [86] exploits the diffraction of X-rays to analytically design a polar CA plane; in [39][87] coded apertures are designed by analyzing the coherence of the sensing matrix in a tomosynthesis system; the computational cost of the design from [87] was improved in [88]; the rotation of the source and detectors of a fan-beam system was explored in [46], but these rotations increase the computational requirements of the CA design strategies. A recent approach employs sparse principal component analysis (SPCA) to design the CA patterns for a fan beam system [89], which requires sacrificing precision to alleviate the computational complexity of the approach.

In general, state-of-the-art CA design approaches solve the coherence minimization problem by training algorithms to use dictionaries [90], or using gradient descent

---

86 David J Brady et al. "Coded apertures for x-ray scatter imaging". In: *Applied optics* 52.32 (2013), pp. 7745–7754.

87 Angela P Cuadros et al. "Coded aperture optimization for compressive X-ray tomosynthesis". In: *Optics express* 23.25 (2015), pp. 32788–32802.

88 A Parada-Mayorga, A Cuadros, and GR Arce. "Coded aperture design for compressive X-ray tomosynthesis via coherence analysis". In: *Biomedical Imaging (ISBI 2017), 2017 IEEE 14th International Symposium on*. IEEE. 2017, pp. 44–47.

89 Tianyi Mao et al. "Coded Aperture Optimization in X-Ray Tomography via Sparse Principal Component Analysis". In: *IEEE Transactions on Computational Imaging* 6 (2020), pp. 73–86. DOI: 10.1109/TCI.2019.2919228.

90 Julio Martin Duarte-Carvajalino and Guillermo Sapiro. "Learning to sense sparse signals: Simultaneous sensing matrix and sparsifying dictionary optimization". In: *IEEE Transactions on Image Processing* 18.7 (2009), pp. 1395–1408.

algorithms [46][47][48]. However, these strategies entail the design of the entire system matrix, which involves both the hardware configuration and the CA effect. Therefore, strong binarization assumptions are required to obtain implementable systems. For instance, in [40] the condition of the system is enhanced with a binarized and rearranged version of the sensing matrix by employing the boundaries of the Gershgorin theorem [50]. Moreover, most CA designs in CT focus on the case in which there is a 1:1 correspondence between the CA and detector elements, such that the physical dimensions of each pixel of the detector array limit the CT image resolution. Although, the traditional solution for increasing the image resolution consists of employing detectors with smaller pixels, this approach implies higher implementation costs. In contrast, SR methods produce better resolved images without considerably modifying the architecture. For instance, high-resolution CA were designed in [18][35] for a multi-shot fan beam system, assuming that a single detector interacts with a group of CA elements of lower aspect ratio, enabling higher resolution acquisitions with low-resolution detectors. However, the work in [35] explores the limits of the aspect ratio relationship, using a single-pixel detector and substantially increasing the number of shots.

More recently, high-resolution modulations were studied in [91], where sparse and periodical high-resolution CA were used on a fan-beam system with non-conventional acquisition orbits to obtain high-resolution images, at the expense of several shots per angle required by periodic CA patterns. It is worth noting that the aforementioned CA designs cannot be directly applied to CBCT due to the differences between sensing schemes of these architectures. Further, CA designs have not been to date developed for super-resolution compressive CBCT because of the extremely heavy computational costs of handling its system matrix. Therefore, this work presents a CA design approach for compressive SR-CBCT such that higher resolution image reconstructions can be obtained from low-resolution projections captured in a single

[91] O Sefi et al. "X-ray imaging of fast dynamics with single-pixel detector". In: *Optics Express* 28.17 (2020), pp. 24568–24576.

shot. To this end, the CA design is formulated as a coherence minimization problem in which the CA is the design variable, thus, ensuring implementable solutions. More precisely, the design includes the minimization of a function that evaluates the radii of the Gershgorin theorem [50] on the Gram matrix, and the homogeneity distribution of the high-resolution information that impacts the low-resolution detector. The problem is solved through a gradient descent algorithm, subject to a non-linear thresholding operator that controls the number of non-blocking elements as a binary response.

4.3. System Matrix Conditioning by the Gershgorin Theorem

Consider the general linear problem of the form $\mathbf{p} = \mathbf{H}\mathbf{f}$, where $\mathbf{H} \in \mathbb{R}^{M\times N}$ represents an acquisition system matrix, whose rank, i.e. number of linearly independent column vectors, is determined by the ratio between its maximum and minimum eigenvalues.

A more concentrated eigenvalue distribution is evidence of a well-conditioned system. This span could be directly associated with the singular value decomposition (SVD) of $\mathbf{H}$. Considering that a rank of $\mathbf{H}$ or a Gram matrix $\mathbf{G} = \mathbf{H}^{\intercal}\mathbf{H}$ is the same [92], instead of calculating the SVD, which is a computationally expensive task, the Gershgorin theorem [93] can be employed to analyze its eigenvalue bounds, assuming that it is a strictly diagonally dominant matrix (SDDM), mathematically defined as

$$|[\mathbf{G}]_{ii}| \geq \sum_{j} |[\mathbf{G}]_{ij}| \text{ for } i = 1, \cdots, N \text{ and } j \neq i. \tag{54}$$

More precisely, the Gershgorin theorem establishes that the SDDM condition can be used to estimate the bounds that contain the eigenvalues λ_i, if the sum of the module of the elements along the $i-th$ row of $\mathbf{G}$, excluding the diagonal element $[\mathbf{G}]_{ii}$ is less

[92] D.C. Lay, S.R. Lay, and J. McDonald. *Linear Algebra and Its Applications*. Always Learning. Pearson Education Limited, 2016.

[93] Howard E Bell. "Gershgorin's theorem and the zeros of polynomials". In: *The American Mathematical Monthly* 72.3 (1965), pp. 292–295.

than the diagonal entry $[\mathbf{G}]_{ii}$. Thus, every eigenvalue of the matrix $\mathbf{G}$ is contained on the boundary of circles satisfying

$$|\lambda_i - [\mathbf{G}]_{ii}| \leq \sum_j |[\mathbf{G}]_{ij}| \text{ for } j \neq i. \tag{55}$$

The radius of the circle centered at the point $[\mathbf{G}]_{ii}$ is given by $[\mathbf{g}]_i = \sum_j |[\mathbf{G}]_{ij}|$ for $j \neq i$, and each eigenvalue λ_i satisfies

$$[\mathbf{G}]_{ii} - [\mathbf{g}]_i \leq \lambda_i \leq [\mathbf{G}]_{ii} + [\mathbf{g}]_i. \tag{56}$$

Given the SDDM characteristics of $\mathbf{G}$, it is possible to reduce the eigenvalue bounds by reducing the corresponding circle radii on the Gershgorin theorem. Mathematically, the radii reduction impacts the total bound that contains the eigenvalues as

$$\min_i \{[\mathbf{G}]_{ii} - [\mathbf{g}]_i\} \mathbf{1} \preceq \boldsymbol{\lambda} \preceq \max_i \{[\mathbf{G}]_{ii} + [\mathbf{g}]_i\} \mathbf{1}, \tag{57}$$

where $\boldsymbol{\lambda}$ represents a vector containing all the eigenvalues, the vector with lower limit in (57) reveals the minimum possible eigenvalue, and the higher limit describes the maximum possible eigenvalue. Note, that these bounds can still be minimized since circles centers are not necessarily close to each other, even though their radii are minimal. Thus, its assumed a normalized sensing matrix $\mathbf{H}$ that in turn yields to concentric Gershgorin circles with $[\mathbf{G}]_{ii} = 1$ and different radii, such that the eigenvalue bounds in (57) can be reduced by just minimizing the radii $\mathbf{g}_i$. On the other hand, the matrix $\hat{\mathbf{G}} = \mathbf{H}\mathbf{H}^{\intercal}$ holds the same SDDM characteristics as $\mathbf{G}$, therefore equations (54) to (57) hold, and $rank(\mathbf{G}) = rank(\hat{\mathbf{G}}) = rank(\mathbf{H})$ [92]. Although $\hat{\mathbf{G}}$ describes the same eigenvalue distribution as $\mathbf{G}$, their associated Gershgorin radii differ. Therefore, the cost function developed in the following section considers both normalized matrices $\mathbf{G}$ and $\hat{\mathbf{G}}$.

4.4. Proposed Cost Function for Gershgorin Radii Reduction

Based on the general linear problem $\mathbf{p} = \mathbf{H}\mathbf{f}$, the system matrix for the CBCT case from (51) is defined as $\mathbf{H} = \mathbf{DTW}$. Thus, the Gram matrices $\mathbf{G}$ and $\hat{\mathbf{G}}$ are given by $\mathbf{G} = \mathbf{W}^\intercal\mathbf{T}^\intercal\mathbf{D}^\intercal\mathbf{DTW}$ and $\hat{\mathbf{G}} = \mathbf{DTWW}^\intercal\mathbf{T}^\intercal\mathbf{D}^\intercal$. Note that improving the condition of $\mathbf{G}$ and $\hat{\mathbf{G}}$ requires minimizing their off-diagonal entries [34]. To this end, products between $\mathbf{D}$ and $\mathbf{D}^T$, and $\mathbf{W}$ and $\mathbf{W}^T$ should be identity matrices; such condition however, is unrealistic in practical applications [46]. Therefore, instead of analyzing $\mathbf{H} = \mathbf{DTW}$, this work addresses the optimization problem from two fronts, based on (51). The first one considers the system $\mathbf{p} = \mathbf{D}\mathbf{H}_1\mathbf{f}$, with $\mathbf{H}_1 = \mathbf{TW}$, corresponding to the high-resolution propagation analysis, and assumes that a better usage of the high-resolution information implies an improvement of the total system. The second front considers the system $\mathbf{p} = \mathbf{H}_2\mathbf{W}\mathbf{f}$ with $\mathbf{H}_2 = \mathbf{DT}$, that accounts for the equivalent low resolution CA related to the projections $\mathbf{p}$. In this way, we assume that an appropriate matrix $\mathbf{T}$ jointly improves $\mathbf{H}_1$ and $\mathbf{H}_2$, and impacts the total matrix system $\mathbf{H}$. Taking $\mathbf{H}_1 \in \mathbb{R}^{\tilde{M}\times N}$ into account, the corresponding Gram matrices are given by $\mathbf{G}_1 = \mathbf{H}_1^\intercal\mathbf{H}_1 \in \mathbb{R}^{N\times N}$ and $\hat{\mathbf{G}}_1 = \mathbf{H}_1\mathbf{H}_1^\intercal \in \mathbb{R}^{\tilde{M}\times\tilde{M}}$. According to the Gershgorin theorem, radii are calculated as the row-wise sum of the off-diagonal entries of the Gram matrices. Let us first analyze $\mathbf{G}_1$, whose Gershgorin radii are represented by the vector $\mathbf{g}_1$, calculated as

$$\mathbf{g}_1 = \mathbf{G}_1\bar{\mathbf{1}} - \mathbf{q}, \tag{58}$$

where $\bar{\mathbf{1}}$ is an N-long one-valued vector used to calculate the row-wise sums in $\mathbf{G}_1$ as $[\mathbf{G}_1\bar{\mathbf{1}}]_i = \sum_j |[\mathbf{G}_1]_{ij}|$. The vector $\mathbf{q} \in \mathbb{R}^N$ accounts for the diagonal entries of $\mathbf{G}_1$, $[\mathbf{q}]_b = \sum_{a=1}^{\tilde{M}} [\mathbf{H}_1]^2_{a,b}$, and it is computed as follows

$$\mathbf{q} = (\mathbf{H}_1 \circ \mathbf{H}_1)^\intercal\,\hat{\mathbf{1}}, \tag{59}$$

with $\circ$ representing the Hadamard product and $\hat{\mathbf{1}}$ an $\tilde{M}$-long one-valued vector. Replacing $\mathbf{H}_1 = \mathbf{TW}$ and $\mathbf{q}$ from (59) in (58) yields

$$\begin{aligned} \mathbf{g}_1 &= \mathbf{W}^{\intercal}\mathbf{T}^{\intercal}\mathbf{T}\mathbf{W}\bar{\mathbf{1}} - \left(\mathbf{W}^{\intercal}\mathbf{T}^{\intercal} \circ \mathbf{W}^{\intercal}\mathbf{T}^{\intercal}\right)\hat{\mathbf{1}} \\ &= \mathbf{W}^{\intercal}\mathbf{T}\mathbf{W}\bar{\mathbf{1}} - \left(\mathbf{W}^{\intercal} \circ \mathbf{W}^{\intercal}\right)\mathbf{T}\hat{\mathbf{1}}, \end{aligned} \tag{60}$$

where the first term can be rewritten as $\mathbf{W}^{\intercal}\mathbf{T}\mathbf{W}\bar{\mathbf{1}}$ due to the fact that products $\mathbf{T}^{\intercal}\mathbf{T}$ and $\mathbf{T}\mathbf{T}^{\intercal}$ in (60) are products of a binary diagonal matrix. This property can be extended to the second term, where a single matrix $\mathbf{T}$ is enough to calculate $\left(\mathbf{W}^{\intercal}\mathbf{T}^{\intercal} \circ \mathbf{W}^{\intercal}\mathbf{T}^{\intercal}\right)\hat{\mathbf{1}} = \left(\mathbf{W}^{\intercal} \circ \mathbf{W}^{\intercal}\right)\mathbf{T}\hat{\mathbf{1}}$ that extracts the diagonal terms of $\mathbf{H}_1$. Moreover, the resulting product $\mathbf{T}\mathbf{W}\bar{\mathbf{1}}$ sets to zero some elements of the vector $\mathbf{W}\bar{\mathbf{1}}$ according to the diagonal entries of $\mathbf{T}$. This operation can be alternatively represented as $\mathbf{Q}\mathbf{T}\hat{\mathbf{1}}$, where $\mathbf{Q} = diag\{\mathbf{W}\bar{\mathbf{1}}\}$, which multiplied by the diagonal matrix $\mathbf{T}$ results in a diagonal matrix, and the product with the one-valued vector $\hat{\mathbf{1}}$ provides the row wise sum of the elements in $\mathbf{Q}$. Thus, (60) can be rewritten as

$$\mathbf{g}_1 = \mathbf{W}^{\intercal}\mathbf{Q}\mathbf{T}\hat{\mathbf{1}} - \left(\mathbf{W}^{\intercal} \circ \mathbf{W}^{\intercal}\right)\mathbf{T}\hat{\mathbf{1}}. \tag{61}$$

The product $\mathbf{T}\hat{\mathbf{1}}$ in (61) extracts the diagonal entries of $\mathbf{T}$ resulting in a vector with the coded aperture, $\mathbf{t}$. This variable $\mathbf{t}$ allows us to focus on the design of the CA entries, disregarding the off-diagonal entries of the matrix $\mathbf{T}$. Then, (61) can be rewritten as

$$\mathbf{g}_1 = \mathbf{W}^{\intercal}\mathbf{Q}\mathbf{t} - \left(\mathbf{W}^{\intercal} \circ \mathbf{W}^{\intercal}\right)\mathbf{t}. \tag{62}$$

Up to this point, the normalization of the sensing matrix $\mathbf{H}_1$ has not been considered. It is worth noting that this normalization aims at setting the diagonal entries of $\mathbf{G}_1$ to a constant value. The normalization of the columns of $\mathbf{H}_1$ has effect in the second term of (62), which becomes a one-valued vector. This effect can be obtained multiplying

(62) with $\mathbf{M}_1 = [\text{diag}\,((\mathbf{W}^\intercal \circ \mathbf{W}^\intercal)\,\mathbf{t})]^{-1}$, which yields to the redefinition of $\mathbf{g}_1$ as

$$\mathbf{g}_1 = \mathbf{M}_1\left(\mathbf{W}^\intercal\mathbf{Q} - (\mathbf{W}^\intercal \circ \mathbf{W}^\intercal)\right)\mathbf{t}. \tag{63}$$

The radii distribution of $\mathbf{G}_1$ can be succinctly expressed as

$$\mathbf{g}_1 = \mathbf{R}\mathbf{t}, \tag{64}$$

where $\mathbf{R} = \mathbf{M}_1(\mathbf{W}^\intercal\mathbf{Q} - (\mathbf{W}^\intercal \circ \mathbf{W}^\intercal))$. Similar to (58), the Gershgorin radii of the matrix $\hat{\mathbf{G}}_1$ are given by

$$\hat{\mathbf{g}}_1 = (\hat{\mathbf{G}}_1\hat{\mathbf{1}} - \hat{\mathbf{q}}), \tag{65}$$

where $\hat{\mathbf{q}} = (\mathbf{H}_1 \circ \mathbf{H}_1)\,\bar{\mathbf{1}}$. Replacing $\mathbf{H}_1 = \mathbf{T}\mathbf{W}$ in (65) yields

$$\hat{\mathbf{g}}_1 = \mathbf{T}\mathbf{W}\mathbf{W}^\intercal\mathbf{T}^\intercal\hat{\mathbf{1}} - (\mathbf{T}\mathbf{W} \circ \mathbf{T}\mathbf{W})\,\bar{\mathbf{1}}. \tag{66}$$

Due to the Hadamard matrix product properties, the second term $(\mathbf{T}\mathbf{W} \circ \mathbf{T}\mathbf{W})\,\bar{\mathbf{1}}$ in (66) can be expressed as $\mathbf{T}\,(\mathbf{W} \circ \mathbf{W})\,\bar{\mathbf{1}}$. Thus, (66) can be rewritten as

$$\hat{\mathbf{g}}_1 = \mathbf{T}\left(\mathbf{W}\mathbf{W}^\intercal\mathbf{T}^\intercal\hat{\mathbf{1}} - (\mathbf{W} \circ \mathbf{W})\,\bar{\mathbf{1}}\right). \tag{67}$$

In an analog manner to (61), note that the first term of (67) $\mathbf{T}^\intercal\hat{\mathbf{1}} = \mathbf{t}$. Also, the second term $(\mathbf{W} \circ \mathbf{W})\,\bar{\mathbf{1}}$, is equivalent to the product $\hat{\mathbf{Q}}\hat{\mathbf{1}}$ with $\hat{\mathbf{Q}} = diag\{(\mathbf{W} \circ \mathbf{W})\,\bar{\mathbf{1}}\}$. These considerations allow rewriting (67) as

$$\hat{\mathbf{g}}_1 = \mathbf{T}\left(\mathbf{W}\mathbf{W}^\intercal\mathbf{t} - \hat{\mathbf{Q}}\hat{\mathbf{1}}\right). \tag{68}$$

To account for the normalization of $\mathbf{H}_1$, let $\hat{\mathbf{M}}_1 = \hat{\mathbf{Q}}^{-1}$ be a matrix, that multiplied by (68) results in unitary diagonal entries of $\hat{\mathbf{G}}_1$. Thus, the radii in (68) are now given by

$$\hat{\mathbf{g}}_1 = \hat{\mathbf{M}}_1\mathbf{T}\left(\mathbf{W}\mathbf{W}^\intercal\mathbf{t} - \hat{\mathbf{Q}}\hat{\mathbf{1}}\right). \tag{69}$$

Further, since $\mathbf{T}$ and $\hat{\mathbf{M}}_1$ are diagonal matrices, $\mathbf{T}\hat{\mathbf{M}}_1 = \hat{\mathbf{M}}_1\mathbf{T}$ and (69) can be alternatively written as

$$\hat{\mathbf{g}}_1 = \mathbf{T}\left(\hat{\mathbf{M}}_1\mathbf{W}\mathbf{W}^{\intercal}\mathbf{t} - \hat{\mathbf{1}}\right). \tag{70}$$

Indeed, (70) can be succinctly expressed as the linear problem

$$\hat{\mathbf{g}}_1 = \mathbf{T}\left(\hat{\mathbf{R}}\mathbf{t} - \hat{\mathbf{1}}\right), \tag{71}$$

where $\hat{\mathbf{R}} = \left(\hat{\mathbf{M}}_1\mathbf{W}\mathbf{W}^{\intercal}\right)$. Note that, the trivial solution for the radii reduction of (71) consists in having zero Gershgorin radii by setting $\mathbf{T} = \mathbf{0}$, which would eliminate the codification. Alternatively, reduced non-zero radii can be obtained by minimizing $\hat{\mathbf{R}}\mathbf{t} - \hat{\mathbf{1}}$ with a CA with low transmittance k. In this context, a CA with transmittance k that reduces the Gershgorin radii of the high resolution system $\mathbf{H}_1 = \mathbf{T}\mathbf{W}$ should simultaneously take into account (64) and (71). Mathematically, such CA can be obtained by solving the following cost function

$$\mathbf{U}(\mathbf{t}) = \frac{\rho_1}{2} \parallel \mathbf{R}\mathbf{t} \parallel_2^2 + \frac{\rho_2}{2} \parallel \hat{\mathbf{1}} - \hat{\mathbf{R}}\mathbf{t} \parallel_2^2, \tag{72}$$

where $\boldsymbol{\rho}_1$ and $\boldsymbol{\rho}_2$ are constants.

To ensure that the effect of the CA in the decimation process is taken into account, let us now consider $\mathbf{H}_2 = \mathbf{D}\mathbf{T}$, which describes the codification process as if an equivalent low-resolution CA was used. The corresponding Gram matrices in this case are given by $\mathbf{G}_2 = \mathbf{H}_2^{\intercal}\mathbf{H}_2 \in \mathbb{R}^{\tilde{M}\times\tilde{M}}$ and $\hat{\mathbf{G}}_2 = \mathbf{H}_2\mathbf{H}_2^{\intercal} \in \mathbb{R}^{M\times M}$. Following the same analysis performed over $\mathbf{G}_1$, the Gershgorin radii vector of $\mathbf{G}_2$ is determined as in (58), yielding

$$\begin{aligned}
\mathbf{g}_2 &= \mathbf{G}_2\hat{\mathbf{1}} - (\mathbf{H}_2 \circ \mathbf{H}_2)^{\intercal}\,\mathbf{1} \\
&= \mathbf{T}^{\intercal}\mathbf{D}^{\intercal}\mathbf{D}\mathbf{T}\hat{\mathbf{1}} - (\mathbf{T}\mathbf{D} \circ \mathbf{T}\mathbf{D})^{\intercal}\,\mathbf{1} \\
&= \mathbf{T}^{\intercal}\mathbf{D}^{\intercal}\mathbf{D}\mathbf{t} - \mathbf{T}^{\intercal}\,(\mathbf{D} \circ \mathbf{D})^{\intercal}\,\mathbf{1},
\end{aligned} \tag{73}$$

where $\mathbf{1}$ is an M-long one-valued vector. Taking into account the structure of $\mathbf{D}$ from (52), in which there is only one one-valued entry per column, $\mathbf{D} \circ \mathbf{D} = \mathbf{D}$. Thus, (73) can be rewritten as

$$\begin{aligned} \mathbf{g}_2 &= \mathbf{T}^{\intercal}\left(\mathbf{D}^{\intercal}\mathbf{D}\mathbf{t} - \mathbf{D}^{\intercal}\mathbf{1}\right) \\ &= \mathbf{T}^{\intercal}\mathbf{D}^{\intercal}\left(\mathbf{D}\mathbf{t} - \mathbf{1}\right). \end{aligned} \tag{74}$$

In this case, following the same normalization procedure for $\mathbf{H}_2$ as for $\mathbf{H}_1$, which would consist in multiplying (74) by a matrix $\mathbf{M}_2$, will not affect the minimization of the Gershgorin radii since it can be attained by designing $\mathbf{t}$ such that $\mathbf{D}\mathbf{t} - \mathbf{1}$ is minimized.

On the other hand, consider the matrix $\hat{\mathbf{G}}_2$ whose radii vector is modeled by

$$\begin{aligned} \hat{\mathbf{g}}_2 &= \hat{\mathbf{G}}_2\mathbf{1} - \left(\mathbf{H}_2 \circ \mathbf{H}_2\right)\hat{\mathbf{1}} \\ &= \mathbf{D}\mathbf{T}\mathbf{T}^{\intercal}\mathbf{D}^{\intercal}\mathbf{1} - \left(\mathbf{D}\mathbf{T} \circ \mathbf{D}\mathbf{T}\right)\hat{\mathbf{1}} \\ &= \mathbf{D}\mathbf{T}\mathbf{D}^{\intercal}\mathbf{1} - \left(\mathbf{D} \circ \mathbf{D}\right)\mathbf{T}\hat{\mathbf{1}} \\ &= \mathbf{D}\mathbf{T}\hat{\mathbf{1}} - \mathbf{D}\mathbf{T}\hat{\mathbf{1}} \end{aligned} \tag{75}$$

$$\hat{\mathbf{g}}_2 = \mathbf{0}, \tag{76}$$

resulting in a zero-valued vector. Thus, the proposed cost function to evaluate the impact of the CA in the Gershgorin radii of $\mathbf{H}_2$ can be written as

$$\mathbf{V}(\mathbf{t}) = \frac{\rho_3}{2} \parallel \mathbf{1} - \mathbf{D}\mathbf{t} \parallel_2^2, \tag{77}$$

where ρ_3 is a regularization constant. Taking into account the results of (72) and (77), the coded aperture optimization is given by the minimization problem

$$\mathbf{t}^* = \underset{\mathbf{t}}{\operatorname{argmin}}\, \mathbf{U}(\mathbf{t}) + \mathbf{V}(\mathbf{t}), \tag{78}$$

which can be solved by getting the operator to find the appropriate patterns $\mathbf{t}$ that reduce the radii of (51) based on the high-resolution modulation and the low-resolution CA effect in the CBCT sensing process.

Despite (78) can be solved by a GD method, the solutions might not be binary. Therefore, to ensure a binary coded aperture with transmittance k, a hard thresholding function $\mathcal{H}_k\{\cdot\}$ is required at each iteration of the proposed method. Taking this into account, the gradient for the $z-$th iteration is obtained by deriving the cost function in (78) with respect to the desired variable $\mathbf{t}$, and applying the thresholding function, yielding

$$\begin{aligned}\mathbf{t}_z = \mathcal{H}_k\{&\mathbf{t}_{z-1} + \rho_1 \mathbf{R}^\intercal \left(\mathbf{R}\mathbf{t}_{z-1}\right)\\ &+ \rho_2 \hat{\mathbf{R}}^\intercal \left(\hat{\mathbf{1}} - \hat{\mathbf{R}}\mathbf{t}_{z-1}\right)\\ &+ \rho_3 \mathbf{D}^\intercal \left(\mathbf{1} - \mathbf{D}\mathbf{t}_{z-1}\right)\}.\end{aligned} \tag{79}$$

Alternatively, the solution can be boosted by replacing the transpose of the matrices $\mathbf{R}^\intercal$, $\hat{\mathbf{R}}^\intercal$, and $\mathbf{D}^\intercal$, by its (Moore-Penrouse) pseudoinverse approximation $\mathbf{R}^\dagger$, $\hat{\mathbf{R}}^\dagger$, and $\mathbf{D}^\dagger$ respectivelly. For it, is possible to use the SVD decomposition, and use the reciprocal of all the non-zero singular values to acquire the desired pseudoinverse. This conception allows formulate (79) as

$$\begin{aligned}\mathbf{t}_z = \mathcal{H}_k\{&\mathbf{t}_{z-1} + \rho_1 \mathbf{R}^\dagger \left(\mathbf{R}\mathbf{t}_{z-1}\right)\\ &+ \rho_2 \hat{\mathbf{R}}^\dagger \left(\hat{\mathbf{1}} - \hat{\mathbf{R}}\mathbf{t}_{z-1}\right)\\ &+ \rho_3 \mathbf{D}^\dagger \left(\mathbf{1} - \mathbf{D}\mathbf{t}_{z-1}\right)\}.\end{aligned} \tag{80}$$

Even for the case where the algorithm 1 provides a proper solution, notice that $\mathbf{R}$ depends on $\mathbf{t}$ and its pseudo-inverse must be estimated in each iteration, offering a computationally expensive for the coded aperture design.

Algorithm 1 Initial coded aperture design for super-resolved compressive CBCT

procedure CA-DESIGN($k, d_1, d_2, z_{\max}, \alpha, \rho_1, \rho_2, \rho_3, \mathbf{t}_0$)
  $z \leftarrow 1$
  Calculate $\hat{\mathbf{R}}^{\dagger}$,$\mathbf{D}^{\dagger}$ ▷ Calculate the pseudo-inverse
  while $z \neq z_{max}$ **do**
    Calculate $\mathbf{R}^{\dagger}$ ▷ Calculate the pseudo-inverse
    $\mathbf{t}_z \leftarrow \mathcal{H}_k\{\mathbf{t}_{z-1} + \rho_1\mathbf{R}^{\intercal}\left(\mathbf{R}\mathbf{t}_{z-1}\right) + \rho_2\hat{\mathbf{R}}^{\intercal}\left(\hat{\mathbf{1}} - \hat{\mathbf{R}}\mathbf{t}_{z-1}\right) + \rho_3\mathbf{D}^{\dagger}\left(\mathbf{1} - \mathbf{D}\mathbf{P}_z\mathbf{t}_{z-1}\right)\}$
    $z \leftarrow z + 1$
  $\mathbf{t}^* \leftarrow \mathbf{t}_{z_{max}}$
  return $\mathbf{t}^*$ ▷ Return final iteration $\mathbf{t}^*$

4.5. Iterative Design of the Super-Resolution CA

It is worth noting that the decimation matrix $\mathbf{D}$ in the last term of (79) induces an error replication among iterations of the gradient descent. More specifically, let $\mathbf{e}_{z-1} = \mathbf{1}-\mathbf{D}\mathbf{t}_{z-1}$ be the residual vector of the sub-problem in (77). The update of this term at iteration z is given by $\Delta\mathbf{t}_{z-1} = \mathbf{D}^T\mathbf{e}_{z-1}$, however, the structure of $\mathbf{D}^T$ replicates each value of $\mathbf{e}_{z-1}$ to d pixels of $\mathbf{\Delta t}_{z-1}$, as illustrated in Fig.11 (a), where black squares represent one-valued elements, white squares represent zero-valued entries, and colored squares represent different values, with blue being the largest and yellow the smallest. This replication causes that applying the threshold function to $\mathbf{\Delta t}_{z-1} + \mathbf{f}_{z-1}$ in the update step, as illustrated in Fig. 11(b), will result in just keeping the values coming from a few super-pixels, thus preventing uniform CA and promoting similar solutions in all iterations.

To avoid this issue, we introduce the matrix $\mathbf{P} \in \mathbb{R}^{\tilde{M}\times\tilde{M}}$, which multiplies the last term in (79) [94]. This product assigns different gradient weights to each individual pixel in the up-sampling operation, as illustrated in Fig. 11(c). The effect of introducing $\mathbf{P}$ is depicted in Fig. 11(d), where the one-valued elements of the CA are more uniformly located across the super-pixels. More precisely, $\mathbf{P}$ is a diagonal matrix defined for

[94] Zhaonan Qu, Yinyu Ye, and Zhengyuan Zhou. *Diagonal Preconditioning: Theory and Algorithms*. 2020. arXiv: `2003.07545 [cs.LG]`.

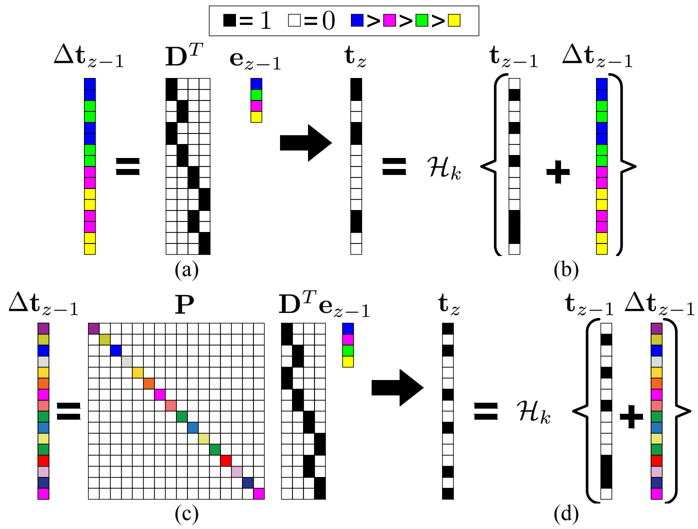

Figure 11. Error replication due to decimation matrix $\mathbf{D}$, for $k = 0.375$, and proposed spatial homogenization solution. Black squares indicate one-valued elements, white squares are zeros, and colored squares represent different values, with magenta being the largest and yellow the smallest. (a) CA variation at z-th iteration; (b) CA update; (c) Proposed spatial homogenization; (d) Effect of proposed approach.

each iteration z as

$$\mathbf{P}_z = \mathbf{I} - \alpha \mathbf{\Omega}_z, \tag{81}$$

where $\mathbf{I}$ is an identity matrix, $0 \leq \alpha \leq 1$ is a scalar value that controls the desired amount of variation added to the gradient and $\mathbf{\Omega}_z$ is a diagonal matrix with Gaussian random entries of mean 0.5. Extending the diagonal structure of a matrix to the gradient step ρ_3 it is possible to differentiate between similar options, the response of the iterative method improves [95]. This approach aims at promoting a uniform spatial distribution in $\mathbf{t}_z$ concerning to the super-resolution factor, such that all features of the equivalent low resolution coded aperture has approximately the same amount of one-valued in his modulation. Taking into account the introduction of $\mathbf{P}$, the problem

[95] Pablo Tarazaga and Diego Cuellar. “Preconditioners generated by minimizing norms”. In: *Computers & Mathematics with Applications* 57.8 (2009), pp. 1305–1312.

(78) can be reformulated as

$$\mathbf{t}^{*} = \underset{\mathbf{t}}{\operatorname{argmin}}\, \mathbf{U}(\mathbf{t}) + \mathbf{V}(\mathbf{P}\mathbf{t}), \tag{82}$$

and its update is given by a gradient of the form

$$\begin{aligned} \mathbf{t}_z = \mathcal{H}_k\{ & \mathbf{t}_{z-1} + \rho_1 \mathbf{R}^{\intercal} \left(\mathbf{R}\mathbf{t}_{z-1}\right) \\ & + \rho_2 \hat{\mathbf{R}}^{\intercal} \left(\hat{\mathbf{1}} - \hat{\mathbf{R}}\mathbf{t}_{z-1}\right) \\ & + \rho_3 \mathbf{P}_z^{\intercal} \mathbf{D}^{\intercal} \left(\mathbf{1} - \mathbf{D}\mathbf{P}_z \mathbf{t}_{z-1}\right)\}. \end{aligned} \tag{83}$$

From (39), k is redefined as the high-resolution transmittance, the proposed method to solve (82) is summarized in algorithm 2.

Algorithm 2 Coded aperture design for super-resolved compressive CBCT

procedure CA-DESIGN($k, d_1, d_2, z_{\max}, \alpha, \rho_1, \rho_2, \rho_3, \mathbf{t}_0$)
    $z \leftarrow 1$
    while $z \neq z_{max}$ **do**
        $\mathbf{P}_z \leftarrow \mathbf{I} - \alpha \mathbf{\Omega}_z$
        $\mathbf{t}_z \leftarrow \mathcal{H}_k\{\mathbf{t}_{z-1} + \rho_1 \mathbf{R}^{\intercal} \left(\mathbf{R}\mathbf{t}_{z-1}\right) + \rho_2 \hat{\mathbf{R}}^{\intercal} \left(\hat{\mathbf{1}} - \hat{\mathbf{R}}\mathbf{t}_{z-1}\right) + \rho_3 \mathbf{P}_z^{\intercal} \mathbf{D}^{\intercal} \left(\mathbf{1} - \mathbf{D}\mathbf{P}_z \mathbf{t}_{z-1}\right)\}$
        $z \leftarrow z + 1$
    $\mathbf{t}^{*} \leftarrow \mathbf{t}_{z_{max}}$
    return $\mathbf{t}^{*}$ ▷ Return final iteration $\mathbf{t}^{*}$

5. CBCT Experimental Procedure

Simulations with medical data sets were performed to test the proposed CA design in the recovery process, it shows that the proposed design attains high-resolution images from lower-resolution detectors in a single-shot CBCT scenario. This Chapter describes the configuration of the simulated CBCT architecture as well as the simulation parameters to generate compressive sparse view measurements and the input images. Afterwards, various experiments and their results are presented, including the evaluation of the Gershgorin radii reduction, image reconstruction quality for different super-resolution factors for noiseless and noisy measurements, as well as a computational complexity analysis of the proposed approach. Besides, reconstructions from Monte-Carlo simulated projections with the GATE/GEANT4 toolkit [96] are also included. Besides, image quality is improved in up to 5 dB of PSNR compared to random CA patterns for different super-resolution factors. Moreover, reconstructions from Monte-Carlo simulated projections show up to 3 dB improvements. Further, for the analyzed cases, the computational load of the proposed approach is up to three orders of magnitude lower than that of SVD-based methods.

5.1. Simulated Compressive CBCT Architecture and Parameter Setup

The compressive CBCT architecture was simulated with the ASTRA Toolbox [59], yielding the sensing matrix $\mathbf{W}$ to generate the projections $\mathbf{p}$ as in (51). The system was configured such that the object's axis of rotation is located at 290.2mm from the X-ray source, and the detector array is located 484.6mm from the object's axis of rotation. The object volume is assumed to fit a $128 \times 128 \times 12$ grid. Thus, the system configuration requires a 2D array of 512×48 detectors, each of size 0.4714×0.4714

[96] David Sarrut et al. "A review of the use and potential of the GATE Monte Carlo simulation code for radiation therapy and dosimetry applications". In: *Medical physics* 41.6Part1 (2014), p. 064301.

mm, if high resolution projections were to be acquired. However, since this work assumes that a low resolution detector array is available, the simulated sensor has $\frac{512}{d_1} \times \frac{48}{d_2}$ elements, where the decimation factors d_1 and d_2 vary as it will be later described. The matrix $\mathbf{W}$ accounts for a total of 97 projection angles over the full angular range $[0, 2\pi)$, each one with a different coded aperture pattern. Coded apertures were obtained using Algorithm 2 to construct the matrix $\mathbf{T}$, and it is assumed that each detector is affected by the projections related to $d_1 \times d_2$ coded aperture features, according to the decimation matrix from (52). The parameters for Algorithm 2 were fixed as $z_{max} = 500$ iterations; constant $\alpha = 0.95$; the initial solution $\mathbf{t}_0$ is a binary random vector; the constants ρ_1,ρ_2 and ρ_3 were adjusted by cross validation until the best possible homogenization was obtained; the transmittance of the coded apertures was varied to analyze its effects in the reconstructions. High resolution volume reconstructions were obtained from the low-resolution projections by solving (53) with the C-SALSA algorithm [84], for which the regularization parameter τ was selected by cross-validation, and the regularization operator Φ was set to be the ℓ_1 norm.

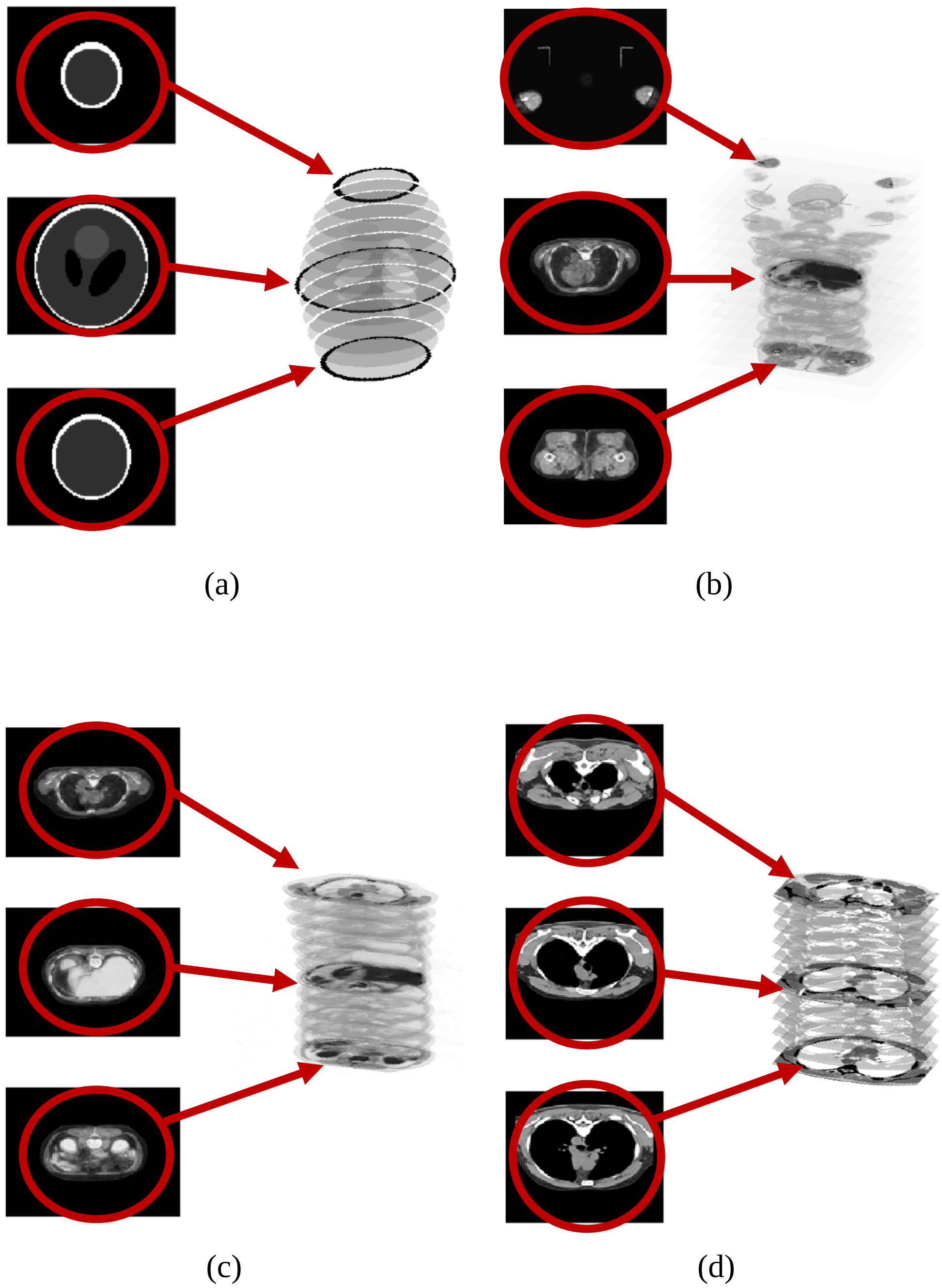

Figure 12. Datasets used for simulations, each with 12 slices of 128×128 pixels. (a) Synthethic 3D-Shepp-Logan phantom; real medical datasets (b) Multiple (Head to hips), (c) Abdomen, and (d) Thorax.

Four object volumes $\mathbf{F}$ were used for simulations, whose dimensions match the system configuration previously described, i.e., 12 slices of 128×128 pixels. The first one is a synthetic data set known as the 3D-Shepp-Logan phantom, shown in Fig. 12(a).The remaining three data sets are real medical images from [35], acquired by CATME SAS[97]. The second test image referred to as Multiple, illustrated in Fig. 12(b), provides 12 slices from the head to the hips. The third image called Abdomen, shown in Fig. 12(c), contains 12 slices of an abdomen, and the fourth image corresponds to the thorax area, as depicted in Fig. 12(d).

5.2. Gershgorin Radii Reduction

This experiment evaluates the actual Gershgorin radii reduction for the system matrix $\mathbf{H} = \mathbf{DTW}$ with $\mathbf{T}$ obtained using the proposed CA design, and compares them with the radii of the system matrix with a random CA $\mathbf{T}$, following a Bernoulli distribution with parameter k. The concentration of the eigenvalues was calculated as the difference between the bounds from (57), and Fig. 13 illustrates the average bound differences as a function of the transmittance, for 5 matrix realizations using $d = 4 \times 4$ and $d = 2 \times 2$ for both types of coded apertures. Notice that the eigenvalue bounds of the matrices with the proposed CA design attain lower eigenvalue bound differences. Moreover, for low transmittances (k) and $d = 4 = (2 \times 2)$, both curves exhibit similar behavior. This effect is explained by the fact that a low decimation factor tends to induce a similar number of zeros between the high-resolution propagations and the detector. It is taking into account that a very low transmittance value has a high number of propagation functions modulated by zero weights producing a weighted matrix with very few rows. In this context, two systems with a different modulation but the same low transmittance value, reveal a condition number that similarly describes the system in terms of eigenvalues. Consequently, very low transmittance yields more

[97] Images correspond to anonymous patients. Patient-related data were not provided. Authors were not involved in the acquisition process of these data sets.

zero-valued features in the low-resolution detector when the decimation factor tends to $d = 1$, which affects the quality of the system and the sensed data.

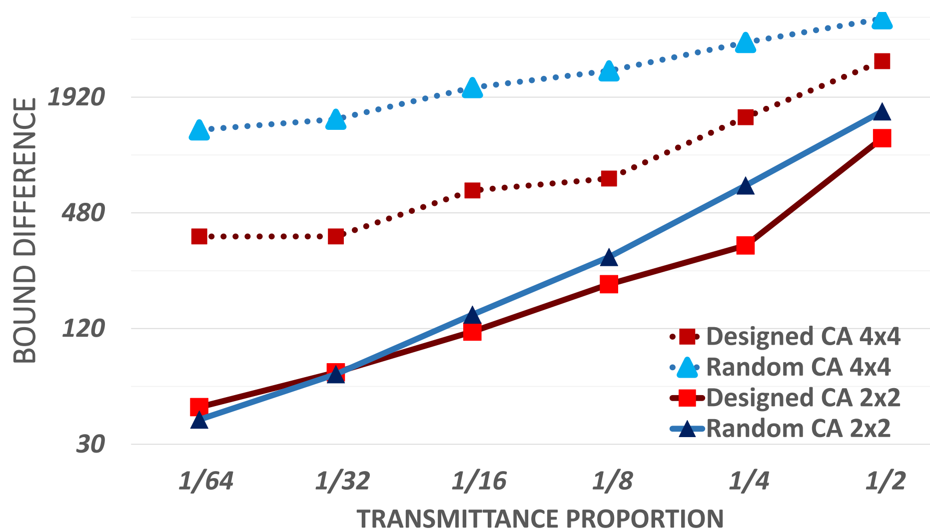

Figure 13. Average eigenvalue bound difference from the Gershgorin radii reduction in (57), as a function of the transmittance k for the designed CA and random CA using a decimation factor of $d = 4 \times 4 = 16$ and $d = 2 \times 2 = 16$.

Figure 14 compares portions of random and designed CA patterns, for three different angle views, using decimation factors $d = 4, 16$, whose transmittance values are $1/d$. The super-pixel grid for each case is illustrated in white. Observe that for both decimation factors, the designed CA contains a single passing (one-valued) element on each super-pixel, in contrast to the random CA that exhibit more than one passing feature at some super-pixels, and in other cases they completely block all the information from one super-pixel. To illustrate how multiple elements of the CA affect a detection into the low-resolution detector, it is possible to apply the decimation to a CA distribution. Thereby, the outcome vector indicates the number of passing elements for a decimation factor. For this sense, the histogram of the decimated CA distribution indicates how well allocated is the CA in function to the decimation process. Figure 15 illustrates the mean of the histogram for five decimated distributions, with a decimation factor $d = 16$, handling a transmittance value equal to Fig. 15 (a) 0.015625, (b) 0.03125, (c) 0.0625, (d) 0.125, (e) 0.25 and (f) 0.5, and highlighying the Fig. 15(c), where the transmittance is equal to $\frac{1}{d}$.

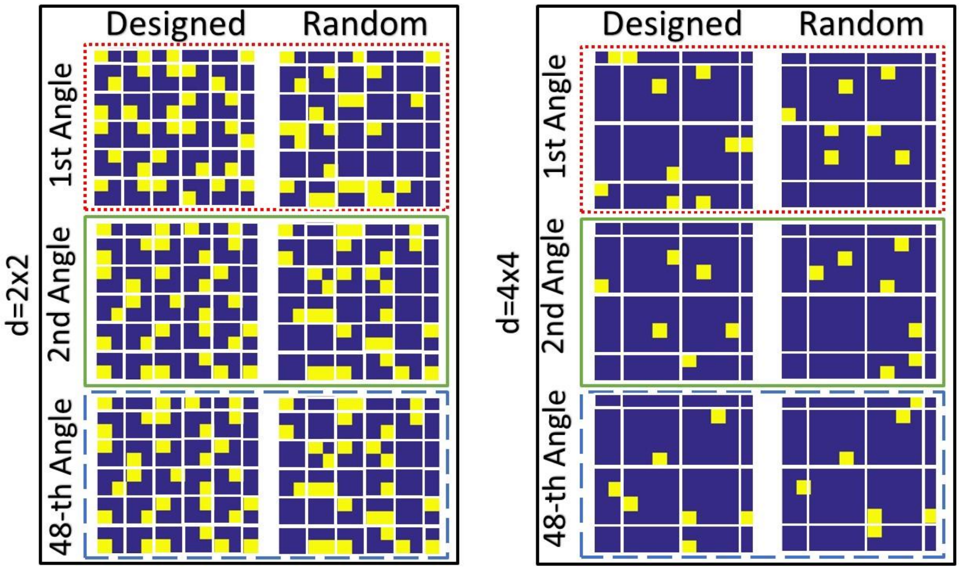

Figure 14. Realizations of designed CA with decimation factors $d = 4, 16$ for three different angle views, compared with non-designed CA patterns.

5.3. Computational Complexity

This section describes the computational complexity of algorithm 2. Specifically, the cost of the gradient step in (83) is compared with respect to actually computing the SVD of the sensing matrix at each iteration, i.e. algorithm 1. Considering the dimensions of the matrices and vectors involved in the products calculated in (83), each iteration of the proposed algorithm 2 exhibits a computational complexity $O(\tilde{M}^2)$ when $\tilde{M} > N$, and $O(\tilde{M}N)$ when $\tilde{M} < N$. In contrast, with the algorithm 1 where the computational complexity of SVD is $O(M^2N + N^2M + N^3)$ [98]. Moreover, the running time of algorithm 2 was evaluated to verify the theoretical computational complexity analysis. To this end, each spatial dimension of the data cube was varied from 1

[98] Ievgen Redko and Younès Bennani. “Non-negative Matrix Factorization with Schatten p-norms Reguralization”. In: *International Conference on Neural Information Processing*. Springer. 2014, pp. 52–59.

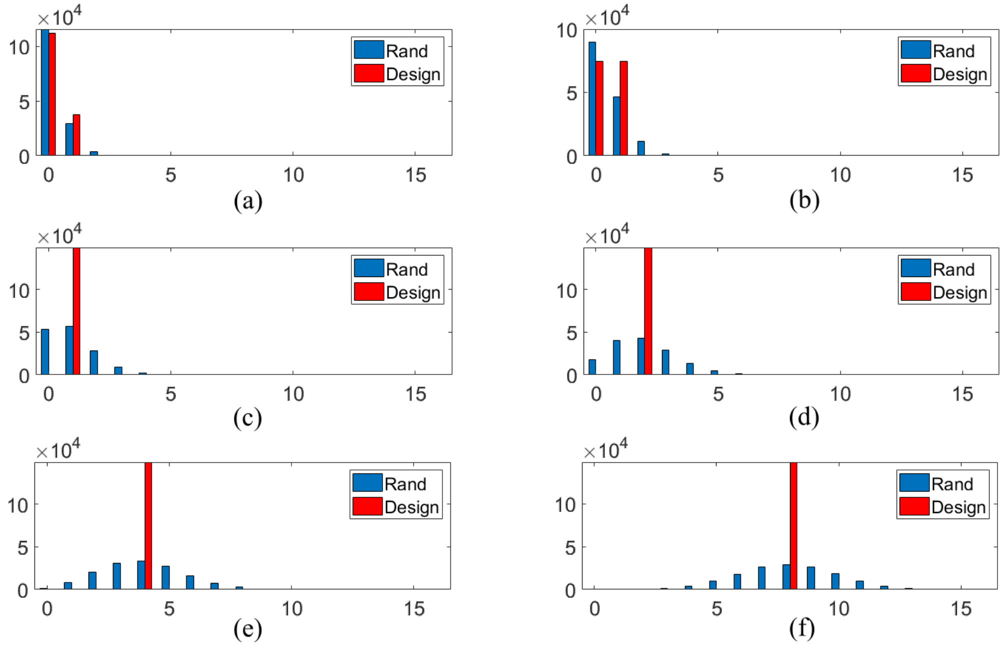

Figure 15. Histogram comparisson between random (blue) and designed (red) distributions of a decimated CA, with a decimation factor of $d = 16$, for a transmittance equal to (a) 0.015625, (b) 0.03125, (c) 0.0625, (d) 0.125, (e) 0.25 and (f) 0.5.

to 64, while the number of slices was fixed at 12. For comparison purposes, the same data cubes were used to measure the running time of the SVD method. All simulations were conducted and timed on an Intel Core i7 3.6GHz CPU with 32 GB RAM.

Figure 16 presents the average running time per iteration of 5 run trials, measured in seconds, for both methods. Note that these results are consistent with the theoretical complexity analysis, in which performing SVD is significantly more expensive than estimating the eigenvalue bounds based on the Gershgorin radii reduction through the proposed gradient method. Further, SVD computation is prohibited in the system employed for simulations. Therefore, in Fig. 16, the SVD results for more than 196,608 voxels, i.e. a $64 \times 64 \times 12$ data cube, correspond to the projected behavior. Contrarily, the proposed method is still able to evaluate such matrix dimensions. To compare the success of a CA distribution achieved with the algorithm 2, consider

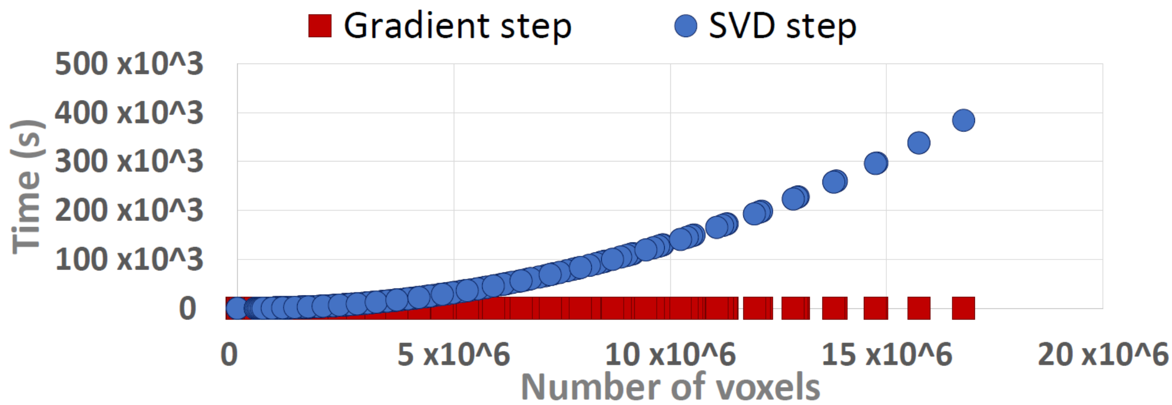

Figure 16. Average running time per iteration step for the proposed gradient method and a SVD design, varying the data cube spatial dimensions.

the response of the algorithm 1 as a solution of reference. In this context, Fig. 17 show the condition number to assess the proposed SR-CBCT system through three different scenarios, an initial random distribution of the CA elements (green bars), using the algorithm 1 as a solution subject to an SVD process (red bars), and using the proposed algorithm 2 (blue bars), using 27648, 836352 and 12192768 voxels in each test.

As a consequence, a comparable result in Fig. 17 between algorithm 1 and the algorithm 2 validates the use of the proposed algorithm 2, taking into account a lower computational cost as reveal the Fig. 16.

5.3.1. Reconstruction Quality These experiments compare the reconstruction quality of the proposed coded aperture design with respect to non-designed coded apertures as a function of the transmittance k and super-resolution factor d. Two different scenarios were analyzed, the first one considers $d_1 = d_2 = 2$ for a total super-resolution factor of $d = 4$, and the second analyzes the case in which $d_1 = d_2 = 4$, for a total factor of $d = 16$. The average peak signal-to-noise ratio (PSNR) is used to evaluate the quality of the reconstructed images in decibels (dB). Figure 18 presents the average PSNR for all the test images, where each result is the average of 5 run trials for each case. In general, these results show that the proposed

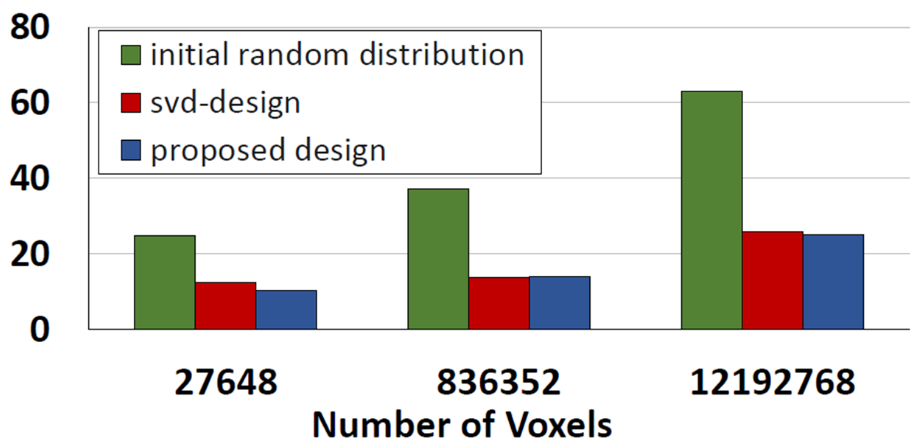

Figure 17. Average condition number for the initial distribution, the proposed SVD method and the proposed gradient method, varying the data cube spatial dimensions.

coded aperture design improves the results of the non-designed patterns, for each particular case.

Moreover, largest transmittance values result in loss of image quality. This behavior has more impact on results from larger super-resolution factors, i.e. $d = 16$. Further, note that the best PSNR on each case occurs when the transmittance is set to $1/d$. This occurs as larger transmittance values imply more multiplexed values on each detector, which results in a more complex inverse super-resolution problem. For comparison purposes, Fig. 18 also includes the results obtained from a high-resolution detector, and it can be seen that for lower transmittance values, the reconstruction behavior from the designed CA resembles that of the high-resolution reconstructions. Further, for larger transmittance values, the designed CA with $d = 2 \times 2$ still provides comparable results.

Figure 19 illustrates the absolute error between the ground truth and attained reconstructions of two different slices using $d = 4 \times 4 = 16$ for all test images. Specifically, Fig.19(a) shows the 5-th and 8-th slices of the 3D-Shepp-Logan Phantom; Figs.19(b), 19(c) and 19(d) depict the errors of the 4-th and 10-th slices of Multiple,

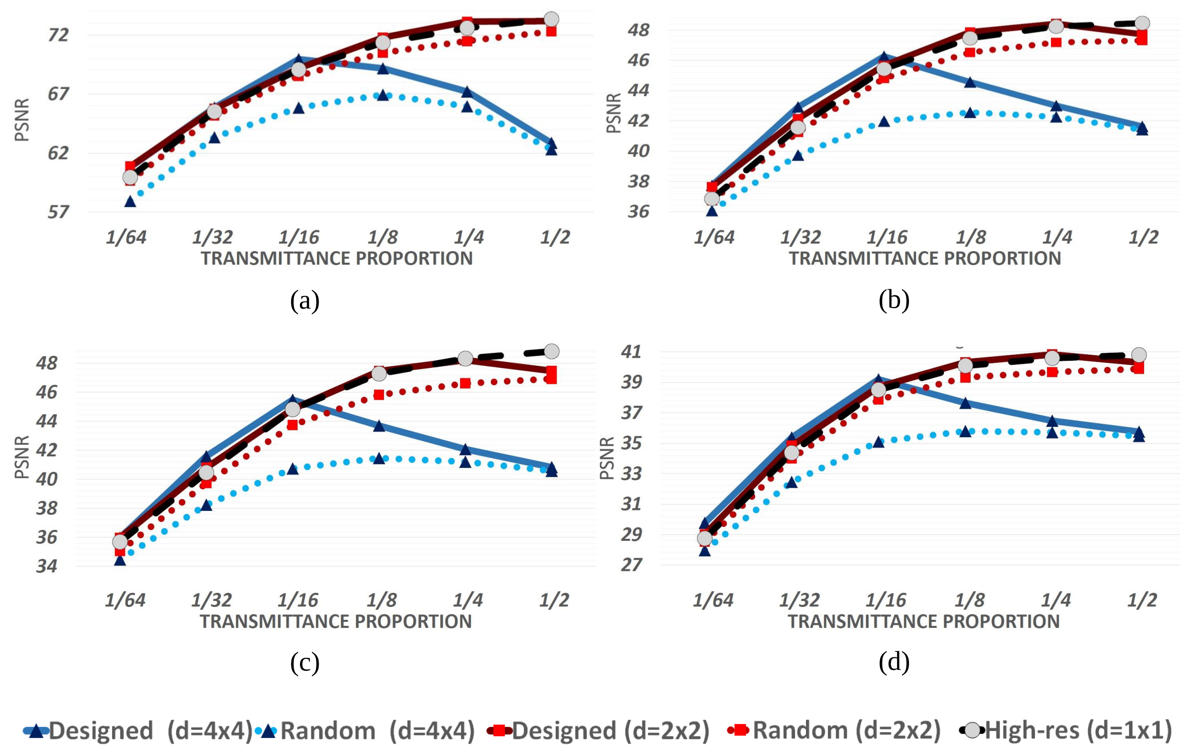

Figure 18. Average reconstruction PSNR as a function of the transmittance k, with decimation factors $d_1 = d_2 = 2$ and $d_1 = d_2 = 4$, using the proposed coded aperture design and random patterns, for the test images (a) 3D-Shepp-Logan phantom, (b) Multiple, (c) Abdomen, and (d) Thorax.

Abdomen and Thorax, respectively. Top row of each image corresponds to the errors of the reconstructions from random coded apertures, and bottom images are the errors of the reconstructions from the design patterns. It is important to highlight that the proposed design results in lower reconstruction errors for all cases.

Besides comparison with typical random CA patterns, we performed an additional simulation to compare the proposed approach with respect to a general non-designed random-SR pattern, comprising a single-randomly selected passing element for each super-pixel, which corresponds to just solving (77). Note that this pattern does not allow to control a desired transmittance proportion. Moreover, it does not consider pixel correlations described by the sensing matrix. Further, the probability of choos-

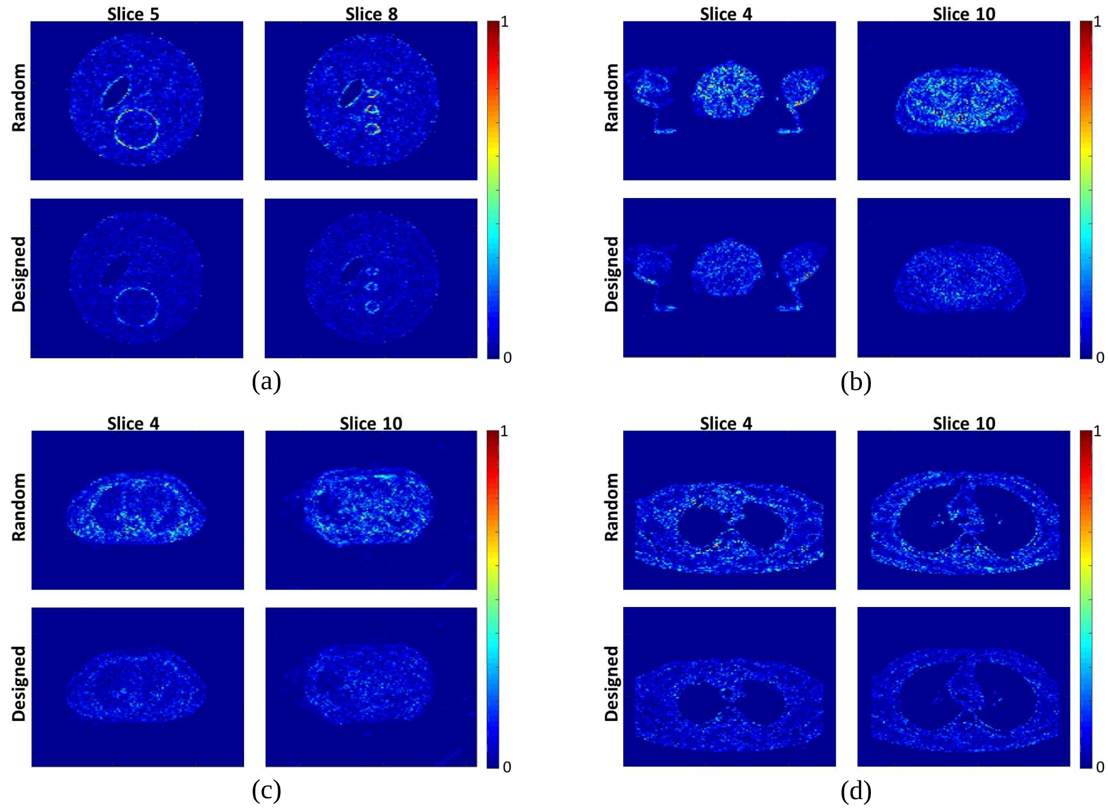

(a) (b) (c) (d)

Figure 19. Normalized absolute reconstruction error comparison with respect to ground truth images for two different slices (columns), using random (Top rows) and designed coded apertures (Bottom rows) for (a) 3D-Shepp-Logan phantom, (b) Multiple, (c) Abdomen, and (d) Thorax data sets in a system with $d = 16$.

ing the best passing-location per super-pixel decreases with the decimation factor. Figure 20 presents a comparison of the reconstruction normalized absolute error of a slice, using the designed CA and the random-SR pattern, for $d = 4, 16$. The transmittance of the designed CA in these cases was set to $\frac{1}{d}$ to ensure a fair comparison. It can be seen that these results are consistent with those from the previous experiments, with larger errors in the random-SR, and a gain of 2 dB of PSNR of the designed pattern for $d = 4 \times 4 = 16$. In contrast, the results for $d = 2 \times 2 = 4$ are comparable for both approaches.

The performance of the proposed CA design was also tested for a data set with a large number of slices. In particular, a $128 \times 128 \times 64$ version of the Multiple image was

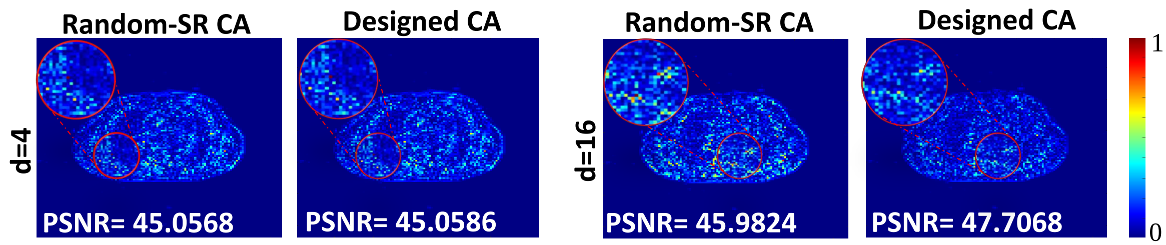

(a) (b) (c) (d)

Figure 20. Normalized absolute reconstruction error comparison of a recovered slice for $d = 4$ and $d = 16$, with a transmittance equal to $\frac{1}{4}$ and $\frac{1}{16}$ respectivelly, using random-SR (a,c) and designed CA patterns (b,d).

used. This experiment was conducted in a workstation with 28 2.6 GHz processors, and 196 GB RAM. To preserve the detector size, and the number of angles used in the previous experiments, the detector array in this case comprises $\frac{512}{d_1} \times \frac{240}{d_1}$ pixels, instead of $\frac{512}{d_1} \times \frac{48}{d_1}$. Thus, this system keeps the sampling ratio between the measurements and the unknowns. Obtained results for $d = 4$ exhibit 31.46 dB of average PSNR for the non-designed PSNR and 35.63 dB for the designed CA, respectively. Similarly, for $d = 16$, non-designed CA attained 31.65 dB and 35.37 dB, respectively. Figure 21 illustrates the reconstructions for two slices, with improvements of 3 dB of PSNR for a single slice.

5.4. Reconstructions from Noisy Measurements

This section evaluates the reconstruction performance of the proposed coded aperture design for super-resolution in noisy scenarios. To this end, Poisson noise was

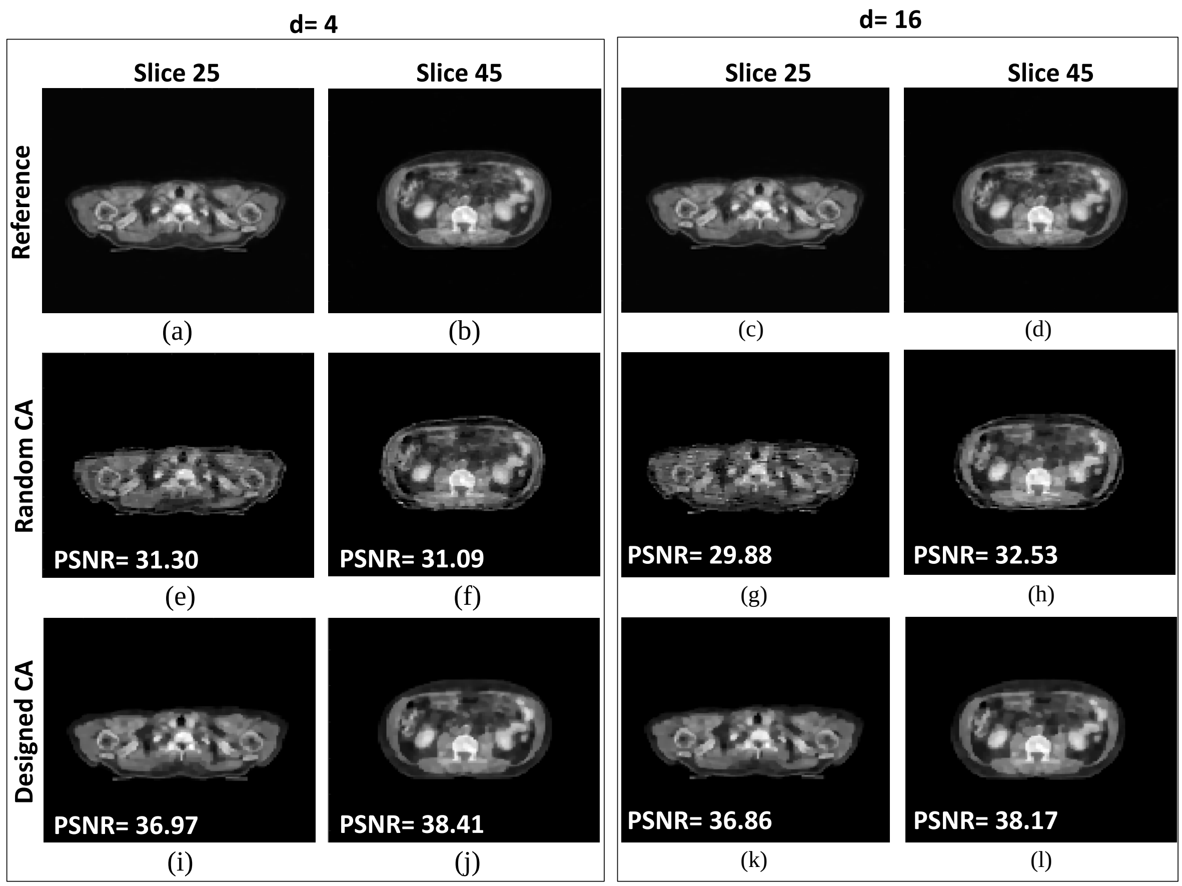

Figure 21. Comparison of high-resolution reconstructions of two slices with random CA and designed CA for the 128×128 data set Multiple with 64 slices, using $d = 4$ and $d = 16$.

added to the simulated projections [99][100][101][102] through the ASTRA Toolbox, employ-

---

[99] Valentina Davidoiu et al. "Evaluation of noise removal algorithms for imaging and reconstruction of vascular networks using micro-CT". in: *Biomedical Physics & Engineering Express* 2.4 (2016), p. 045015.

[100] Manoj Diwakar and Manoj Kumar. "A review on CT image noise and its denoising". In: *Biomedical Signal Processing and Control* 42 (2018), pp. 73–88.

[101] Alessandro Perelli et al. "Compressive Computed Tomography Reconstruction through Denoising Approximate Message Passing". In: *SIAM Journal on Imaging Sciences* 13.4 (2020), pp. 1860–1897.

[102] Jing Huang et al. "Iterative image reconstruction for sparse-view CT using normal-dose image induced total variation prior". In: *PloS one* 8.11 (2013), pp. 1–15.

ing signal-to-noise ratio (SNR) values of $5, 10, 15, 20, 25$ and 30 dB. These simulations consider transmittance values $k = \{\frac{1}{4}, \frac{1}{16}\}$, which correspond to the best noiseless results from Fig. 18, for the decimation factors $d = 4, 16$, respectively. Figure 22 presents the average reconstruction quality of 5 run trials for each case, in terms of PSNR, as a function of the SNR, for all test images.

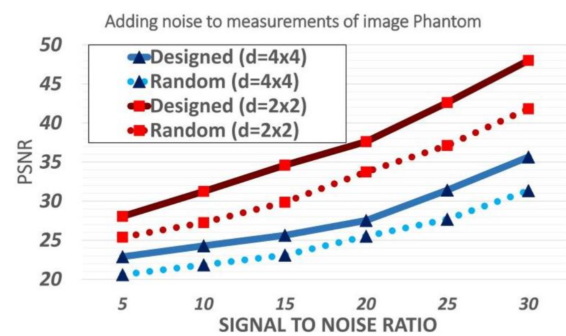

(a)

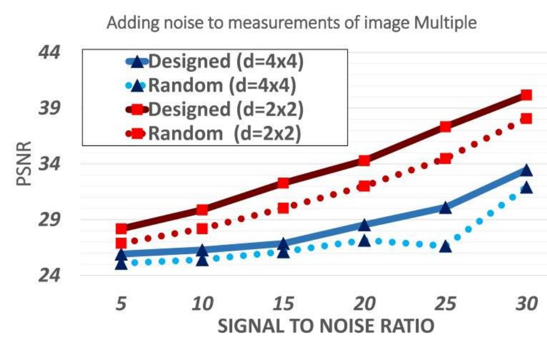

(b)

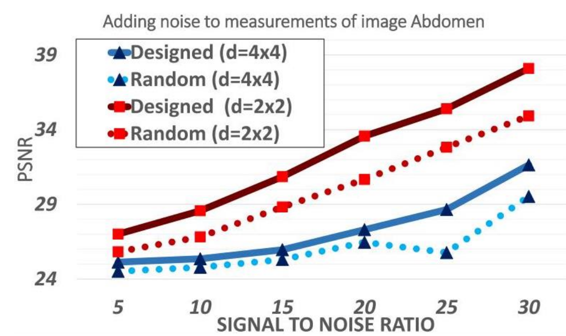

(c)

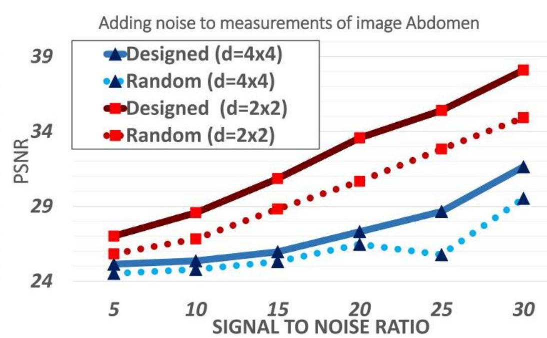

(d)

Figure 22. Average reconstruction PSNR from noisy (Poisson) measurements as a function of the SNR, using designed CA and random CA for the test data sets (a) 3D-Shepp-Logan phantom, (b) Multiple, (c) Abdomen and (d) Thorax.

These results show the robustness of the proposed coded apertures to noisy scenarios, since their performance consistently overcomes that of the random coded apertures, even in the noisiest cases. Further, it can be also noted that reconstructions of larger super-resolution factors ($d = 16$) are more affected by the noise, as each low resolution detector takes into account the associated noise from d high resolution projections. Moreover, Fig. 23 illustrates the comparisons of the obtained reconstructions from noisy projections with SNR $= 15$dB and $d = 16$ for all test images, using designed and random coded apertures. For reference, the low-resolution and high-resolution ground truth images for each case are also depicted. Specifically, the low-resolution ground truth represents the image that would be recovered if a system with a 1:1 ratio between a low-resolution coded aperture and a low-resolution detector. Similarly, the high resolution image represents the target image that would be recovered if a system with a 1:1 ratio between a high-resolution detector and a high-resolution coded aperture. Thus, the results from Fig. 23 show that, in general, the proposed coded aperture design allows to obtain super-resolved images under noisy scenarios. Further, note that in some cases, the reconstructions from the random coded apertures resemble the low resolution ground truth instead of the high resolution images.

5.5. Montecarlo Simulation

Geant4 can be described as a Monte Carlo simulation toolkit to represent the passage of particles through matter, and the GATE toolkit (based on GEANT4) provides additional high-level features to facilitate the design of GEANT4- based simulations. In contrast with the acquisition of measurements given by the sensing matrix $\mathbf{W}$ calculated with the ASTRA toolbox, GATE/GEANT4 toolkit simulate the measurement process performing single and multiple scattering models. The suggested process involves measurements of the compressive CBCT system simulated with the GATE/Geant4 toolkit [96], and its corresponding reconstruction is performed by employing the matrix calculated with the ASTRA toolbox in Matlab. Selecting a super-resolution factor $d = 2 \times 2$, the system deploys a detector array of 256×24 pixels of size 0.9048×0.9048 mm and thickness 0.9048 mm. The high-resolution CA is placed at 96.55 mm from the object center, in the source direction, producing spatial blockages of 0.1131×0.1131 mm and 0.25 mm thickness.

The test object is composed of a pyramidal shape composition located at the center of the volume; the pyramid is surrounded by nine spheres of different sizes (radii

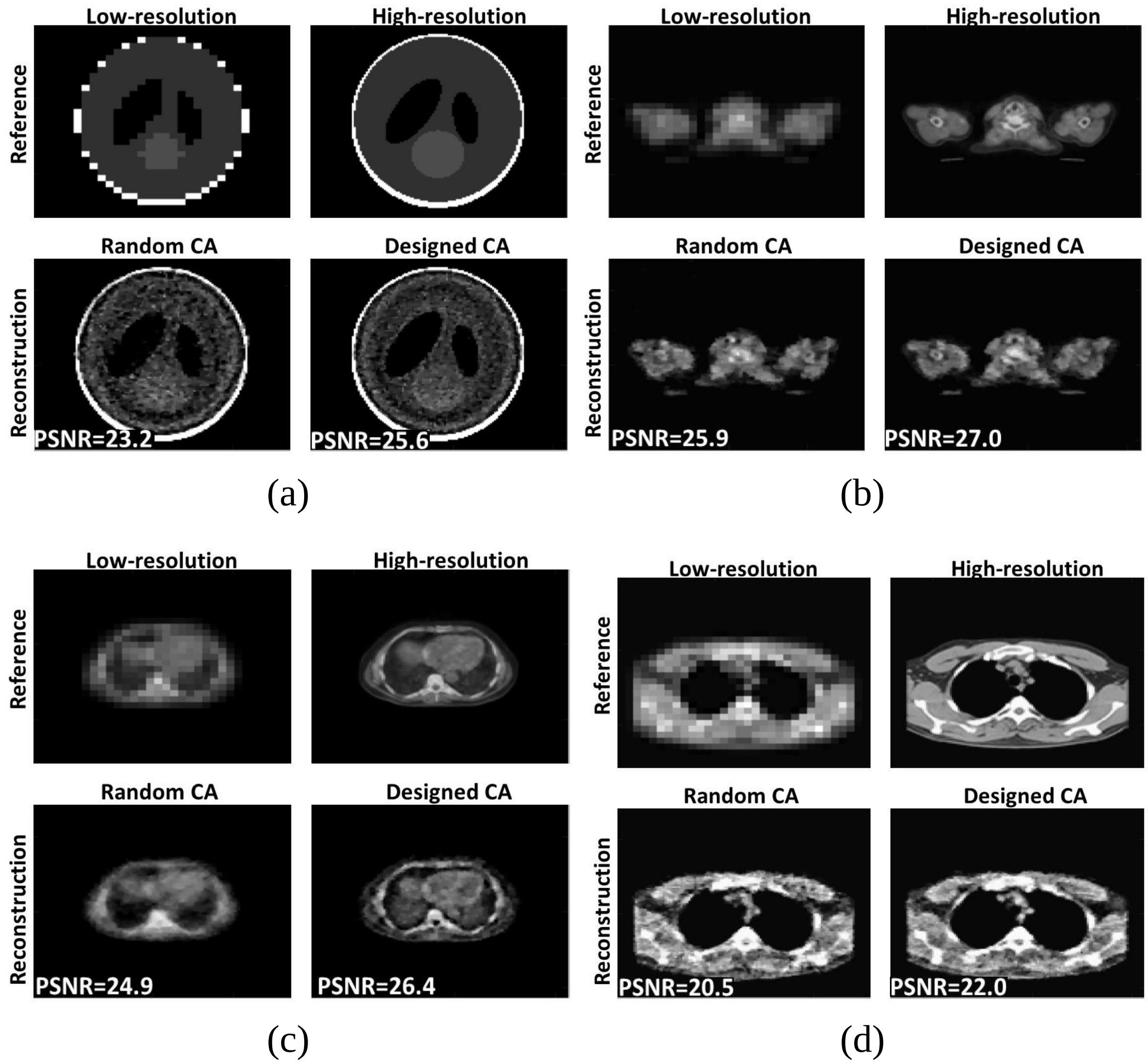

Figure 23. Reconstruction comparison from noisy measurements with SNR $= 15$ dB and $d = 16$ for all test data sets. Reference images include low resolution and high resolution data. PSNR values are calculated with respect to the high resolution ground truth. (a) 3D-Shepp-Logan phantom, (b) Multiple, (c) Abdomen, and (d) Thorax.

6mm, 3mm, and 1mm), which are diagonally arranged at the sides of the pyramid, and repeated every 120 degrees as illustrated in Fig. 24. All the elements are composed of $SpineBone$ material. The coded projections were simulated on GATE using the designed and random CA patterns, where parallel CPU clusters of the European

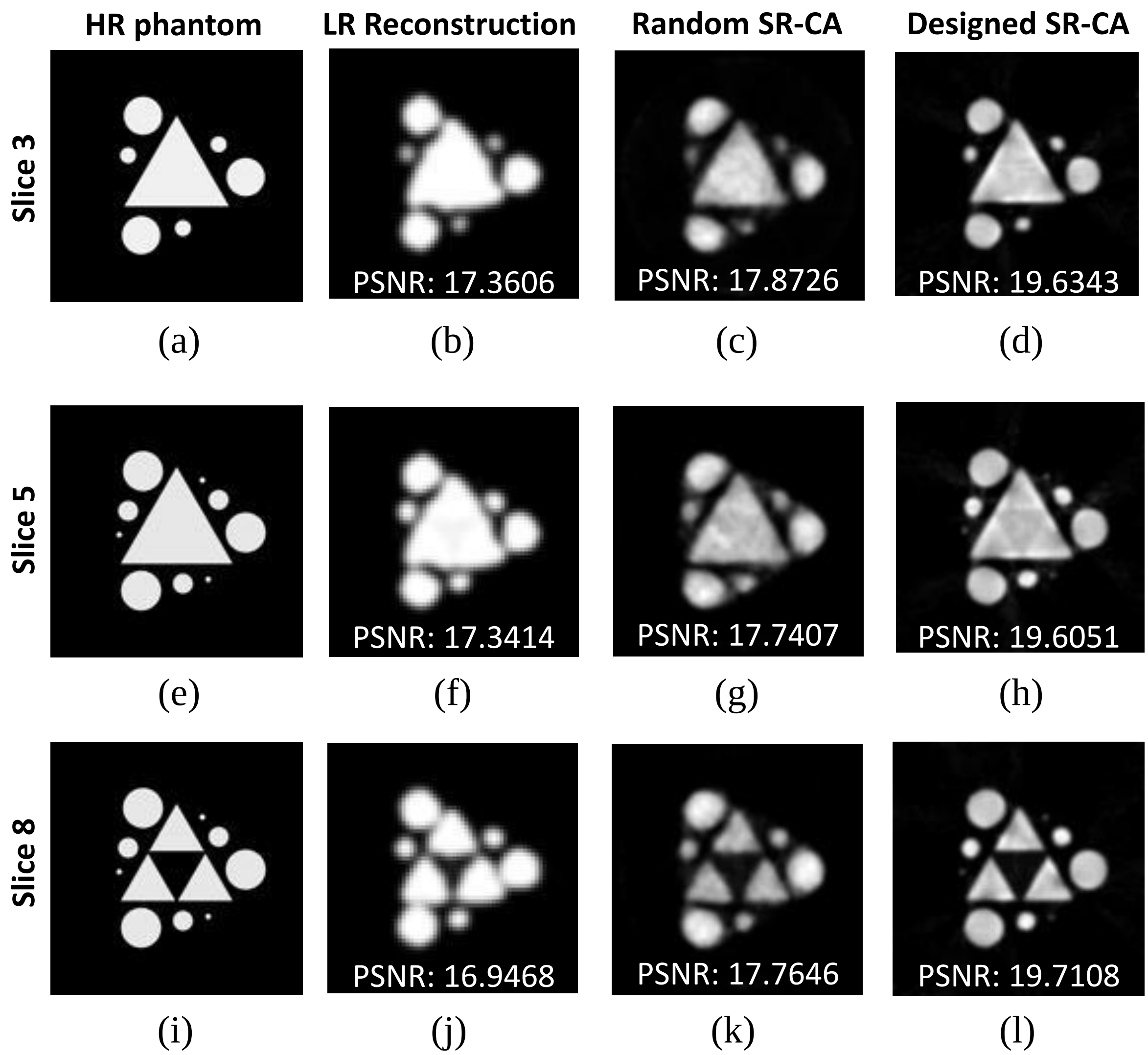

Figure 24. Reconstruction comparison of high-resolution images from Monte Carlo projections simulated with GATE, with random and designed CA for a SR factor $d = 2 \times 2$.

Grid Infrastructure, reduce simulation running times from several weeks to a few days [103]. The Monte Carlo simulated projections were used to recover the high-resolution

[103] Sorina Camarasu-Pop et al. “Monte Carlo simulation on heterogeneous distributed systems: A computing framework with parallel merging and checkpointing strategies”. In: *Future Generation Computer Systems* 29.3 (2013), pp. 728–738.

images. Figure 24 presents the obtained results for three object slices. These comparisons show the high-resolution ground truth in Figs.24 (a,e,i); the reconstruction from low-resolution projections (LR) without a coded aperture, scaled to the high-resolution image size in Figs.24 (b,f,j); and the high-resolution reconstructions using random and designed CA in Figs.24 (c,g,k) and Figs.24 (d,h,l), respectively. The improvements in the image quality from the designed patterns with respect to the random CA are easily noticeable, as sharper structures are obtained with the designed patterns. Numerically, the scaled LR reconstruction resulted in 16.4dB average PSNR across all slices, while the random and designed SR-CA attained 17.7 and 19.9dB, respectively. This implies a gain of up to 2.2 dB PSNR of the designed CA with respect to the random SR-CA, and 3.5 dB of PSNR when compared to the scaled LR reconstruction.

5.6. Discussion

The proposed coded aperture design method was tested under different scenarios, in which it demonstrated its advantages over purely random patterns. Notwithstanding, we have identified some aspects in which there is still place for improvement. In the proposed method, the regularization parameter tuning is a time-consuming process, since it requires three parameters $\rho_1, \rho_2,$ and ρ_3, whose values depend on the CA transmittance proportion and configuration of the acquisition system. Parameter tuning was conducted by fixing two parameters at a time and looking for convergence in the solution. Therefore, further work should be conducted towards more efficient parameter tuning methods. In the same direction, modern techniques involving deep learning could be exploited not only to develop parameter tuning strategies for this problem but also for designing the coded aperture patterns.

Another interesting further work is the extension of the proposed method to consider higher decimation factors than those considered in simulations presented in this Chapter, i.e., $d = 8 \times 8, 16 \times 16$, because one of the main constraints for these cases lies on manufacturing size limits for coded aperture fabrication. This is crucial to fit more CA features per unit area, thus yielding 1:8 or higher matching with respect to detector pixels.

5.7. Conclusions

This Chapter presented a method to design high-resolution coded apertures to be used in a compressive CBCT system with a low-resolution detector array such that, super-resolved images can be recovered without significantly changing the traditional architecture. The proposed method reduces the Gershgorin radii of the system matrix, as they describe the bounds of the eigenvalue distribution, to improve the condition of the inverse problem. Simulation results obtained with five different test data sets consistently validate the performance of the proposed CA for different transmittance values and super-resolution factors, obtaining improvements of up to 4 dB of PSNR with respect to non-designed coded apertures in the noiseless case. On the other hand, reconstructions from projections contaminated with Poisson noise for different SNR values demonstrated the robustness of the proposed coded apertures in noisy scenarios, where the designed CA improve random patterns in up to 4 dB of PSNR. These results were validated by Montecarlo simulations with the GATE toolbox. Further, it was shown that the computational load of the proposed approach is up to three orders of magnitude lower than the SVD-based CA design methods.

6. A Fan Beam Multi-Resolution Regularization

The reconstruction time in CT applications is a key factor for providing on-time diagnoses or conclusions from the CT images. However, in CT-based architectures such as the X-ray FB system, there still some drawbacks to provide fast and accurate reconstructions given the high computational load and high correlated linear problem. In this Chapter, a computed tomography reconstruction strategy is adopted to overcome this issue for recovering CT images acquired with a FB system.

6.1. Introduction

The FB is a CT system mainly composed of a source that emits fan-shaped energy. The interaction of this energy with 2D slices of a 3D object under observation allows to obtain the internal structure information of the object through energy alternations. The mathematical modeling of the FB system to acquire a single slice (CT image) relies on the characterization of the energy propagation through the discrete object using an over-determined matrix. Thus, the acquired image is the result of back-propagating the registered information from the detector to the pixel distribution. In this sense, the linear problem formulation offers the advantage of having a back-propagation solution, which is obtained by multiplying the acquired projections with the transpose of the acquisition system matrix [1]. However, even with these oversampling conditions, the back-propagation solution provides inaccurate images. Therefore, iterative solutions that correct the result at each step have been adopted. Precisely, this over-sampling particularity of the system entails high computational resources and elevated reconstruction times in the iterative reconstruction algorithm, where the complexity of these methods increases in proportion to the dimensionality and resolution of the data.
In contrast to traditional reconstruction methods, works in spectral imaging such as [26], have considered segmentation algorithms that group a set of similar pixels in ir-

regular neighborhoods of the image domain (so-called super-pixels) such that the total number of unknowns in the inverse problem is drastically reduced. This recovery approach based on super-pixels has been named MR reconstruction since the spatial representation of an image is summarized in a set of super-pixel elements, yielding to lower resolution representation of the image [104][105][106][107][108].

This Chapter introduces the MR reconstruction concept into the CT recovery problem by considering sets of similar pixel attenuation into square neighborhoods of the CT image to reduce the number of unknowns in the inverse problem, and provide faster reconstructions. To this end, a decimation matrix that accounts for squared pixel grouping is introduced into the traditional iterative problem, yielding a reduced number of variables in the formulation. Numerical experiments show an improvement by the proposed approach of up to 16 dB in terms of PSNR and a speedup up to 3.5 times compared with the traditional method that does not consider the MR concepts.

6.2. FB CT Image Acquisition and Reconstruction

Let $\mathbf{X} \in \mathbb{R}^{\sqrt{N}\times\sqrt{N}}$ be a 2D slice (image) of the 3D object under observation, and $\mathbf{x} \in \mathbb{R}^N$ its column-vector representation. Then, the forward projection operation of

---

[104] Radhakrishna Achanta et al. “SLIC Superpixels”. In: (2010), p. 15.

[105] Jiansheng Chen, Zhengqin Li, and Bo Huang. “Linear spectral clustering superpixel”. In: *IEEE Transactions on image processing* 26.7 (2017), pp. 3317–3330.

[106] Amir Said and William A Pearlman. “An image multiresolution representation for lossless and lossy compression”. In: *IEEE Transactions on image processing* 5.9 (1996), pp. 1303–1310.

[107] Adriana Gonzalez et al. “Multi-resolution compressive sensing reconstruction”. In: *arXiv preprint arXiv:1602.05941* (2016).

[108] Xing Wang and Jie Liang. “Multi-resolution compressed sensing reconstruction via approximate message passing”. In: *IEEE Transactions on Computational Imaging* 2.3 (2016), pp. 218–234.

the FB acquisition system can be considered as a linear problem of the form

$$\tilde{\mathbf{p}} = \mathbf{W}\mathbf{x}, \tag{84}$$

where $\tilde{\mathbf{p}} \in \mathbb{R}^{\tilde{M}}$ is the projections vector of $\mathbf{x}$ and $\mathbf{W} \in \mathbb{R}^{\tilde{M} \times N}$ denotes the acquisition system, whose rows models the energy interaction for each pixel. In an ideal model, the propagation described by the matrix $\mathbf{W}$ must be invertible, with dimensions $N = \tilde{M}$. However, in practice, there exists correlated rows in the matrix given that the coefficients characterizing the propagation reveal similarities between them. Thus, the direct inversion of the square system introduces inaccurate or noisy solutions of $\mathbf{x}$. To avoid this, the object under observation is over-sampled yielding an overdetermined system matrix $\mathbf{W}$ with $\tilde{M} > N$, which obtains redundant information and reduces issues of image underestimation. Nonetheless, the inversion of this overdetermined system demands high computational load and computer time.

Alternatively, a minimum norm least-squares formulation is used to find an approximation of $\mathbf{x}$ from the projections $\tilde{\mathbf{p}}$, and is expressed as

$$\hat{\mathbf{x}} = \underset{\mathbf{x}}{\operatorname{argmin}} \parallel \tilde{\mathbf{p}} - \mathbf{W}\mathbf{x} \parallel_2^2. \tag{85}$$

As a solution, the back-projection process turns back the measurements to the projection path, and can be written as

$$\mathbf{x}^* = \mathbf{W}^\intercal \tilde{\mathbf{p}}, \tag{86}$$

where Eq. (86) can be associated with the unfiltered back-projection process. Another solution to (85) can be found using the pseudo-inverse of the system as

$$\hat{\mathbf{x}} = \mathbf{W}^\dagger \tilde{\mathbf{p}}, \tag{87}$$

where a Moore-Penrose inverse $\mathbf{W}^\dagger$ can be calculated as $(\mathbf{W}^\intercal\mathbf{W})^{-1}\mathbf{W}^\intercal$, or equivalently expressed as $\mathbf{W}^\intercal(\mathbf{W}\mathbf{W}^\intercal)^{-1}$. Note that, the matrix $\mathbf{W}^\dagger$ is related with the term $(\mathbf{W}\mathbf{W}^{\intercal})^{-1}$, which plays the role of a high-pass filter, introducing a solution related with a filtered back projection [1]. The iterative reconstruction strategies, on the other hand, can be used to solve (85) such as the stochastic gradient descent (SGD) method. This method establishes that an initial image $\mathbf{x}_0$ can iteratively converge to a desired quality of reconstruction by sequentially improving solutions $(\mathbf{x}_1, \mathbf{x}_2, \cdots, \mathbf{x}_z)$. Thus, with a current image estimation $\mathbf{x}_z$, the method finds $\mathbf{x}_{z+1}$. Specifically, the updating step of the SGD approach for solving (85) is given by

$$\mathbf{x}_{z+1} = \mathbf{x}_z - \gamma \nabla f(\mathbf{x}_z) = \mathbf{x}_z - \gamma \mathbf{W}^{\intercal} \left(\mathbf{W}\mathbf{x}_z - \tilde{\mathbf{p}} \right), \tag{88}$$

where γ is the step size to regularize the changes on each estimation of $\mathbf{x}_z$, and $\Delta f(\mathbf{x})$ is the Jacobi derivation of $f(\mathbf{x}) = \parallel \tilde{\mathbf{p}} - \mathbf{W}\mathbf{x} \parallel_2^2$. Observe that, compared to the back-projection solution, the computational resources in the IR process is still a drawback since the requirements (e.g. the use of $\mathbf{W}^{\intercal}$) are extended in time during z iterations. Thus, algorithms such as the stochastic gradient descent with Nesterov (SGDN) [109] modify the gradient step on the SGD strategy for a faster convergence. One strategy to reduce the computational load and the number of elements on the IR-based methods entails introducing an MR decimation matrix in the linear problem [26]. To extend the MR insights to the CT recovery problem, Eq. (84) is modified by introducing the matrix **D** that models the MR decimation as

$$\tilde{\mathbf{p}} = \mathbf{W}\mathbf{D}^{\intercal}\bar{\mathbf{x}}, \tag{89}$$

where $\mathbf{D}^{\intercal}$ is the transpose of **D**. Note that, having **D** into the problem, the approach in (85) need to be updated to find the new MR scene. Hence, the cost function to be

[109] Atilim Gunes Baydin et al. “Online learning rate adaptation with hypergradient descent”. In: *arXiv preprint arXiv:1703.04782* (2017).

minimized is rewritten as

$$\hat{\mathbf{x}} = \mathbf{D}^{\intercal}\{\underset{\bar{\mathbf{x}}}{\operatorname{argmin}} \parallel \tilde{\mathbf{p}} - \mathbf{W}\mathbf{D}^{\intercal}\bar{\mathbf{x}} \parallel^2\}, \tag{90}$$

where $\hat{\mathbf{x}}$ is the response on the image domain and $\bar{\mathbf{x}} = \mathbf{D}\mathbf{x}$ is the MR solution. Then, the updating step of the MR-based SGD approach, which includes **D**, can be written as

$$\bar{\mathbf{x}}_{z+1} = \bar{\mathbf{x}}_z - \gamma\nabla f(\mathbf{x_z}) = \bar{\mathbf{x}}_z - \gamma\mathbf{D}\mathbf{W}^{\intercal}\left(\mathbf{W}\mathbf{D}^{\intercal}\bar{\mathbf{x}}_z - \tilde{\mathbf{p}}\right). \tag{91}$$

Note that by assuming that any CT image can be summarized in a set of c super-pixels instead of $N = \sqrt{N}\sqrt{N}$ pixels, the number of unknowns using the MR-based update step in (91) can be reduced from N to c ($c \ll N$).

6.3. MR Decimation Matrix Design

The construction of the MR decimation matrix **D** is based on the analysis of the homogeneous zones of the image under observation, as presented in Algorithm 3. The main objective is to decompose the input image **X** $\in \mathbb{R}^{\sqrt{N}\times\sqrt{N}}$ into subsets of square super-pixels and build **D** considering the inputs of the Algorithm which are: the image, a tolerance level σ and a set of coordinate points $\mathbf{\Omega}$. The first step in the Algorithm is to define the possible sizes **S** of the squared super-pixels (Line 2). Later, to build each super-pixel, a random point $(\hat{i}, \hat{j})$ from the set $\mathbf{\Omega}$ is selected. Then, a hypothetical super-pixel **B** is generated (Line 7), where in this set is important to ensure that all points are available in $\mathbf{\Omega}$, performing a set of coordinates that have not been assigned to any super-pixel before (this is required to assign each spatial pixel to only one super-pixel). After building **B**, the expected value of **X** on this zone **B**, denoted as $E\{\bar{\mathbf{X}}_{\mathbf{B}}\}$, is computed as in Line 10. The spatial positions with error values lower than the tolerance σ (line 11) are labeled with 1 in a new matrix $\mathbf{\Upsilon}$ as in Lines 12 to 13. Then, the matrix $\mathbf{\Upsilon}$ is column-vectorized and added to the MR matrix **D** as a new row (Line 14). As a result, at each iteration, elements are assigned to the c-th super-pixel and removed from the sets $\hat{\mathbf{\Omega}}$ (set of points coordinates available for being chosen as the random corner point) and Ω. After building all the possible super-pixel elements under the tolerance condition over the entire image, the current index z is updated, and the procedure is repeated for a new super-pixel size of the non-grouped zones. The output of the Algorithm is the matrix **D**.

Algorithm 3 MR Matrix **D** Construction for Rectangular Super-Pixels

procedure DECIMATION_MATRIX_DESIGN(Image $\mathbf{X} \in \mathbb{R}^{\sqrt{N}\times\sqrt{N}}$, set of coordinate points $\mathbf{\Omega}$, tolerance σ.)
  $\mathbf{S} = [\lceil\frac{\sqrt{N}}{2}\rceil, \lceil\frac{\sqrt{N}}{2^2}\rceil, \ldots, 1]$, $z = 0$, $c = 0$ ▷ Initialize super-pixel sizes
  while $|\Omega| > 0$ **do**
    $\hat{\mathbf{\Omega}} = \mathbf{\Omega}$ ▷ Generate a new set of available points
    while $|\hat{\mathbf{\Omega}}| > 0$ **do**
      $(\hat{i}, \hat{j}) \in \hat{\mathbf{\Omega}}$ ▷ Choose an eligible top-left point
      $\mathbf{B} = \{(i,j)|i = [\hat{i}, \ldots, \min\left(\hat{i} + \mathbf{S}(z), \sqrt{N}\right)], j = [\hat{j}, \ldots, \min\left(\hat{j} + \mathbf{S}(z), \sqrt{N}\right)]\}$
      ▷ Generate the hypothetical super-pixel **B**
      if $\mathbf{B} \in \Omega$ **then**
        $\tilde{\mathbf{p}} = E\{\bar{\mathbf{X}}_{\mathbf{B}}\}$ ▷ Calculate the expected value of **X** in spatial coordinates in set **B**
        if $\max(MSE(\mathbf{p}, \bar{\mathbf{X}}_{\mathbf{B}})) < \sigma$ **then**
          $\mathbf{\Upsilon} = \mathbf{0}_{\sqrt{N}\times\sqrt{N}}$
          $\mathbf{\Upsilon}_{(i,j)} = 1$ for $(i,j) \in \mathbf{B}$ ▷ Create an indicator matrix for the c-th super-pixel
          $(\mathbf{D})_c = vec(\mathbf{\Upsilon})$ ▷ Vector form of $\mathbf{\Upsilon}$ is assigned as a new row of MR matrix
          $c = c + 1$ ▷ Update MR super-pixels counter
          $\mathbf{\Omega} = \mathbf{\Omega} - \mathbf{B}$ ▷ Update available points
          $\hat{\mathbf{\Omega}} = \hat{\mathbf{\Omega}} - \mathbf{B}$ ▷ Update eligible top-left points
        else
          $\hat{\mathbf{\Omega}} = \hat{\mathbf{\Omega}} - (\hat{i}, \hat{j})$ ▷ Remove the corner point
      else
        $\hat{\mathbf{\Omega}} = \hat{\mathbf{\Omega}} - (\hat{i}, \hat{j})$
    $z = z + 1$ ▷ Change super-pixel size index
return MR decimation matrix **D**

6.4. Simulations and Results

Numerical simulations were conducted on a synthetic data set to test the performance of the proposed MR-based CT reconstruction. The spatial resolution of the data is 128×128 pixels, where different noise level values on the measurements and data ratio $\Gamma = M/N$ are tested. For comparison purposes, reconstructions using the proposed MR approach in (90) are compared with approaches that solve the inverse problem shown in (85) using SGD and SGDN from [109] as reconstruction algorithm. For all cases, the number of iterations for the reconstruction process was fixed to 5000 and each result is the average of 10 runs[110], where on each simulation, the CT measurements are obtained using the model in (84). It is important to remark that a CT image is taken as a known distribution to build the MR matrix. The reconstruction quality is expressed in terms of PSNR.

6.4.1. MR Reconstruction Quality In order to qualitatively analyze the performance with the proposed MR assumption, this section compares the SGD and SGDN reconstruction methods using the proposed MR framework, named as SGDMR and SGDNMR, respectively; and the methods without including the MR matrix in the problem formulation, i.e., the SGD and SGDN methods [109]. The experiment solves the CT images preserving the same number of projections, the same solver of the minimization problem based on l_2, and keeping 5000 iterations as an initial distribution of the image in all cases. Figure 25 shows the relationship between the average PSNR result and the data ratio Γ. As can be noticed, the MR-based approaches improve the quality of the reconstructed images in up to 15 dB of PSNR; this quality improvement is caused by reducing the number of variables to reconstruct induced by the MR decimation matrix.

In Figure 26 is shown the reconstructed images using all the recovery approaches

---

[110] All simulations were conducted and timed using an Intel Core i7-6700 @3.40GHz processor and 32GB RAM.

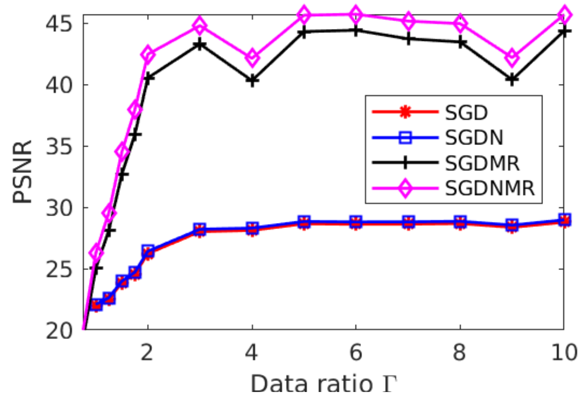

Figure 25. Quality reconstruction comparison for the phantom data-set

when $\Gamma = 2$, where the methods using the MR approach show better results. In particular, observe that the SGD and SGDN reconstructions exhibit circular artifacts that are vanished with the SGDMR and SGDNMR methods.

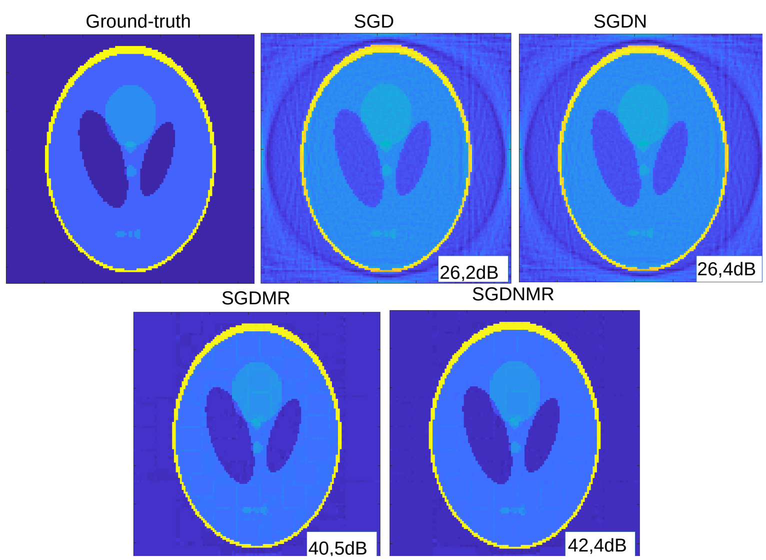

Figure 26. Comparison of the reconstructed images for $\Gamma = 2$.

6.4.2. Computation Time Analysis of the MR Reconstructions For a fair comparison, the number of iterations of each recovery methods is the same, i.e., 5000 iterations, to compare the required computation time on each reconstruction process, including the MR approaches. The reconstructing time in seconds of each simulated scenario at different data ratios is shown in Fig. 27, where the MR approach is up to 3.5x faster than the non-MR approaches. This reduction in the required recon-

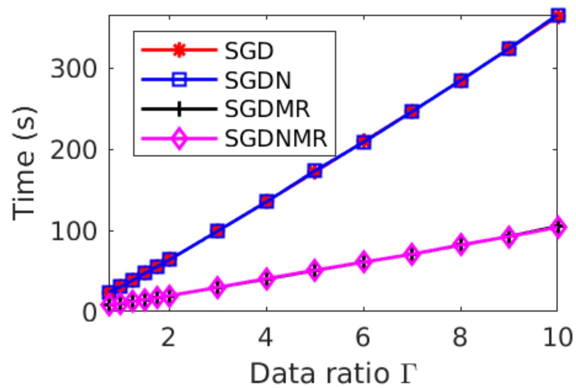

Figure 27. Comparison of the time required in the reconstruction process by each approach for different data ratios.

struction time is attributed to the lower number of variables to reconstruct respect to the traditional non-MR approach, where the proposed approach requires lower size matrix products.

6.4.3. Reconstruction Quality Analysis in Presence of Noise Several simulations were performed to evaluate the robustness of the MR-based methods in noisy scenarios, including 10 and 20 dB of SNR of additive white Gaussian noise (AWGN) in the measurements. The quality of the reconstruction images in terms of the PSNR for different values of data ratio Γ are shown in Fig. 28. As expected, the PSNR is lower in high noise levels, but it is essential to remark that the proposed approach improves the traditional approaches in up to 12dB even for 10 dB of SNR. Also, the SGDMR and SGDNMR approach results in the same quality of the reconstructed image in opposite to the results in Fig.25.

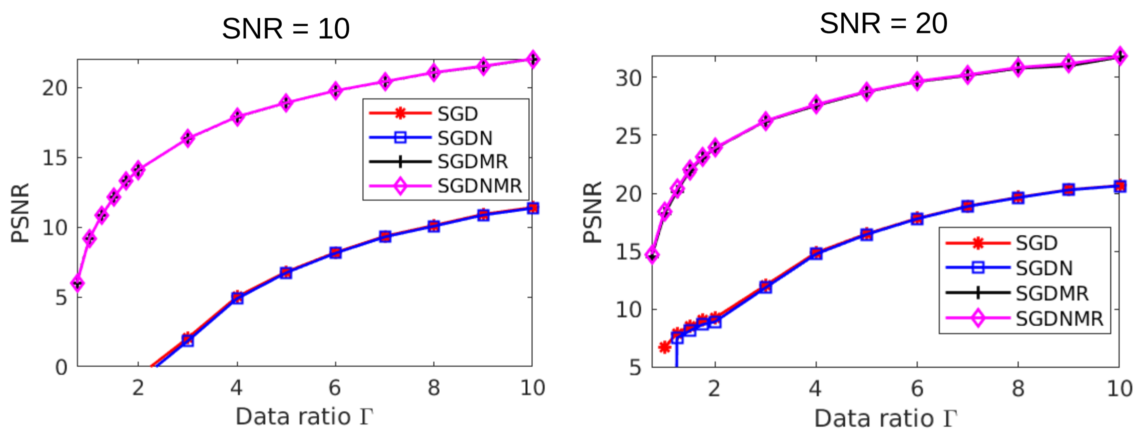

Figure 28. Quality reconstruction comparison for different noise levels. Left image with 10dB of SNR and right image with 20dB of SNR.

6.5. Conclusions

A multi-resolution iterative reconstruction scheme for CT image recovery has been proposed. This approach exploits the neighborhood similarities, representing each uniform square zone with a single value, allowing to reduce the number of elements in the reconstruction and the complexity of the inverse problem. Moreover, the proposed approach improves the relation measurements/variables of the sensing matrix. Simulation results show that the proposed method improves the reconstruction PSNR by up to 16 dB and is 3.5x faster than the traditional reconstruction method, even in the presence of noise. It is important to remark that this work exploits the fact that exists a previous knowledge of the image. Taking this into account for future work is possible to use a reduced set of the iterations to obtain a particular quality image and apply the proposed strategy to the rest of the iterations to generate relevant results.

7. Extension to Compressive Spectral Imaging

In spectral imaging, the spatial information varies as a function of a range of wavelengths, yielding a three-dimensional representation of the scene under observation. Traditional spectral image acquisition techniques integrate imaging and spectroscopic technologies into one system to perform a scanning of the scene across the spatial (line-wise or point-wise) or the spectral (wavelength-wise) dimensions. In contrast, compressive snapshot-based acquisition systems allow to acquire the spatio-spectral information in one shot, providing a faster image acquisition. A compressive spectral imaging (CSI) snapshot system captures the 3D spatio-spectral data using a 2D encoded projection of the spectrally dispersed scene. For the encoding of the incoming information, CA such as random block-unblock and colored coded aperture (CCA) have been used in the literature. In particular, the CCA patterns are composed of optical filters that provide a improved modulation of spatial and spectral information respect to the random block-unblock patterns, however, the fabrication cost and complexity of the CCA are higher as well. To be precise, the cost of the real implementation of a CCA directly depends on the number of filters to be used and the number of snapshots to be captured. This is because each element in the CCA is free of revealing a different and unique physical property to be implemented.
This Chapter extends the results of this thesis to explore an alternative CA optimization design considering the restrictions of the pattern of a moving CCA in a CSI system. Simulations show that the designed pattern improves the quality of the reconstruction of the spectral data cube through a physically realizable pattern.

7.1. Compressive Spectral Imaging

Spectral images can be described as images with spatial information across different wavelengths, where the resulting three-dimensional data set is known as spatio-spectral data cube. The spatio-spectral information is valuable in applications such as quality control in food and industrial agriculture [111][112][113], medical imaging [114][115][116], remote sensing [117], art conservation [118][119][120], gas identification [121][122],

---

[111] P.S. Thenkabail and J.G. Lyon. *Hyperspectral Remote Sensing of Vegetation*. CRC Press, 2016.

[112] Di Wu and Da-Wen Sun. "Advanced applications of hyperspectral imaging technology for food quality and safety analysis and assessment: A review—Part I: Fundamentals". In: *Innovative Food Science & Emerging Technologies* 19.6 (2013), pp. 1–14.

[113] Karen Sánchez et al. "Classification of Cocoa Beans Based on their Level of Fermentation using Spectral Information". In: *TecnoLógicas* 24.50 (2021), pp. 172–188.

[114] Matthew E Martin et al. "Development of an advanced hyperspectral imaging (HSI) system with applications for cancer detection". In: *Annals of biomedical engineering* 34.6 (2006), pp. 1061–1068.

[115] Guolan Lu et al. "Spectral-spatial classification for noninvasive cancer detection using hyperspectral imaging". In: *Journal of biomedical optics* 19.10 (2014), pp. 106004–106004.

[116] Qingli Li et al. "Review of spectral imaging technology in biomedical engineering: achievements and challenges". In: *Journal of biomedical optics* 18.10 (2013), pp. 100901–100901.

[117] Kareth M León-López et al. "Anomaly Detection and Classification in Multispectral Time Series Based on Hidden Markov Models". In: *IEEE Transactions on Geoscience and Remote Sensing* 60 (2022), pp. 1–11.

[118] Haida Liang. "Advances in multispectral and hyperspectral imaging for archaeology and art conservation". In: *Applied Physics A* 106.2 (2012), pp. 309–323.

[119] Kirk Martinez et al. "Ten years of art imaging research". In: *Proceedings of the IEEE* 90.1 (2002), pp. 28–41.

[120] John K Delaney et al. "Visible and infrared imaging spectroscopy of Picasso's Harlequin musician: mapping and identification of artist materials in situ". In: *Applied spectroscopy* 64.6 (2010), pp. 584–594.

[121] Dimitris Manolakis and Gary Shaw. "Detection algorithms for hyperspectral imaging applications". In: *IEEE signal processing magazine* 19.1 (2002), pp. 29–43.

[122] Dimitris Manolakis, David Marden, Gary A Shaw, et al. "Hyperspectral image processing for automatic target detection applications". In: *Lincoln laboratory journal* 14.1 (2003), pp. 79–116.

security [121][122][123], among others [124]. In spite of the high range of applications of these images, the implementation of spectral sensing systems, and the acquisition and processing of these data pose significant challenges. Traditional spectral imaging (SI) systems generally are based on a full sampling scheme, which effectively senses the whole spatio-spectral data cube getting the spectral information pixel-by-pixel or line-by-line at the expense of a time-consuming acquisition. Thereby, full sampling scheme can only be applied to static scenes or scenes with slow movement [125]. As an alternative, CS concepts has been introduced into SI to reduce the number of measurements and time consumption in the spectral images acquisition. CS handles a large amount of data with fewer measurements than those required by the well-known Shannon-Nyquist sampling theorem [124]. Hence, applying the CS concept to the SI systems has generated the development of compressive spectral imaging (CSI) systems [125][126], including the CASSI, the multi-aperture filtered camera (MAFC), and the snapshot hyperspectral imaging Fourier transform (SHIFT) system. CSI measures spatio-spectral information in such a way that the data cube is sensed and compressed at the same time. Specifically, the CSI spatio-spectral information is acquired in 2D coded projections or measurements of the underlying scene using a CA, where the number of measurements in the detector is far less than when using

---

[123] Chein-I Chang. “Hyperspectral Target Detection: Hypothesis Testing, Signal-to-Noise Ratio, and Spectral Angle Theories”. In: *IEEE Transactions on Geoscience and Remote Sensing* 60 (2021), pp. 1–23.

[124] Adrian Stern. *Optical compressive imaging*. CRC Press, 2016.

[125] Xun Cao et al. “Computational snapshot multispectral cameras: Toward dynamic capture of the spectral world”. In: *IEEE Signal Processing Magazine* 33.5 (2016), pp. 95–108.

[126] Nathan A Hagen and Michael W Kudenov. “Review of snapshot spectral imaging technologies”. In: *Optical Engineering* 52.9 (2013), pp. 090901–090901.

a full sampling scheme [127128 34129].

The pattern distribution of the CA is a key element in the system to sample and, then, recovering high quality reconstructions [333454]. Different works have been proposed to design the pattern of the CA, where state-of-the-art CA designs include approaches based on singular value decomposition [130131], genetic algorithms [33], adaptive schemes [132133], shrinkage methods [130], computational-based [13490], among

---

[127] Gonzalo R Arce et al. "Snapshot compressive multispectral cameras". In: *Wiley Encyclopedia of Electrical and Electronics Engineering* (1999), pp. 1–22. DOI: `https://doi.org/10.1002/047134608X.W8345`.

[128] Yuehao Wu et al. "Development of a digital-micromirror-device-based multishot snapshot spectral imaging system". In: *Optics letters* 36.14 (2011), pp. 2692–2694.

[129] Xin Yuan, David J Brady, and Aggelos K Katsaggelos. "Snapshot compressive imaging: Theory, algorithms, and applications". In: *IEEE Signal Processing Magazine* 38.2 (2021), pp. 65–88.

[130] Michael Elad. "Optimized projections for compressed sensing". In: *IEEE Transactions on Signal Processing* 55.12 (2007), pp. 5695–5702.

[131] M. Aharon, M. Elad, and A. Bruckstein. "K-SVD: An algorithm for designing overcomplete dictionaries for sparse representation". In: *IEEE Transactions on Signal Processing* 54.11 (2006), pp. 4311–4322. DOI: `10.1109/TSP.2006.881199`.

[132] Zhongmin Wang, Gonzalo R Arce, and Jose L Paredes. "Colored random projections for compressed sensing". In: *2007 IEEE International Conference on Acoustics, Speech and Signal Processing-ICASSP'07*. Vol. 3. IEEE. 2007, pp. III–873–III–876.

[133] Alejandro Parada-Mayorga and Gonzalo R. Arce. "Colored Coded Aperture Design in Compressive Spectral Imaging via Minimum Coherence". In: *IEEE Transactions on Computational Imaging* 3.2 (2017), pp. 202–216. DOI: `10.1109/TCI.2017.2692649`.

[134] Vahid Abolghasemi, Saideh Ferdowsi, and Saeid Sanei. "A gradient-based alternating minimization approach for optimization of the measurement matrix in compressive sensing". In: *Signal Processing* 92.4 (2012), pp. 999–1009.

others approaches [135][136][137]. On the other hand, works such as [18], rearranged the CA in order to design its structure for CT imaging. This strategy has shown that the optimization based on a gradient descent strategy allows to design the CA elements across the different CA dimensions, including the number of snapshots or angles to be acquired. However, up to our knowledge, this methodology has not been exploited in CSI systems to design the CA.

This Chapter develops a CCA optimization that design the CA structure considering the physical restrictions of the imaging system by adding variability and uniformity constraints to the formulation. To this end, the CCA is rearranged and its distribution is updated via the gradient descent method and subjected to the given constraints, which allows to handle physical restrictions such as the number of filters in the CCA. Additionally, a novel moving strategy is considered in the design, which can be implemented as a moving colored lithographic mask using a micro-piezo electric device. Figure 29 depicts the physical sensing phenomenon in the CASSI system, where the CCA can be moved vertically to acquire two different snapshots.

7.1.1. The CASSI system The CASSI system modulates the light reaching the focal plane array (FPA) by using coded apertures and dispersive elements. Figure 29 introduces the effect of this modulation in data propagation and describes each blockage with color filters in each coded aperture. The CCA patterns are created through a micro-lithography process to improve the manufacturing accuracy of color using different filters, so that not only spatial modulation can be performed, but spec-

[135] Michael Lustig, David Donoho, and John M Pauly. "Sparse MRI: The application of compressed sensing for rapid MR imaging". In: *Magnetic Resonance in Medicine: An Official Journal of the International Society for Magnetic Resonance in Medicine* 58.6 (2007), pp. 1182–1195.

[136] Zhongmin Wang and Gonzalo R Arce. "Variable density compressed image sampling". In: *IEEE Transactions on image processing* 19.1 (2009), pp. 264–270.

[137] W. Chen, M. R. D. Rodrigues, and I. J. Wassell. "Projection Design for Statistical Compressive Sensing: A Tight Frame Based Approach". In: *IEEE Transactions on Signal Processing* 61.8 (2013), pp. 2016–2029.

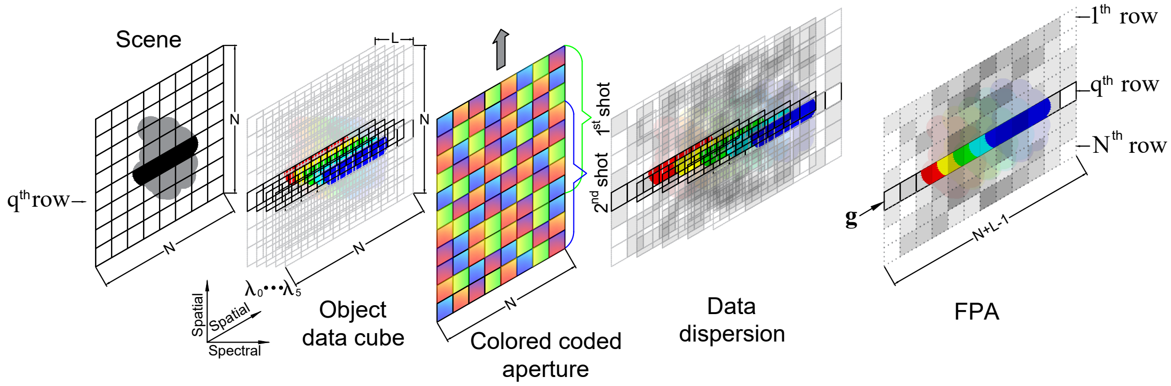

Figure 29. Physical description of the sensing phenomenon in the color CASSI system. The L spectral band of the data cube $\mathbf{F}$ is spatially and spectrally encoded by a moving color-coded aperture, and dispersed by a prism. The detector captures the intensity $\mathbf{g}$ by integrating the coded dispersed light.

tral modulation as well. Therefore, a CCA $\mathbf{T}^{\ell}_{mnk}$ can be defined as an arrangement of binary elements $\mathbf{T}_{mn}$ for each of the L bands, as it is presented in fig. 30, it modulates spatio-spectral image data $\mathbf{F}_{mnk}$, where m and n index space coordinates, k determines k^{th} spectral bands, and ℓ index the number of snapshots captured using different CCA distributions.

The FPA measurement value represented by this symbol is defined as:

$$\mathbf{Y}^{\ell}_{mn} = \sum_{k=0}^{L-1} \mathbf{T}^{\ell}_{m(n-k)k}\mathbf{F}_{m(n-k)k} + \boldsymbol{\omega}_{mn}, \tag{92}$$

where $m, n = 0, 1, \dots, N-1$, $k = 0, 1, \dots, L-1$, and $\boldsymbol{\omega}$ represents the noise of the sensing system. Notice that $\mathbf{F} \in \mathbb{R}^{N^2L}$, $\mathbf{T}^{\ell} \in \mathbb{R}^{N^2L}$, and $\mathbf{Y}^{\ell} \in \mathbb{R}^{N^2}$.

The multispectral signal $\mathbf{F} \in \mathbb{R}^{N\times N\times L}$, or its vector representation $\mathbf{f} \in \mathbb{R}^{N\cdot N\cdot L}$ is S-sparse on some basis $\boldsymbol{\Psi}$. Therefore, the signal can be approximated by the linear combination of the S vector from $\boldsymbol{\Psi}$ and $S \ll (N \cdot N \cdot L)$, such as $\mathbf{f} = \boldsymbol{\Psi\theta}$. Then, a projection in a CASSI system is given by $\mathbf{y} = \mathbf{H}\boldsymbol{\Psi\theta} = \mathbf{A}\boldsymbol{\theta}$, where $\mathbf{H}$ is the matrix structure, determined by the coded aperture entry and the dispersion effect, thereby,

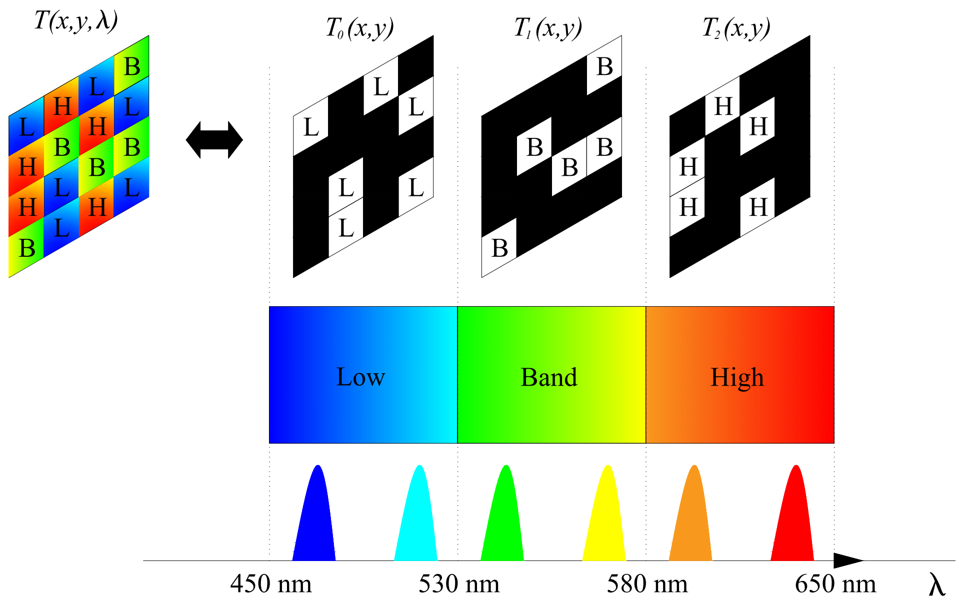

Figure 30. CCA with low, band and high pass filters and its equivalent set of binary coded apertures.

the matrix $\mathbf{A} = \mathbf{H\Psi}$ works as the sensing matrix of the sparse coefficients of the image. An estimate of spatio-spectral data cube from the measurements $\mathbf{Y}$ can be attained by solving the optimization problem,

$$\hat{\mathbf{f}} = \mathbf{\Psi}\left\{\underset{\boldsymbol{\theta}}{\operatorname{argmin}}\|\mathbf{y}-\mathbf{H\Psi}\boldsymbol{\theta}\|_2+\tau\|\boldsymbol{\theta}\|_1\right\}, \tag{93}$$

where τ is a regularization constant. In this contest, the basis $\mathbf{\Psi}$ is set with a Kronecker product between a 2D-Wavelet Symmlet 8 basis and a 1D-Discrete Cosine Transform. The solution of the problem in (93) is obtained with the GPSR algorithm, due to the quality of the reconstructed dataset rises or drops subject to the structure of the CCA, the reconstruction quality could be assessed by any other algorithm as well.

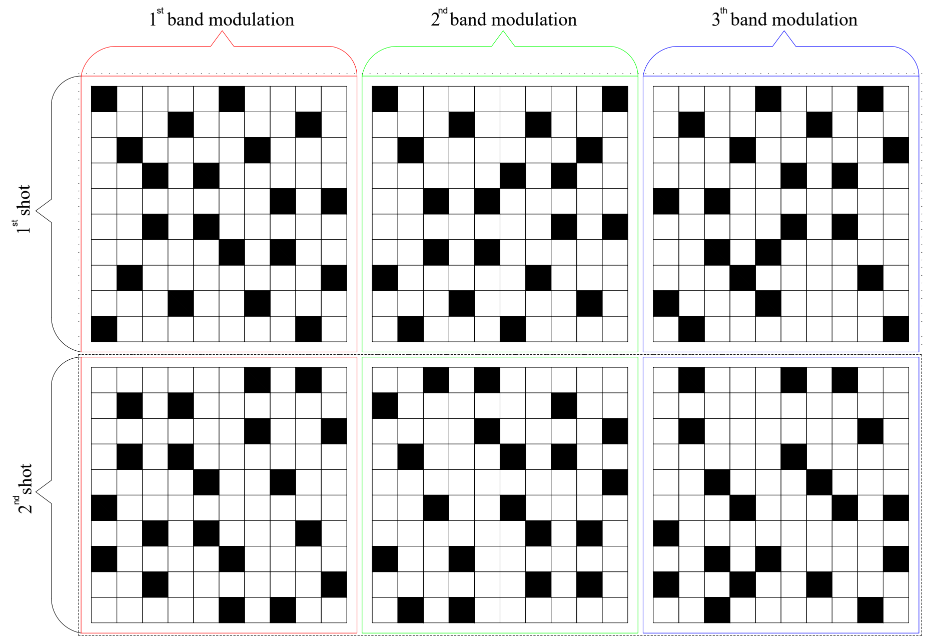

Figure 31. Proposed matrix $\mathbf{X}$ arrangement of a random CCA in binary representation to modulate a spatio-spectral data cube of dimensions $10 \times 10 \times 3$, and for 2 snapshots.

7.2. Colored Coded Aperture Optimization

The optimization proposed for the CCA structure is based on the promotion of the variability and uniformity. In this context, a bidimensional arrangement of the binary CCA representation can be used instead the provided in $\mathbf{T}$, with the aim of reducing the complexity of a CCA design proposed in this work. The matrix arrangement is defined as the horizontal concatenation of the L binary CA, and the subsequent vertical concatenation of the codes for the $\mathbf{K}$ shots. Then, a rearranged form of the CCA binary matrix is defined as $\mathbf{X} = \left[(\mathbf{X}^1)^\intercal, \ldots, (\mathbf{X}^i)^\intercal, \ldots (\mathbf{X}^K)^\intercal\right]^\intercal$, such that $\mathbf{X} \in \mathbb{R}^{KN \times NL}$, and $\mathbf{X}^i \in \mathbb{R}^{N \times N \cdot L}$. A brief representation of the resulting array is displayed in fig. 31, it show a CCA witch modulates a spatio spectral data cube of dimensions $10 \times 10 \times 3$, and for 2 shots.

The variability takes into account the reduction of the correlation between the rows and columns of the $\mathbf{X}$ matrix. Uniformity refers to the regularity of the sensing process through spatial dimensions, spectral bands, and the number of snapshots. In addition, two other considerations are used to guide the CA mask design process, considering cost and manufacturing complexity.

7.2.1. Variability Constraint The sampling process is directly affected by the CCA from Eq.(92), therefore $\mathbf{X}$. The Gram matrix of $\mathbf{X}$ is used as a constraint in the optimization problem, and its design results in a low correlation between rows and columns of $\mathbf{X}$. The row-wise and column-wise correlation defines the variability constraint as:

$$\underset{\mathbf{X}}{\operatorname{argmin}} \|\mathbf{I}_1 - \mathbf{X}\mathbf{X}^\intercal\|_F^2, \tag{94}$$

$$\underset{\mathbf{X}}{\operatorname{argmin}} \|\mathbf{I}_2 - \mathbf{X}^\intercal\mathbf{X}\|_F^2, \tag{95}$$

where $\mathbf{I}_1$ and $\mathbf{I}_2$ are identity matrices of size $KN \times KN$, and $LN \times LN$, respectively, and $\mathbf{X}$ is the optimization variable

7.2.2. Uniformity Constraint The uniformity constraint promotes the reduction of the spatial, spectral and snapshot correlation of the voxels in the acquisition process. In the case of the snapshots, when multiple snapshots are acquired, the number of times a voxel is sensed across snapshots given a CCA arrangement $\mathbf{X}$, can be calculated as the product $\mathbf{RX}$, where $\mathbf{R} = [\mathbf{I}_1, \cdots, \mathbf{I}_k]^\intercal$, and $\mathbf{I}_i$ is an identity matrix of size $N \times N$. Then, the snapshots uniformity can be minimized by solving,

$$\underset{\mathbf{X}}{\operatorname{argmin}} \|\mathbf{U} - \mathbf{RX}\|_F^2, \tag{96}$$

where $\mathbf{U}$ is a matrix with constant values.

Regarding the spectral sensing, the uniformity is guaranteed if the number of times a spectral voxel is sensed is as uniform as possible, and it is calculated as $\mathbf{XD}$, with $\mathbf{D} = [\mathbf{0}^\intercal_{N\times L-L}, \mathbf{I}^\intercal_N, \mathbf{0}^\intercal_{N\times L-1}, \ldots, \mathbf{0}^\intercal_{N\times L-1}, \mathbf{I}^\intercal_N, \mathbf{0}^\intercal_{N\times L-L}]^\intercal$, where $\mathbf{0}_{N\times L-1}$ is a $0-$ valued $N \times L - 1$ matrix, and $\mathbf{I}_N$ is an identity $N \times N$ matrix. The uniformity is then given by the constraint,

$$\underset{\mathbf{X}}{\operatorname{argmin}} \|\mathbf{V} - \mathbf{X}\mathbf{D}\|_F^2, \tag{97}$$

where $\mathbf{V}$ is a matrix with constant values, keeping the sensing proportions.

The purpose of the spatial uniformity is to avoid the clusters of one-valued entries both in the columns, and in the rows of the CA pattern. These constraints are defined as,

$$\underset{\mathbf{X}}{\operatorname{argmin}} \|\mathbf{B} - \mathbf{X}\mathbf{W}\|_F^2, \tag{98}$$

$$\underset{\mathbf{X}}{\operatorname{argmin}} \|\mathbf{C} - \mathbf{Z}\mathbf{X}\|_F^2, \tag{99}$$

where $\mathbf{B}$ and $\mathbf{C}$ are matrices with constant values, $\mathbf{W}$ and $\mathbf{Z}$ are positive definite Toeplitz matrices of size $LN \times LN$ and $KN \times KN$ respectively. The selection of the number of 1-value diagonals in the Toeplitz matrices determine the number of neighbor pixels to analyze of a row/column. The expected behavior of the matrices as in the previous constraints is to be as constant as possible and therefore promote a more uniform sensing.

Considering the variability constraints in Eqs. (94) and (95), and the uniformity constraints in Eqs. (96), (97), (98), and (99), the cost function to solve is defined as,

$$\begin{aligned}\underset{\mathbf{X}}{\operatorname{argmin}}\ c(\mathbf{X}) = \boldsymbol{\phi}_1\|\mathbf{I}_1 - \mathbf{X}\mathbf{X}^\intercal\|_F^2 + \boldsymbol{\phi}_2\|\mathbf{I}_2 - \mathbf{X}^\intercal\mathbf{X}\|_F^2 \\ +\boldsymbol{\phi}_3\|\mathbf{U}-\mathbf{R}\mathbf{X}\|_F^2 + \boldsymbol{\phi}_4\|\mathbf{V}-\mathbf{X}\mathbf{D}\|_F^2 \\ +\boldsymbol{\phi}_5\|\mathbf{B}-\mathbf{X}\mathbf{W}\|_F^2 + \boldsymbol{\phi}_6\|\mathbf{C}-\mathbf{Z}\mathbf{X}\|_F^2,\end{aligned} \tag{100}$$

where $\boldsymbol{\phi}_1, \boldsymbol{\phi}_2, \boldsymbol{\phi}_3, \boldsymbol{\phi}_4, \boldsymbol{\phi}_5$, and $\boldsymbol{\phi}_6$ are step control variables. The minimization problem is solved with a gradient descent algorithm, which iteratively minimizes (100), starting with a realization of a random CA, and with the aim to find an optimized coded aperture arrangement $\mathbf{X}^*$.

7.2.3. Cost and Fabrication Complexity Constraint The cost limitations are given by the type and number of filters used in the manufacturing, and the number of masks required for multi shot systems. The capabilities CCA depends on the number of filters developed to provide a response with the linear combination of different length waves. Thereby, a huge set of filters with different response in his band pass, provides almost any combination to discriminate an specific length wave response. The cost limitations is subject to the type (low, band, or high pass) and the number of filters used in the manufacturing process, and fluctuate growing with the number of masks required for multi shot systems. A selected reduction in the set of filters impacts the cost and fabrication complexity reduction. The spectral response of the filters in the CCA is limited to be either low or high pass filters, and the cut-off wavelengths of the filters are assumed to be selected from the subset $\lambda_0, \ldots, \lambda_{L-1}$. Thus, only $2\lambda_L$ colored filters can be selected for each coded aperture pixel. A gradient descend strategy explore as solution of (100) a non-binary solution. Thereby, a thresholding operator is applied at each iteration of the gradient descent algorithm, bounding the results to the set of filters established as solution of the CCA. Applying a gradient descend strategy to yield a non-binary solution of Eq. (100) generates the necessity of a thresholding operator at each iteration of the gradient descent algorithm. This bounds the results to the set of filters established as solution of the CCA and belonging to the set $\mathbf{\Lambda} \in \left\{\mathbf{\Lambda}^{Low} \cup \mathbf{\Lambda}^{High}\right\}$, where the set of low pass filters is $\mathbf{\Lambda}^{Low} = \left\{\lambda_0^{Low}, \ldots, \lambda_L^{Low}\right\}$, and the set of high pass filters is $\mathbf{\Lambda}^{High} = \left\{\lambda_0^{High}, \ldots, \lambda_L^{High}\right\}$.

On the other hand, the design of the CCA patterns for a multishot system is proposed such that only one moving mask is required. The strategy consists in the concatenation of vertical complementary colored coded aperture patches of size $S \times N$, defining to S as the number of pixels of the CCA that should be vertically moved between shots. This assumption impacts the final spatial dimension of the moving CCA, giving as result a pattern with $N + (S * (K - 1))$ instead $N + (N * (K - 1))$ rows of the classical multishot mask.

7.3. Simulations and Results

Using three sets of compressive measurements acquired with the model in Eq. (92), each of them with a different CCA modulation pattern, it is assessed the quality of reconstructions for the proposed pattern.

The first set is modulated by a random CCA of the *LH* filters, the second set is modulated by a genetic algorithm (GA) optimal CCA of the *LH* filters in literature [33], and the third set is modulated by the proposed moving colored CA pattern. In order to make a fair comparison, the three CCA patterns are designed to be moving patterns. For test, a data cube $\mathbf{F}$ with 256×256 pixels of spatial resolution and $L = 8$ spectral bands is used. To construct these measurements, the spectral data cube $\mathbf{F}$ was acquired with a monochromator in the spectral range between $450\,nm$ and $650\,nm$. A CCD camera AVT Marlin F0033B, with spatial resolution 656×492 pixels and a pixel pitch size of $9.9\,\mu m$ is used. The resolution of all the three CAs is 256×256 pixels, and its distribution comes from the same set of 16 filters, corresponding to the design of $L = 8$ spectral bands for low pass filters and high pass filters as well. The transmittance, is defined as the amount of light passing through the coded aperture, it depends on the number of shots acquired with the relation $T = 1/K$. The simulations were performed for $K = 2, 4$ snapshots.

The GPSR algorithm is used to get the reconstruction of the data cube [138]. Figure 32 illustrates the image in each band of the spectral data cube and Figure 33 shows four images of reference selected from the spectral bands of the original data cube to be used for these simulations in order to refer to the results. Figures 34 and 35 show the reconstruction of two and four measurement snapshots and the pixel offset value of $S = 8$, respectively. For each spectral band, the reconstruction results of the measurement obtained using random, GA optimized and designed mobile CCA are shown. It shows the improvement in spatial quality when using the designed CCA,

---

[138] M. Figueiredo, R. D. Nowak, and S. J. Wright. "Gradient Projection for Sparse Reconstruction: Application to Compressed Sensing and Other Inverse Problems". In: *Selected Topics in Signal Processing, IEEE Journal of* 1.4 (2007), pp. 586–597.

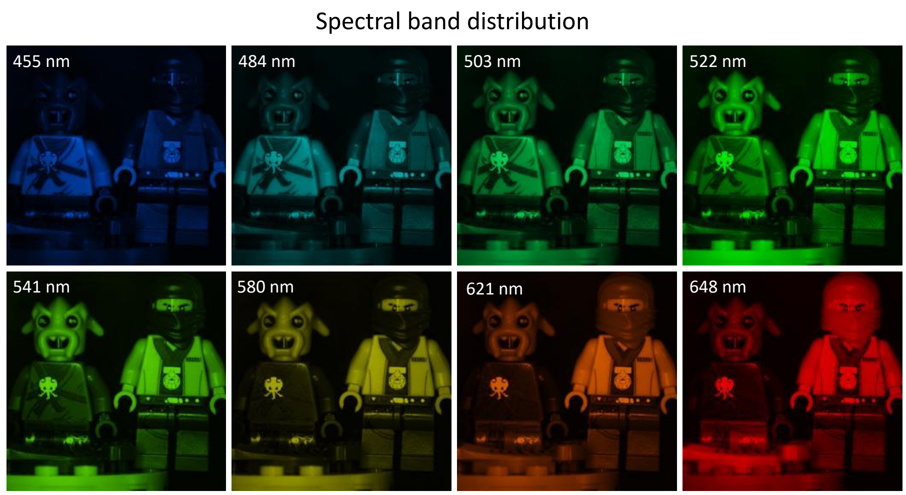

Figure 32. Spectral bands of the ground-truth data cube used in simulations.

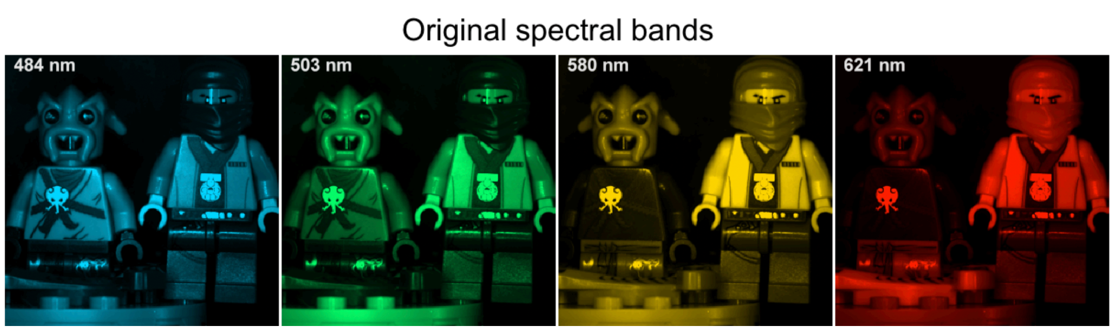

Figure 33. Four of eight spectral bands of the ground-truth data cube used in simulations.

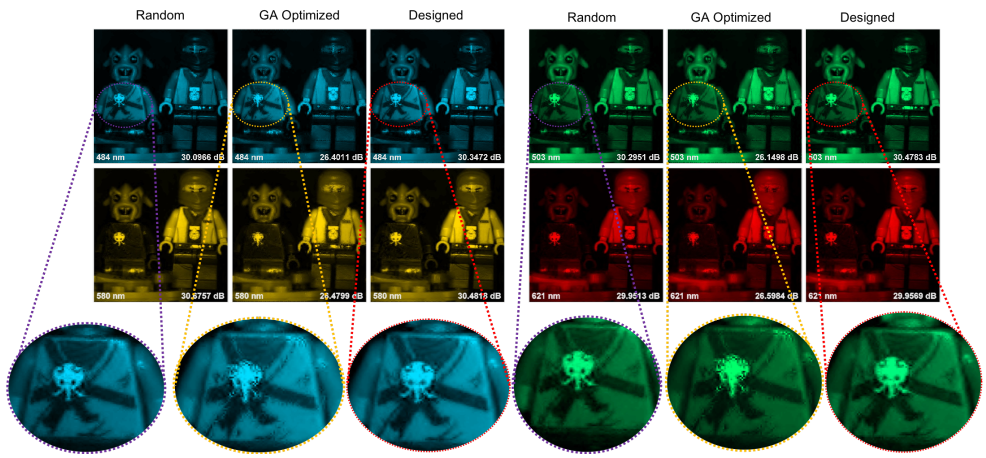

Figure 34. Four spectral bands reconstruction for the CASSI system with CCA. For each spectral band, three reconstructions from 2 measurements using the random, the genetic algorithm optimization, and the designed coded apertures are shown.

as shown in the zoomed part of Figure 2. 34, and you can also notice it by the PSNR value of 2 and 4 snapshots.

In order to analyze the influence of the shifting parameter S, a set of simulations were performed for $K = 2$ and $K = 4$ snapshots, and for the three colored CAs. The overall performance achieved by the designed colored CA is superior for 2 and 4 snapshots. Figures 36 and 37 report these results for 2 and 4 snapshots, respectively. The results correspond with results in literature [33], where random colored CAs are shown to behave closely as the optimized designs for $K = 2$. For greater number of snapshots $K = 4$, the designed colored CA from literature and the ones proposed get better reconstruction performance than random codes for all the shifting values.

7.4. Conclusions

The optimization of the moving color-coded aperture in compressed spectral imaging is proposed to establish some physical limits for the design. The optimization promotes the variability and uniformity of the pattern, as well as the consideration of hardware limitations, thereby reducing the manufacturing cost of the mask. The mobile color CA design is simulated. Compared with the randomly optimized LH-

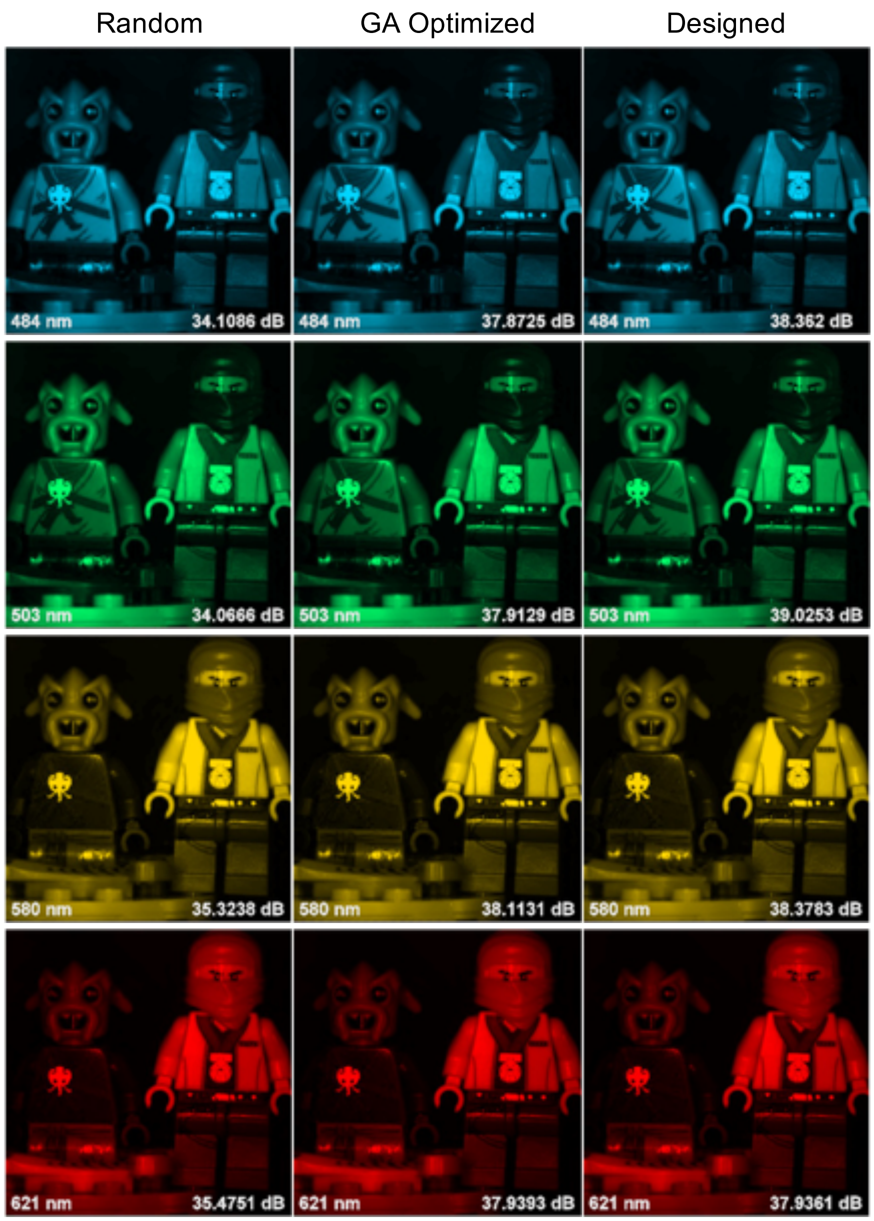

Figure 35. Reconstruction of four spectral bands using the CASSI with color coded apertures. For each spectral band, three reconstructions from 4 measurements using the random, the genetic algorithm optimization, and the designed coded apertures are displayed.

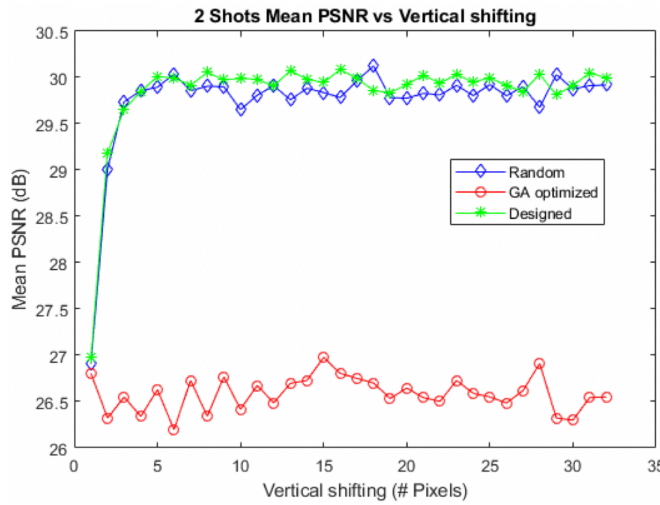

Figure 36. Mean PSNR achieved with $K = 2$ measurements snapshots for different vertical shifting value S from 1 to 32 pixels.

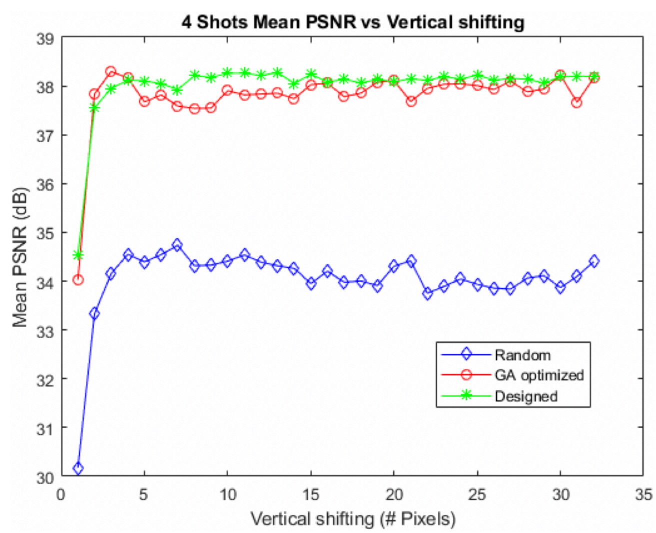

Figure 37. Mean PSNR achieved with $K = 4$ measurements snapshots for different vertical shifting value S from 1 to 32 pixels.

colored CA in the literature, the reconstructed PSNR achieves an improvement of up to 3 dB. However, this kind of design does not take into account the sensing structure of the matrix systems in CT.

Conclusions

The main contribution of this thesis embraces that any projection in an X-ray system can be as a high-resolution distribution of a decimated array of information. Thus, introducing a decimation strategy for high-resolution information, a cone beam X-ray system produces low-resolution measurements onto the detector. In this context, a high-resolution coded aperture is introduced between source and object, to disambiguate the underlying information, allowing high-resolution information from low-resolution measurements. The quality of reconstructions significantly improves by designing the coded aperture distribution while the proposed method enhances the system's condition. The proposed method reduces the Gershgorin radii of the system matrix by improving the inverse system condition describing the bounds of the eigenvalue distribution. In the big picture, the proposed distribution to design high-resolution coded apertures to be used in a compressive CBCT system with a low-resolution detector array, such that super-resolved images can be recovered without significantly changing the traditional architecture. This advance offers a bare modification with tremendous advantages. Simulation results obtained with five different test data sets consistently validate the performance of the proposed CA for different transmittance values and super-resolution factors, obtaining improvements of up to 4 dB of PSNR concerning random distributions of coded apertures in the noiseless case. On the other hand, reconstructions from projections contaminated with Poisson noise for different SNR values demonstrated the robustness of the proposed coded apertures in noisy scenarios, where the designed CA improves random patterns in up to 4 dB of PSNR. Montecarlo simulations validated these results with the GATE toolbox. Further, it was shown that the computational load of the proposed approach is up to three orders of magnitude lower than the SVD-based CA design methods.

Additionally, this work proposes for a multi-resolution iterative reconstruction scheme for a fan-beam CT image recovery. Under the premise that the image is known, a

decimation scheme is introduced. This approach exploits the neighborhood similarities, representing each uniform square zone with a single value, which reduces the number of elements to reconstruct, decreases the complexity of the inverse problem, and improves the relation measurements/variables of the sensing matrix. Simulation results concerning the proposed method show on its PSNR reconstruction by up to 16 dB and 3.5x faster than a traditional reconstruction method, even in the presence of noise. Reconstruction applications that address a reduced set of iterations to obtain a particular quality image can apply the proposed strategy to the remaining iterations, generating results to fulfill the requirements of the decimation strategy.
Finally, the optimization of the moving color-coded aperture in compressed spectral imaging is proposed to establish some physical limits for the design. The optimization promotes the variability and uniformity of the pattern, as well as the consideration of hardware limitations, thereby reducing the manufacturing cost of the mask. The mobile color CA design is simulated. Compared with the randomly optimized LH-colored CA in the literature, the reconstructed PSNR achieves an improvement of up to 3 dB. However, this kind of design does not take into account the sensing structure of the matrix systems in CT.

Bibliography

Aarle, Wim van et al. “Fast and flexible X-ray tomography using the ASTRA toolbox”. In: *Optics express* 24.22 (2016), pp. 25129–25147 (cit. on pp. 56, 86).

Abolghasemi, Vahid, Saideh Ferdowsi, and Saeid Sanei. “A gradient-based alternating minimization approach for optimization of the measurement matrix in compressive sensing”. In: *Signal Processing* 92.4 (2012), pp. 999–1009 (cit. on p. 120).

— “Fast and incoherent dictionary learning algorithms with application to fMRI”. In: *Signal, Image and Video Processing* 9.1 (2015), pp. 147–158 (cit. on pp. 31, 73, 74).

Achanta, Radhakrishna et al. “SLIC Superpixels”. In: (2010), p. 15 (cit. on p. 107).

Afonso, Manya V, José M Bioucas-Dias, and Mário AT Figueiredo. “An augmented Lagrangian approach to the constrained optimization formulation of imaging inverse problems”. In: *IEEE Transactions on Image Processing* 20.3 (2011), pp. 681–695 (cit. on pp. 72, 87).

— “Fast image recovery using variable splitting and constrained optimization”. In: *IEEE transactions on image processing* 19.9 (2010), pp. 2345–2356 (cit. on p. 68).

Aharon, M., M. Elad, and A. Bruckstein. “K-SVD: An algorithm for designing overcomplete dictionaries for sparse representation”. In: *IEEE Transactions on Signal Processing* 54.11 (2006), pp. 4311–4322. DOI: `10.1109/TSP.2006.881199` (cit. on p. 120).

Arce, Gonzalo R et al. “Compressive coded aperture spectral imaging: An introduction”. In: *IEEE Signal Processing Magazine* 31.1 (2013), pp. 105–115 (cit. on p. 26).

Arce, Gonzalo R et al. “Snapshot compressive multispectral cameras”. In: *Wiley Encyclopedia of Electrical and Electronics Engineering* (1999), pp. 1–22. DOI: https://doi.org/10.1002/047134608X.W8345 (cit. on p. 120).

Arguello, Henry and Gonzalo Arce. “Colored coded aperture design by concentration of measure in compressive spectral imaging”. In: *IEEE Transactions on Image Processing* 23.4 (2014), pp. 1896–1908 (cit. on pp. 30, 120, 128, 130).

Arguello, Henry and Gonzalo R Arce. “Rank minimization code aperture design for spectrally selective compressive imaging”. In: *IEEE transactions on image processing* 22.3 (2012), pp. 941–954 (cit. on p. 30).

Arguello, Henry, Claudia V Correa, and Gonzalo R Arce. “Fast lapped block reconstructions in compressive spectral imaging”. In: *Applied Optics* 52.10 (2013), pp. D32–D45 (cit. on p. 27).

Arguello, Henry, Hoover F Rueda, and Gonzalo R Arce. “Spatial super-resolution in code aperture spectral imaging”. In: *Compressive Sensing*. Vol. 8365. International Society for Optics and Photonics. SPIE, 2012, pp. 43 –48 (cit. on pp. 27, 31).

Baydin, Atilim Gunes et al. “Online learning rate adaptation with hypergradient descent”. In: *arXiv preprint arXiv:1703.04782* (2017) (cit. on pp. 109, 113).

Beck, Amir and Marc Teboulle. “A fast iterative shrinkage-thresholding algorithm for linear inverse problems”. In: *SIAM journal on imaging sciences* 2.1 (2009), pp. 183–202 (cit. on p. 68).

Bell, Howard E. “Gershgorin’s theorem and the zeros of polynomials”. In: *The American Mathematical Monthly* 72.3 (1965), pp. 292–295 (cit. on p. 75).

Bioucas-Dias, José M and Mário AT Figueiredo. “A new TwIST: Two-step iterative shrinkage/thresholding algorithms for image restoration”. In: *IEEE Transactions on Image processing* 16.12 (2007), pp. 2992–3004 (cit. on p. 68).

Blumensath, Thomas and Mike E Davies. “Iterative hard thresholding for compressed sensing”. In: *Applied and computational harmonic analysis* 27.3 (2009), pp. 265–274 (cit. on p. 63).

Brady, David J et al. “Coded apertures for x-ray scatter imaging”. In: *Applied optics* 52.32 (2013), pp. 7745–7754 (cit. on p. 73).

Brady, David J et al. “Compressive tomography”. In: *Advances in Optics and Photonics* 7.4 (2015), pp. 756–813 (cit. on pp. 26, 72, 73).

Buzug, Thorsten M. *Computed Tomography*. Springer-Verlag Berlin Heidelberg, 2008 (cit. on pp. 23, 25, 32, 44, 45, 51, 56, 69, 72, 106, 109).

Camarasu-Pop, Sorina et al. “Monte Carlo simulation on heterogeneous distributed systems: A computing framework with parallel merging and checkpointing strategies”. In: *Future Generation Computer Systems* 29.3 (2013), pp. 728–738 (cit. on p. 102).

Candès, Emmanuel J, Justin Romberg, and Terence Tao. “Robust uncertainty principles: Exact signal reconstruction from highly incomplete frequency information”. In: *IEEE Transactions on information theory* 52.2 (2006), pp. 489–509 (cit. on p. 62).

Candes, Emmanuel J, Justin K Romberg, and Terence Tao. “Stable signal recovery from incomplete and inaccurate measurements”. In: *Communications on Pure and Applied Mathematics: A Journal Issued by the Courant Institute of Mathematical Sciences* 59.8 (2006), pp. 1207–1223 (cit. on pp. 26, 27, 59, 67).

Candès, Emmanuel J and Michael B Wakin. “An introduction to compressive sampling”. In: *IEEE signal processing magazine* 25.2 (2008), pp. 21–30 (cit. on p. 27).

Cao, Xun et al. “Computational snapshot multispectral cameras: Toward dynamic capture of the spectral world”. In: *IEEE Signal Processing Magazine* 33.5 (2016), pp. 95–108 (cit. on p. 119).

Chambolle, Antonin. “An algorithm for total variation minimization and applications”. In: *Journal of Mathematical imaging and vision* 20.1 (2004), pp. 89–97 (cit. on pp. 65, 67).

Chambolle, Antonin and Thomas Pock. “A first-order primal-dual algorithm for convex problems with applications to imaging”. In: *Journal of mathematical imaging and vision* 40.1 (2011), pp. 120–145 (cit. on p. 67).

Chang, Chein-I. “Hyperspectral Target Detection: Hypothesis Testing, Signal-to-Noise Ratio, and Spectral Angle Theories”. In: *IEEE Transactions on Geoscience and Remote Sensing* 60 (2021), pp. 1–23 (cit. on p. 119).

Chen, Jiansheng, Zhengqin Li, and Bo Huang. “Linear spectral clustering superpixel”. In: *IEEE Transactions on image processing* 26.7 (2017), pp. 3317–3330 (cit. on p. 107).

Chen, Scott Shaobing, David L Donoho, and Michael A Saunders. “Atomic decomposition by basis pursuit”. In: *SIAM review* 43.1 (2001), pp. 129–159 (cit. on p. 71).

Chen, W., M. R. D. Rodrigues, and I. J. Wassell. “Projection Design for Statistical Compressive Sensing: A Tight Frame Based Approach”. In: *IEEE Transactions on Signal Processing* 61.8 (2013), pp. 2016–2029 (cit. on p. 121).

Chen, Yi, Nasser M Nasrabadi, and Trac D Tran. “Simultaneous joint sparsity model for target detection in hyperspectral imagery”. In: *IEEE Geoscience and Remote Sensing Letters* 8.4 (2011), pp. 676–680 (cit. on p. 29).

Choi, Kerkil and David J. Brady. “Coded aperture computed tomography”. In: *Adaptive Coded Aperture Imaging, Non-Imaging, and Unconventional Imaging Sensor Systems*. Ed. by David P. Casasent et al. Vol. 7468. International Society for Optics and Photonics. SPIE, 2009, pp. 99 –108 (cit. on p. 31).

Chun, Se Young, Yuni K Dewaraja, and Jeffrey A Fessler. “Alternating direction method of multiplier for tomography with nonlocal regularizers”. In: *IEEE transactions on medical imaging* 33.10 (2014), pp. 1960–1968 (cit. on p. 68).

Correa, Claudia V, Henry Arguello, and Gonzalo R Arce. “Spatiotemporal blue noise coded aperture design for multi-shot compressive spectral imaging”. In: *JOSA A* 33.12 (2016), pp. 2312–2322 (cit. on pp. 30, 77, 120).

Cozzini, C, S Olesinski, and G Harding. “Modeling scattering for security applications: a multiple beam x-ray diffraction imaging system”. In: *2012 IEEE Nuclear*

Science Symposium and Medical Imaging Conference Record (NSS/MIC). IEEE. 2012, pp. 74–77 (cit. on pp. 24, 69).

Cuadros, Angela, Xu Ma, and Gonzalo R Arce. "Compressive spectral x-ray tomography based on spatial and spectral coded illumination". In: *Optics express* 27.8 (2019), pp. 10745–10764 (cit. on p. 39).

Cuadros, Angela et al. "Coded aperture design for compressive X-ray tomosynthesis". In: *Computational Optical Sensing and Imaging*. Optical Society of America. 2015, CW2F–2 (cit. on pp. 30, 32, 73).

Cuadros, Angela P and Gonzalo R Arce. "Coded aperture optimization in compressive X-ray tomography: a gradient descent approach". In: *Optics Express* 25.20 (2017), pp. 23833–23849 (cit. on pp. 31, 73, 74, 77).

Cuadros, Angela P et al. "Coded aperture optimization for compressive X-ray tomosynthesis". In: *Optics express* 23.25 (2015), pp. 32788–32802 (cit. on p. 73).

Cull, Christy Fernandez et al. "Identification of fluorescent beads using a coded aperture snapshot spectral imager". In: *Applied optics* 49.10 (2010), B59–B70 (cit. on pp. 27, 31).

Davidoiu, Valentina et al. "Evaluation of noise removal algorithms for imaging and reconstruction of vascular networks using micro-CT". In: *Biomedical Physics & Engineering Express* 2.4 (2016), p. 045015 (cit. on p. 98).

De Chiffre, Leonardo et al. "Industrial applications of computed tomography". In: *CIRP annals* 63.2 (2014), pp. 655–677 (cit. on pp. 24, 69, 72).

Debatin, Maurice et al. “CT reconstruction from few-views by anisotropic total variation minimization”. In: *2012 IEEE Nuclear Science Symposium and Medical Imaging Conference Record (NSS/MIC)*. IEEE. 2012, pp. 2295–2296 (cit. on p. 66).

Delaney, John K et al. “Visible and infrared imaging spectroscopy of Picasso’s Harlequin musician: mapping and identification of artist materials in situ”. In: *Applied spectroscopy* 64.6 (2010), pp. 584–594 (cit. on p. 118).

Diwakar, Manoj and Manoj Kumar. “A review on CT image noise and its denoising”. In: *Biomedical Signal Processing and Control* 42 (2018), pp. 73–88 (cit. on p. 98).

Donoho, David L. “Compressed sensing”. In: *IEEE Transactions on information theory* 52.4 (2006), pp. 1289–1306 (cit. on pp. 26, 27, 59, 62).

Duarte-Carvajalino, Julio Martin and Guillermo Sapiro. “Learning to sense sparse signals: Simultaneous sensing matrix and sparsifying dictionary optimization”. In: *IEEE Transactions on Image Processing* 18.7 (2009), pp. 1395–1408 (cit. on pp. 73, 120).

Eckstein, Jonathan and Dimitri P Bertsekas. “On the Douglas—Rachford splitting method and the proximal point algorithm for maximal monotone operators”. In: *Mathematical Programming* 55.1 (1992), pp. 293–318 (cit. on p. 68).

Efron, Bradley et al. “Least angle regression”. In: *The Annals of statistics* 32.2 (2004), pp. 407–499 (cit. on p. 71).

Elad, Michael. “Optimized projections for compressed sensing”. In: *IEEE Transactions on Signal Processing* 55.12 (2007), pp. 5695–5702 (cit. on pp. 32, 73).

Elad, Michael. “Optimized projections for compressed sensing”. In: *IEEE Transactions on Signal Processing* 55.12 (2007), pp. 5695–5702 (cit. on p. 120).

Figueiredo, M., R. D. Nowak, and S. J. Wright. “Gradient Projection for Sparse Reconstruction: Application to Compressed Sensing and Other Inverse Problems”. In: *Selected Topics in Signal Processing, IEEE Journal of* 1.4 (2007), pp. 586–597 (cit. on p. 128).

Figueiredo, Mario AT, Jose M Bioucas-Dias, and Manya V Afonso. “Fast frame-based image deconvolution using variable splitting and constrained optimization”. In: *2009 IEEE/SP 15th Workshop on Statistical Signal Processing*. IEEE. 2009, pp. 109–112 (cit. on p. 68).

Figueiredo, Mário AT, Robert D Nowak, and Stephen J Wright. “Gradient projection for sparse reconstruction: Application to compressed sensing and other inverse problems”. In: *IEEE Journal of selected topics in signal processing* 1.4 (2007), pp. 586–597 (cit. on pp. 28, 67, 68).

Foucart, Simon and Holger Rauhut. “An invitation to compressive sensing”. In: *A mathematical introduction to compressive sensing*. Springer, 2013, pp. 1–39 (cit. on p. 27).

Galvis, Laura et al. “Optimization of a Moving Colored Coded Aperture in Compressive Spectral Imaging”. In: *ICASSP 2019-2019 IEEE International Conference on Acoustics, Speech and Signal Processing (ICASSP)*. IEEE. 2019, pp. 7685–7689 (cit. on p. 37).

— “Shifting colored coded aperture design for spectral imaging”. In: *Applied optics* 58.7 (2019), B28–B38 (cit. on pp. 37, 120).

Garcia, Hans, Claudia V Correa, and Henry Arguello. “Multi-resolution compressive spectral imaging reconstruction from single pixel measurements”. In: *IEEE Transactions on Image Processing* 27.12 (2018), pp. 6174–6184 (cit. on pp. 28, 29, 106, 109).

Gershgorin, S. “Uber die Abgrenzung der Eigenwerte einer Matrix”. In: *Izvestija Akademii Nauk SSSR, Serija Matematika* 7.6 (1931), pp. 749–754 (cit. on pp. 32, 74, 75).

Ginat, Daniel Thomas and Rajiv Gupta. “Advances in computed tomography imaging technology”. In: *Annual review of biomedical engineering* 16.1 (2014), pp. 431–453 (cit. on pp. 23, 69).

Goldfarb, Donald and Wotao Yin. “Second-order cone programming methods for total variation-based image restoration”. In: *SIAM Journal on Scientific Computing* 27.2 (2005), pp. 622–645 (cit. on p. 68).

Gonzalez, Adriana et al. “Multi-resolution compressive sensing reconstruction”. In: *arXiv preprint arXiv:1602.05941* (2016) (cit. on p. 107).

Hagen, Nathan A and Michael W Kudenov. “Review of snapshot spectral imaging technologies”. In: *Optical Engineering* 52.9 (2013), pp. 090901–090901 (cit. on p. 119).

Hamalainen, Keijo et al. “Sparse tomography”. In: *SIAM Journal on Scientific Computing* 35.3 (2013), B644–B665 (cit. on pp. 25, 26, 72).

Hsieh, Jiang. *Computed tomography: principles, design, artifacts, and recent advances*. Vol. 114. SPIE press, 2003 (cit. on p. 42).

Hsieh, Jiang et al. “Recent advances in CT image reconstruction”. In: *Current Radiology Reports* 1.1 (2013), pp. 39–51 (cit. on p. 55).

Huang, Jing et al. “Iterative image reconstruction for sparse-view CT using normal-dose image induced total variation prior”. In: *PloS one* 8.11 (2013), pp. 1–15 (cit. on p. 98).

Hudson, H Malcolm and Richard S Larkin. “Accelerated image reconstruction using ordered subsets of projection data”. In: *IEEE transactions on medical imaging* 13.4 (1994), pp. 601–609 (cit. on p. 57).

Jerez, Andrés, Miguel Márquez, and Henry Arguello. “Adaptive coded aperture design for compressive computed tomography”. In: *Journal of Computational and Applied Mathematics* 384 (2021), p. 113174 (cit. on pp. 30, 32).

Jiang, Ming and Ge Wang. “Convergence studies on iterative algorithms for image reconstruction”. In: *IEEE Transactions on Medical Imaging* 22.5 (2003), pp. 569–579 (cit. on p. 57).

Kaganovsky, Yan et al. “Compressed sampling strategies for tomography”. In: *JOSA A* 31.7 (2014), pp. 1369–1394 (cit. on pp. 25, 30, 32, 72, 73).

Kak, Avinash C, Malcolm Slaney, and Ge Wang. *Principles of computerized tomographic imaging*. 2002 (cit. on p. 50).

Lay, D.C., S.R. Lay, and J. McDonald. *Linear Algebra and Its Applications*. Always Learning. Pearson Education Limited, 2016 (cit. on pp. 75, 76).

Le, Triet, Rick Chartrand, and Thomas J Asaki. “A variational approach to reconstructing images corrupted by Poisson noise”. In: *Journal of mathematical imaging and vision* 27.3 (2007), pp. 257–263 (cit. on p. 65).

León-López, Kareth M et al. “Anomaly Detection and Classification in Multispectral Time Series Based on Hidden Markov Models”. In: *IEEE Transactions on Geoscience and Remote Sensing* 60 (2022), pp. 1–11 (cit. on p. 118).

Li, Bo et al. “Projection matrix design using prior information in compressive sensing”. In: *Signal Processing* 135 (2017), pp. 36–47 (cit. on pp. 31, 74).

Li, Qingli et al. “Review of spectral imaging technology in biomedical engineering: achievements and challenges”. In: *Journal of biomedical optics* 18.10 (2013), pp. 100901–100901 (cit. on p. 118).

Liang, Haida. “Advances in multispectral and hyperspectral imaging for archaeology and art conservation”. In: *Applied Physics A* 106.2 (2012), pp. 309–323 (cit. on p. 118).

Liu, Ming-Yu et al. “Entropy rate superpixel segmentation”. In: *CVPR 2011*. IEEE. 2011, pp. 2097–2104 (cit. on p. 29).

Lu, Guolan et al. “Spectral-spatial classification for noninvasive cancer detection using hyperspectral imaging”. In: *Journal of biomedical optics* 19.10 (2014), pp. 106004–106004 (cit. on p. 118).

Lustig, Michael, David Donoho, and John M Pauly. “Sparse MRI: The application of compressed sensing for rapid MR imaging”. In: *Magnetic Resonance in Medicine: An Official Journal of the International Society for Magnetic Resonance in Medicine* 58.6 (2007), pp. 1182–1195 (cit. on p. 121).

MacCabe, Kenneth et al. “Pencil beam coded aperture x-ray scatter imaging”. In: *Optics Express* 20.15 (2012), pp. 16310–16320 (cit. on p. 31).

Manolakis, Dimitris, David Marden, Gary A Shaw, et al. “Hyperspectral image processing for automatic target detection applications”. In: *Lincoln laboratory journal* 14.1 (2003), pp. 79–116 (cit. on pp. 118, 119).

Manolakis, Dimitris and Gary Shaw. “Detection algorithms for hyperspectral imaging applications”. In: *IEEE signal processing magazine* 19.1 (2002), pp. 29–43 (cit. on pp. 118, 119).

Mao, Tianyi et al. “Coded Aperture Optimization in X-Ray Tomography via Sparse Principal Component Analysis”. In: *IEEE Transactions on Computational Imaging* 6 (2020), pp. 73–86. DOI: 10.1109/TCI.2019.2919228 (cit. on p. 73).

Marquez, Miguel and Henry Arguello. “Coded aperture optimization for single pixel compressive computed tomography”. In: *Journal of Computational and Applied Mathematics* 348 (2019), pp. 58–69 (cit. on pp. 30, 74, 89).

Martin, Matthew E et al. “Development of an advanced hyperspectral imaging (HSI) system with applications for cancer detection”. In: *Annals of biomedical engineering* 34.6 (2006), pp. 1061–1068 (cit. on p. 118).

Martinez, Kirk et al. “Ten years of art imaging research”. In: *Proceedings of the IEEE* 90.1 (2002), pp. 28–41 (cit. on p. 118).

Massoudifar, Pegah, Anand Rangarajan, and Paul Gader. “Superpixel estimation for hyperspectral imagery”. In: *Proceedings of the IEEE Conference on Computer Vision and Pattern Recognition Workshops*. 2014, pp. 287–292 (cit. on p. 29).

Mejia, Yuri and Henry Arguello. “Binary codification design for compressive imaging by uniform sensing”. In: *IEEE Transactions on Image Processing* 27.12 (2018), pp. 5775–5786 (cit. on pp. 30, 32, 74).

Mejia, Yuri and Henry Arguello Sr. “Filtered gradient reconstruction algorithm for compressive spectral imaging”. In: *Optical Engineering* 56.4 (2016), pp. 1 –11 (cit. on p. 62).

Mojica, Edson, Claudia V Correa, and Henry Arguello. “High-resolution coded aperture optimization for super-resolved compressive x-ray cone-beam computed tomography”. In: *Applied Optics* 60.4 (2021), pp. 959–970 (cit. on p. 36).

Mojica, Edson, Hans Garcia, and Henry Arguello. “Impact of Multi-resolution reconstruction on Computed Tomography”. In: *2019 XXII Symposium on Image, Signal Processing and Artificial Vision (STSIVA)*. IEEE. 2019, pp. 1–5 (cit. on p. 36).

Mojica, Edson, Said Pertuz, and Henry Arguello. “High-resolution coded-aperture design for compressive X-ray tomography using low resolution detectors”. In: *Optics Communications* 404 (2017). Super-resolution Techniques, pp. 103 –109. DOI: https://doi.org/10.1016/j.optcom.2017.06.053 (cit. on pp. 27, 30, 32, 74, 121).

Muthukrishnan, Shanmugavelayutham. *Data streams: Algorithms and applications*. Now Publishers Inc, 2005 (cit. on p. 63).

Pan, Xiaochuan, Emil Y Sidky, and Michael Vannier. “Why do commercial CT scanners still employ traditional, filtered back-projection for image reconstruction?” In: *Inverse problems* 25.12 (2009), p. 123009 (cit. on p. 62).

Pani, Silvia et al. “Modelling an energy-dispersive x-ray diffraction system for drug detection”. In: *IEEE Transactions on Nuclear Science* 56.3 (2009), pp. 1238–1241 (cit. on pp. 24, 69).

Parada-Mayorga, A, A Cuadros, and GR Arce. “Coded aperture design for compressive X-ray tomosynthesis via coherence analysis”. In: *Biomedical Imaging (ISBI 2017), 2017 IEEE 14th International Symposium on*. IEEE. 2017, pp. 44–47 (cit. on p. 73).

Parada-Mayorga, Alejandro and Gonzalo R. Arce. “Colored Coded Aperture Design in Compressive Spectral Imaging via Minimum Coherence”. In: *IEEE Transactions on Computational Imaging* 3.2 (2017), pp. 202–216. DOI: `10.1109/TCI.2017.2692649` (cit. on p. 120).

Perelli, Alessandro et al. “Compressive Computed Tomography Reconstruction through Denoising Approximate Message Passing”. In: *SIAM Journal on Imaging Sciences* 13.4 (2020), pp. 1860–1897 (cit. on p. 98).

Qu, Zhaonan, Yinyu Ye, and Zhengyuan Zhou. *Diagonal Preconditioning: Theory and Algorithms*. 2020. arXiv: `2003.07545 [cs.LG]` (cit. on p. 83).

Ramani, Sathish and Jeffrey A Fessler. “A splitting-based iterative algorithm for accelerated statistical X-ray CT reconstruction”. In: *IEEE transactions on medical imaging* 31.3 (2011), pp. 677–688 (cit. on pp. 28, 68).

Ramirez, Ana et al. “Spectral image classification from optimal coded-aperture compressive measurements”. In: *IEEE Transactions on Geoscience and Remote Sensing* 52.6 (2013), pp. 3299–3309 (cit. on p. 31).

Redko, Ievgen and Younès Bennani. “Non-negative Matrix Factorization with Schatten p-norms Reguralization”. In: *International Conference on Neural Information Processing*. Springer. 2014, pp. 52–59 (cit. on p. 91).

Reiser, Ingrid and Stephen Glick. *Tomosynthesis imaging*. Taylor & Francis, 2014 (cit. on pp. 26, 72, 73).

Rish, Irina and Genady Grabarnik. “Sparse signal recovery with exponential-family noise”. In: *Compressed Sensing & Sparse Filtering*. Springer, 2014, pp. 77–93 (cit. on p. 63).

Rudin, Leonid I, Stanley Osher, and Emad Fatemi. “Nonlinear total variation based noise removal algorithms”. In: *Physica D: nonlinear phenomena* 60.1-4 (1992), pp. 259–268 (cit. on p. 65).

Rueda, Hoover, Henry Arguello, and Gonzalo R Arce. “DMD-based implementation of patterned optical filter arrays for compressive spectral imaging”. In: *JOSA A* 32.1 (2015), pp. 80–89 (cit. on p. 30).

Rueda, Hoover F, Henry Arguello, and Gonzalo R Arce. “On super-resolved coded aperture spectral imaging”. In: *Algorithms and Technologies for Multispectral, Hyperspectral, and Ultraspectral Imagery XIX*. Vol. 8743. International Society for Optics and Photonics. SPIE, 2013, pp. 421 –426 (cit. on p. 31).

Said, Amir and William A Pearlman. “An image multiresolution representation for lossless and lossy compression”. In: *IEEE Transactions on image processing* 5.9 (1996), pp. 1303–1310 (cit. on p. 107).

Sánchez, Karen et al. “Classification of Cocoa Beans Based on their Level of Fermentation using Spectral Information”. In: *TecnoLógicas* 24.50 (2021), pp. 172–188 (cit. on p. 118).

Sarrut, David et al. “A review of the use and potential of the GATE Monte Carlo simulation code for radiation therapy and dosimetry applications”. In: *Medical physics* 41.6Part1 (2014), p. 064301 (cit. on pp. 86, 100).

Sefi, O et al. “X-ray imaging of fast dynamics with single-pixel detector”. In: *Optics Express* 28.17 (2020), pp. 24568–24576 (cit. on p. 74).

Stern, Adrian. *Optical compressive imaging*. CRC Press, 2016 (cit. on p. 119).

Strecker, H. “Automatic detection of explosives in airline baggage using elastic X-ray scatter”. In: *Medicamundi* 42 (1998), pp. 30–33 (cit. on pp. 24, 69).

Sutskever, Ilya et al. “On the importance of initialization and momentum in deep learning”. In: *International conference on machine learning*. PMLR. 2013, pp. 1139–1147 (cit. on p. 67).

Tarazaga, Pablo and Diego Cuellar. “Preconditioners generated by minimizing norms”. In: *Computers & Mathematics with Applications* 57.8 (2009), pp. 1305–1312 (cit. on p. 84).

Thenkabail, P.S. and J.G. Lyon. *Hyperspectral Remote Sensing of Vegetation*. CRC Press, 2016 (cit. on p. 118).

Thompson, David R et al. “Superpixel endmember detection”. In: *IEEE Transactions on Geoscience and Remote Sensing* 48.11 (2010), pp. 4023–4033 (cit. on p. 29).

Tibshirani, Robert. “Regression shrinkage and selection via the lasso”. In: *Journal of the Royal Statistical Society: Series B (Methodological)* 58.1 (1996), pp. 267–288 (cit. on p. 71).

Tillack, G-R, Christina Nockemann, and Carsten Bellon. “X-ray modeling for industrial applications”. In: *NDT & E International* 33.7 (2000), pp. 481–488 (cit. on pp. 24, 69).

Tropp, Joel A and Anna C Gilbert. “Signal recovery from random measurements via orthogonal matching pursuit”. In: *IEEE Transactions on information theory* 53.12 (2007), pp. 4655–4666 (cit. on pp. 28, 63).

Wang, Xing and Jie Liang. “Multi-resolution compressed sensing reconstruction via approximate message passing”. In: *IEEE Transactions on Computational Imaging* 2.3 (2016), pp. 218–234 (cit. on p. 28).

— “Multi-resolution compressed sensing reconstruction via approximate message passing”. In: *IEEE Transactions on Computational Imaging* 2.3 (2016), pp. 218–234 (cit. on p. 107).

Wang, Zhongmin and Gonzalo R Arce. “Variable density compressed image sampling”. In: *IEEE Transactions on image processing* 19.1 (2009), pp. 264–270 (cit. on p. 121).

Wang, Zhongmin, Gonzalo R Arce, and Jose L Paredes. “Colored random projections for compressed sensing”. In: *2007 IEEE International Conference on Acoustics, Speech and Signal Processing-ICASSP’07*. Vol. 3. IEEE. 2007, pp. III–873–III–876 (cit. on p. 120).

Wright, Stephen J, Robert D Nowak, and Mário AT Figueiredo. “Sparse reconstruction by separable approximation”. In: *IEEE Transactions on signal processing* 57.7 (2009), pp. 2479–2493 (cit. on pp. 28, 68).

Wu, Di and Da-Wen Sun. “Advanced applications of hyperspectral imaging technology for food quality and safety analysis and assessment: A review—Part I: Fundamentals”. In: *Innovative Food Science & Emerging Technologies* 19.6 (2013), pp. 1–14 (cit. on p. 118).

Wu, Yuehao et al. “Development of a digital-micromirror-device-based multishot snapshot spectral imaging system”. In: *Optics letters* 36.14 (2011), pp. 2692–2694 (cit. on p. 120).

Yang, Xiaoquan et al. “Abnormal pixel detection using sum-of-projections symmetry in cone beam computed tomography”. In: *Optics express* 20.10 (2012), pp. 11014–11030 (cit. on p. 72).

Yuan, Xin, David J Brady, and Aggelos K Katsaggelos. “Snapshot compressive imaging: Theory, algorithms, and applications”. In: *IEEE Signal Processing Magazine* 38.2 (2021), pp. 65–88 (cit. on p. 120).

Zhang, Qiang et al. “Joint segmentation and reconstruction of hyperspectral data with compressed measurements”. In: *Applied optics* 50.22 (2011), pp. 4417–4435 (cit. on p. 31).

Zhang, Shuzhen and Shutao Li. “Spectral-spatial classification of hyperspectral images via multiscale superpixels based sparse representation”. In: *2016 IEEE International Geoscience and Remote Sensing Symposium (IGARSS)*. IEEE. 2016, pp. 2423–2426 (cit. on p. 29).

Zhang, Xuewen et al. “SLIC superpixels for efficient graph-based dimensionality reduction of hyperspectral imagery”. In: *Algorithms and Technologies for Multispectral, Hyperspectral, and Ultraspectral Imagery XXI*. Vol. 9472. International Society for Optics and Photonics. 2015, pp. 92 –105 (cit. on p. 29).